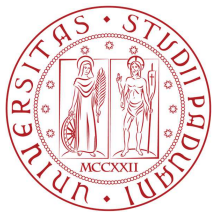

UNIVERSITÀ DEGLI STUDI DI PADOVA

Dipartimento di Fisica e Astronomia "Galileo Galilei"

Corso di Laurea Magistrale in Astronomia

Tesi di Laurea

Study of the superficial variegation and surface evolution of comet 67P/C-G as seen by Rosetta/OSIRIS

Relatore

Prof.ssa Monica Lazzarin

Correlatore

Dott.ssa Fiorangela La Forgia

Laureanda

Martina Raniolo

Anno Accademico 2020/2021

Abstract

The aim of this work is to provide a surface analysis of comet 67P/C-G. A spectrophotometric study has been performed on multiband OSIRIS images acquired by the Rosetta mission, after applying a topographic and photometric correction. The spectral analysis is limited to regions not yet spectrophotometrically investigated. Spectra show changes in the surface as the comet approaches perihelion.

Contents

Chapter 1

The Rosetta space mission

The Rosetta mission was approved in November 1993 by ESA's Science Programme Committee, as the Planetary Cornerstone Mission in ESA's long-term space science programme.
Rosetta was launched on March 2004 and its main objective was to rendezvous with comet 67P/Churyumov-Gerasimenko, enter its orbit and perform observations of the comet's nucleus and coma.
During its ten years journey towards the comet, the spacecraft passed by two asteroids: 2867 Steins - in 2008 and 21 Lutetia - in 2010. The relevance of studying comets and asteroids is that they allow us to investigate the primordial phases of the Solar System formation and its evolution. Indeed, it seems that comets have preserved their pristine composition, including volatiles, because of the high distance from the Sun and their small sizes. Thus by studying their morphology, dynamics and chemical composition it is possible to understand the physical and chemical conditions that were present at the origin of the Solar System.
The Rosetta mission takes its name from the Rosetta Stone, a stela of black basalt incised with a Ptolemaic decree, in three scripts (Egyptian Hieroglyphs, Egyptian Demotic and Greek). The great significance of the Stone is that it provided the key to deciphering Egyptian hieroglyphs, as well as scientists hope that the Rosetta mission provides solutions to some of the open questions concerning the Solar System origin and evolution.
The mission included a lander, named Philae after an island in the Nile river, where archaeologists found an inscription on an obelisk that confirmed their interpretation of the Rosetta Stone texts.
The aim of the lander Philae was to do experiments on the comet's surface to analyse its composition, retrieve samples and send data to Earth by means of the orbiter antenna. Philae was developed by the European Space Agency.
The Rosetta mission counts some records between cometary missions, indeed it was the first mission to to successfully land onto a comet's nucleus and to follow a comet during its journey towards perihelion, capturing images of its evolution due to the perihelion passage. It has almost reached Jupiter's orbit counting on the power produced by the solar panels alone.

Contribution to the mission came from ESA Member States, some of the national space agency such as ASI and from NASA.

Figure 1.1: Composite image of Rosetta and Philae at the comet 67P/Churyumov-Gerasimenko.

1.1 The Rosetta journey

The Rosetta journey to reach the target, comet 67P/Churyumov-Gerasimenko, lasted ten years. Rosetta performed a series of looping orbits that brought it back for three Earth fly-by and one Mars fly-by, passing trough the Main Belt Asteroids twice. Thanks to each gravitational assist, the spacecraft changed its velocity and trajectory as it extracted energy from the gravitational field of Earth or Mars. In this way it was possible for the spacecraft, which was powered by solar panels, to reach the comet at a relative velocity of nearly 1 m/s. The European Space Operations Centre, ESOC, was the responsible for the control and determination of the spacecraft orbit.
Rosetta was launched by an Ariane 5G+ from Kourou, French Guaiana, on March the 2nd 2004. The first Earth fly-by took place the following year, during which instruments on board the spacecraft were controlled and calibrated. The Mars fly-by, in February 2007, required Rosetta to fly past Mars at just 250 km from the surface, and spend 24 minutes in its shadow. The second Earth gravity assist was on 13 November 2007 and the last, on 13 November 2009, provided Rosetta the push required to reach comet 67P.

1.1.1 Fly-by to asteroid 2867 Steins

En-route to the comet, Rosetta encountered asteroid 2867 Steins on 5 September 2008. A primitive asteroid of nearly 5 km, which looked attractive for its peculiar spectral classification, an E-type asteroid. Scientists believe that Steins was part of a

larger differentiated object that had broken up and it was later struck by other objects, creating impact craters. The asteroid interior is thought to be a rubble pile. Steins showed a diamond shape that probably gained from the YORP effect, in which photons from the Sun are re-radiated as infrared emission taking momentum from the body and altering the rotation rate. The attribution of surface reshaping to the YORP effect, accounts for the lack of smaller craters on Steins. Indeed the effect would have caused landslides to fill in the smaller craters. This is the first time that the YORP effect has been seen in a main-belt asteroid (Keller et al. 2010).

1.1.2 Fly-by to asteroid 21 Lutetia

Rosetta reached 21 Lutetia, an asteroid with a diameter of 130 kilometres, on 10 July 2010. It was the largest asteroid ever seen in close-up at the time. Images from Rosetta revealed an irregular shape, complex surface geology and the presence of giant craters.
By counting the craters, it was determined that the surface of Lutetia is about 3.6 billion years old and probably had an almost spherical shape before large amounts of material were removed by impacts (Sierks et al. 2011). OSIRIS revealed a vast network of grooves, fractures and grabens, similar in appearance to those on the Martian moon Phobos, while analysis of the VIRTIS data showed a remarkable uniformity in the surface spectral properties. This implied that the variations in albedo observed by OSIRIS must be related to transport and/or sorting of fragmented surface material, rather than variations in composition. VIRTIS also determined that the asteroid's surface temperature varied between 170 K and 245 K (-103 °C to -28 °C), with the highest temperatures in regions where the Sun was high above the local horizon and on Sun-facing slopes. The data suggest that the surface is covered by a layer of dust particles in the 50 to 100 micron size range (Coradini et al. 2011).

1.1.3 Hibernation

Because of the long journey, Rosetta hibernated from May 2011 to January 2014. In this way it was possible to reduce the energy and fuel consumption, indeed Rosetta was powered by solar panels only, but so far from the Sun there would not be enough power to keep all the spacecraft's systems operating. So everything was shut down, except for the on board computer, radio receivers and some internal heaters. During its sleeping time Rosetta turned its orientation once a minute towards the Sun, so that solar panels could receive as much radiation as possible. It was during hibernation that Rosetta reached the highest distance from the Sun, nearly 800 millions km.

1.1.4 Approach and Stay at Comet 67P

On 20 January 2014 Rosetta was awaken and all twenty-one instruments were brought online and checked out. Between May and August the spacecraft performed a series of manoeuvres, known as pyramid trajectories, to reduce Rosetta velocity at almost 25 m/s, the velocity required to approach the comet without the risk of being

pitched away. The final arrival manoeuvre, to put Rosetta into the comet's orbit, took place on 6 August 2014 when the comet was 3.6 AU from the Sun.
The rendezvous with the comet occurred with Rosetta at a distance of about 100 kilometres from the comet. This was too far away for the comet to hold the spacecraft with its weak gravitational field. During this time, it was studied how Rosetta responded to the weak but complex gravitational field generated by the comet's bilobate shape and scientists gathered data to characterise the comet rotational speed, shape and dimensions.
Gradually Rosetta got closer to the comet until the spacecraft was captured by the comet's gravitational field on 10 September 2014. On November 2014, Rosetta deployed the Philae lander to the surface of comet 67P, when the spacecraft was at a distance of 22 km from the comet. Philae performed its first touch down within the selected area for its landing. Rosetta followed comet 67P along its orbit through its closest approach to the Sun, which occurred on 13 August 2015. During this phase the spacecraft was moved to about 100 km from the comet to prevent dust and gas tales damages due to the increasing cometary activity at perihelion.
Rosetta followed comet 67P for almost two years during its journey towards the perihelion, looking at its changes. The mission ended on 30 September 2016 with a controlled impact on the comet's surface. During this descent to the comet, high resolution images and sensitive measurements of gas and dust were collected till a distance of few meters from the ground.
The decision to end the mission was the result of the spacecraft's ever increasing distance from the Sun, which means significantly reduced solar power with which the spacecraft and its instruments have to operate. Furthermore Rosetta was an ageing spacecraft which have endured the harsh environment of space for over 12 years.

1.2 Landing on a comet

The presence of the Philae lander on board Rosetta and the experiments it carried out were certainly among the peculiarities of the mission.
While the spacecraft approached the comet,the OSIRIS team was mapping the comet's surface in order to find a suitable site for Philae to land. Five candidate regions had been identified, all were more difficult terrains than hoped because of the presence of cliffs, craters and boulders on the surface. Thus, after a detailed analysis of the Philae's capabilities and of the features of the site, the choice fell on a location named Agilkia, situated on the head lobe.
On 12 November 2014, Philae was deployed on the surface of comet 67P, touching down about seven hours later, but instead of anchoring itself to the comet it bounced twice. Indeed, Philae experienced the comet's very low-gravity (10^{-3} m/s^2) (Sierks et al. 2015) and problems in the anchoring system which was not able to free the harpoons. Philae rebounded from its initial touchdown site at Agilkia and subsequently performed an almost two-hour flight during which it collided with a cliff edge, then tumbled towards a second touchdown location. Despite that, the lander completed many experiments,

returning unique data before entering into hibernation.
After years of work, the second touchdown site of the lander has been located in a spot that resembles the shape of a skull. It was important to find the touchdown site because sensors on Philae indicated that it had dug into the surface, most likely exposing the primitive comet's icy interior and an unexpected roundness. It is apparent that Philae struck the surface multiple times during the second touchdown event, and spent around two minutes there (O'Rourke et al. 2020).
The Philae magnetometer ROMAP looked at changes recorded in the data that arose when its boom, which sticks out 48 cm from the lander, moved as it struck a surface. This created a characteristic set of spikes in the magnetic data as the boom moved relative to the lander body, which provided an estimate of the duration of Philae stamping into the ice. A notable imprint revealed in the images was created as Philae's top surface sank 25 cm into the ice on the side of a crevice, leaving identifiable marks of its drill tower and sides. The spikes in the magnetic field data arising from the boom movement showed that it took Philae three seconds to make this particular depression. Analysis of images and data from OSIRIS and VIRTIS confirmed that the bright exposure seen in the images was water-ice covering an area of about $3.5m^2$, located just 30 m away from where Philae was finally imaged. The ice revealed was brighter than the surrounds because it had not been previously exposed to the space environment and undergone space weathering.
The study of the second touchdown site also provided the first in situ measurement of the boulder's porosity, about 75%, and showed that the comet is homogeneous anywhere in its interior, on all size scales down to about one metre. This implies that the boulders represent the overall state of the comet's interior when it formed almost 4.5 billion years ago (O'Rourke et al. 2020).
The analysis of the Philae touchdowns helped to understand that the strength of a comet is a critical and important point for future lander missions. Indeed, the comet's fluffy interior is a really valuable information in terms of how to design the landing mechanisms, as well as for the mechanical processes that might be needed to retrieve samples.
Less than a month before the end of the mission, an image taken with Rosetta's high-resolution camera showed that Philae rested against a cliff, in a sheltered site, in the comet's Abydos region (fig.1.2).
The images were taken by the OSIRIS narrow angle camera, on 2 September, as the orbiter came within 2.7 km of the surface and clearly showed the main body of the lander and two of its three legs. They also provided proof of Philae's orientation, making it clear why establishing communications was so difficult following its landing on 12 November 2014.
After being in operation for three days, Philae's primary battery was exhausted and the lander went into hibernation, only to wake up again and communicate with Rosetta in June and July 2015, as the comet came closer to the Sun and more power was available to send data.

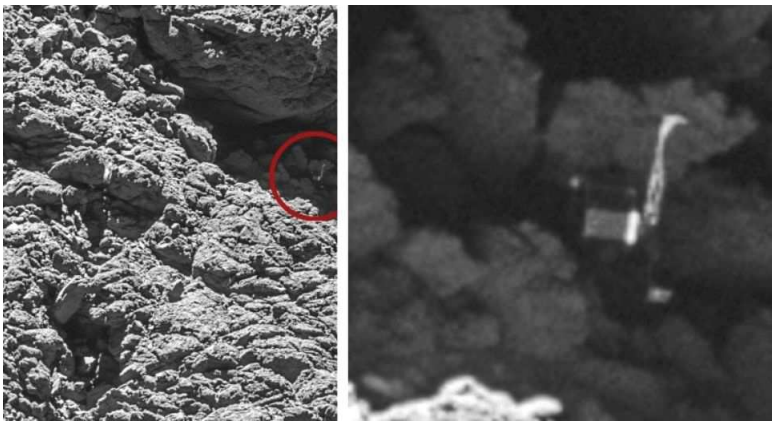

Figure 1.2: The Abydos site where Philae rested after two touchdowns.

1.3 Spacecraft technical details

The Rosetta spacecraft was composed of two main elements: the Rosetta orbiter, which carried 11 science instruments and the Philae lander, which carried 10 science instruments. The Rosetta design was based on a box-type central structure, 2.8m×2.1m×2.0m, on which all subsystems and payload equipment were mounted.
The central box, made of aluminium, weighed nearly 3000 kg and more than half of the weight was the fuel necessary for the launch. At the center of the orbiter, around a vertical tube, there was the propulsion system with two tanks, one for the fuel and the other for the oxidant. The spacecraft orbit was maintained by means of 24 engines which provided the required push of 10 Newton.
Solar panels were the only source of energy of the spacecraft, with a combined area of 64 m^2 and a length of 14 m, while the total span from tip to tip was 32 m. Panels were able to perform a 180° rotation to catch the solar radiation. They were made of hundreds of non-reflective silicon cells which produced a power of 8700 Watt near the Sun and almost 400 Watt at the highest distance reached during the mission. Rosetta was the first space mission to access the Main Belt Asteroids by only use of solar panels as energy source.
An antenna for communications with Earth was installed on one side of the orbiter. It was an high gain radio antenna, with a 2.2 m diameter, biaxial shape and able to change direction in order to constantly point towards Earth. It sent highly packed data with a maximum velocity of 22000 bit per second. On Earth, communications worked by means of a parabolic antenna, with a 35 m diameter, developed by ESA and located in Australia, New Norcia. Radio signal needed almost 50 minutes to reach the spacecraft, moreover the signal was interrupted when the spacecraft passed behind the Sun, thus to have a better signal coverage the team decided to use another 35 m antenna located in Spain, Cerebros. Hence, to take into account also the rotation of the Earth Rosetta had an internal memory to save the data that couldn't be sent immediately to Earth.
The Philae lander, about 1m×1m×1m, was attached to the spacecraft opposite side respect to the antenna. It was made of carbon and weighed 100 kg. It was composed

of a platform for the technical instruments, some of which were covered by solar cells. It was designed to self-eject from the vehicle and to land on the comet's surface by using of three 'legs' and an harpoon to be anchored on the surface. The harpoon was necessary to face the low gravitational attraction of the comet.
Finally, the spacecraft carried black panels to maintain the instruments at a warm temperature when Rosetta was at a high distance from the Sun, while to cool down the instruments near perihelion it was equipped with some radiators.

1.4 Rosetta instruments and their main results

The Rosetta orbiter carried eleven scientific instruments on the top panel, whose goals were to analyse the comet's nucleus and the gas and dust jets due to comet's activity near the Sun. The instruments were:
ALICE, an Ultraviolet Imaging Spectrometer thought to analyze the gas from the coma and the tail in the far ultraviolet, between 70 nm and 250 nm. It was also used to study the surface's composition and the production rate of water, monoxide and bi-oxide of carbon. Results from ALICE showed that the comet is unusually dark in the UV range and revealed the presence of hydrogen and oxygen in the coma (Feldman et al. 2011).
CONSERT, Comet Nucleus Sounding Experiment by Radio wave Transmission, was an instrument to study the internal structure of the comet by use of the delay in the propagation and re-emission of the signal. It passed radio waves through the nucleus between the lander and the orbiter, indeed there is a CONSERT instrument on the lander too (fig.1.3). It showed that the porosity of the 'head' lobe of the comet is very high, about 75-85 %. This is consistent with a very loosely compacted mixture of dust and ice, termed a 'rubble pile'. This observation is also supported by the Radio Science Investigation team analysis of the way in which the Rosetta orbiter is pulled by the gravity of the comet. Indeed, the latter allowed them to infer the comet's porosity. According to the investigation team, the high porosity suggests that the formation of the comet was a relatively gentle collision with many small 'cometesimals' falling together at speeds of less than 1 m/s. This would mean that cometesimals rested against each other rather than melting into a single slab (Kofman et al. 2015).
COSIMA, Cometary Secondary Ion Mass Analyzer, was an instrument to collect dust grains emitted by the comet. It had a microscope and a cannon with ions to bomb dust grains, then it analyzes the secondary ions produced to understand if they are organic or not. Thanks to COSIMA almost 6053 particles have been identified.
GIADA, Grain Impact Analyzer and Dust Accumulator, measured the mass and the velocity distribution of the coma dust grains. GIADA revealed two main types of dust grain: compact particles, with dimensions between 0.03 and 1 mm and 'soft compounds', with bigger dimensions between 0.2 and 2.5 mm. It also tracked the movement of dust grains around the comet, so two distinct populations of dust grains have been identified. One set flowing from the comet was detected close to the spacecraft, while the other orbited the comet no closer than 130 km from the spacecraft (Rotundi et al. 2015).

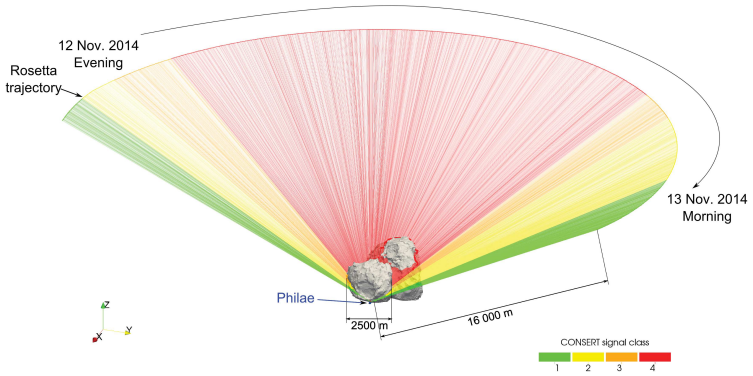

Figure 1.3: Diagram showing the propagation of signals between Rosetta and Philae through the nucleus of comet 67P, between 12 and 13 November 2014. Green represents the best signal quality, decreasing in quality to red for no signal.

MIDAS, Micro-Imaging Dust Analysis System, used an atomic force microscope to make a statistical analysis of dust grains. It showed that dust grains are made of other little grains, which seems to be stretched along one direction.

Figure 1.4: Representation of scientific instruments on board the Rosetta orbiter.

MIRO, Microwave Instrument for the Rosetta Orbiter, made measures of the

superficial temperature of the comet and determined the abundance of gasses. The MIRO team produced a map of the coma water vapor and during Rosetta's approach to the comet, in 2014, it registered that the amount of water vapour being released by the comet increased by a factor of ten between June and August 2015. MIRO also found that a substantial portion of the water seen during the activity phase originated from the comet's neck (Gulkis et al. 2015).

OSIRIS, Optical Spectroscopic and InfraRed Remote Imaging System, was a double camera imaging system which worked in the visible, near infrared and near ultraviolet. The two cameras, Narrow Angle Camera and Wide Angle Camera, had the same electronics and were thermally isolated.

The NAC camera was used for high resolution images of the cometary surface and it was composed of eleven filers with wavelength between 250 and 1000 nm. It had a $2.2° \times 2.2°$ field of view and a mirror system with a foci length of 72 cm.

The WAC camera had a very wide field of view, $11.6° \times 12.2°$, and it was composed of fourteen filters in the wavelength range between 240 and 720 nm. It had a mirror system with a foci length of 13 cm and it was able to remove diffused light, so it was good to capture images of dust and gas from the comet's surface. The WAC camera was built in Padova by a team of researchers from the Astronomy and Engineering Departments (DEI and CISAS).

OSIRIS provided the images that were used to construct the three-dimensional shape model of the comet (Preusker et al. 2017) and the images to make high resolution spectrophotometry (Fornasier at al. 2016, Deshapriya et al. 2016, La Forgia et al. 2015, Oklay et al. 2016). It gave the opportunity to study the topographical features, the geomorphological superficial variegation, the mineralogical properties and the changes in the surface due to the comet's activity and jets. For example images from OSIRIS displayed pits 100 metres wide and deep, 'goose bumps' of about three meters in diameter in the walls, and the largest chunks seen by OSIRIS were greater than 1 metre in size near perihelion, while before then they were only around 1 centimetre (N. Thomas, H. Sierks, et al. 2015).

ROSINA, Rosetta Orbiter Spectrometer for Ion and Neutral Analysis, by use of two sensors analyzed the atmospheric and ionospheric composition. It was also designed to reveal the gas velocity and reactions.

The ROSINA instrument proved that the gas pressure increases near the cometary nucleus and showed that the water on the comet was substantially different from the water on Earth. The difference with Earth's water is apparent in the ratio of deuterium to hydrogen atoms in the water. When deuterium combines with an oxygen molecule it is known as heavy water. On Earth there are roughly 160 molecules of heavy water for every million molecules of the normal stuff, while ROSINA found that the amount of deuterium on comet 67P was greater by a factor of three(Altwegg et al. 2014). These results led to further doubts on the possibility that comets are the source of water on Earth, which remains an open question.

RCP, Rosetta Consortium Plasma, was a five instrument set. Its function was to measure the physical properties of the nucleus and to analyze the internal structure of the coma in order to see its interaction with the solar wind. Indeed, the outflowing coma interacts with the solar wind and as activity grows this interaction become more

intense and creates a cavity that 'protect' the nucleus from the solar wind and divert the solar magnetic field (fig. 1.5). Such a cavity, called diamagnetic cavity, was expected to stand in front of the comet by only a few 10's of kilometres, but observations by the RCP-MAG have found that it is much more dynamic, its boundary reaching more than 180 kilometres from the comet.
RSI, Radio Science Investigation, was the system of communication with the antenna on Earth. It worked by using the radio signal oscillation to measure the mass and the gravity of the nucleus, from which it could derive its density and internal structure. RSI determined the mass and density of asteroid Lutetia during its flyby. In addition, the RSI team excluded the possibility that some cavity in the internal structure of the comet could be present. RSI contributed also to define the orbit of comet 67P.

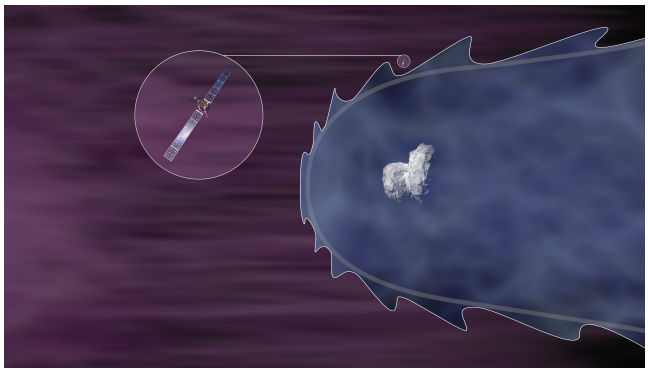

Figure 1.5: Impression of the magnetic field-free region or diamagnetic cavity, shown in blue, caused by the interaction of the comet's coma and the solar wind, shown in purple.

VIRTIS, Visible and InfraRed Thermal Imaging Spectrometer, was a spectrometer which combined, in a single instrument, two channels for the spectral mapping and a channel for spectroscopy. It was used to study solid compounds, map the surface and derive the superficial temperature. It analyzed the physical properties of the coma and provided images to find a suitable site for the landing of Philae. VIRTIS followed the changes in the reflected light from the surface, in the 0.2-5.1μm wavelength range, revealing slightly changes on the superficial layers.
At scales of 15-25 m VIRTIS found that the surface has an homogeneous composition and it is dominated by dust and carbon-rich molecules. Moreover, smaller and bright areas seen in images are likely to be ice-rich and typically they are associated with exposed surfaces or debris piles where collapse of weaker material has occurred, uncovering fresher material (Capaccioni et al. 2015).

The Philae lander was equipped with ten scientific instruments designed to analyze the superficial and sub-superficial composition, and the physical properties of the terrain. The instruments carried by Philae were:
APXS, Alpha-P-X-ray Spectrometer, able to lower within 4 cm of the comet's ground to detect alpha particles and X-rays, which provided information on the elemental

composition of the comet's surface.
CIVA, Panoramic and microscopic imaging system, had six identical micro-cameras which took panoramic photos of the comet. It used a spectrometer to study the composition and albedo of the samples collected from the surface. Images taken by CIVA, before Philae last touchdown, revealed details in the surrounding terrain down to the millimetre scale and also helped decipher Philae's orientation. The images revealed fractures in the comet's cliff walls and the material around seems to be dominated by dark agglomerates, perhaps comprising organic-rich grains. Brighter spots likely represent differences in mineral composition, and may even point to ice-rich materials (Bibring et al. 2015).
CONSERT, Comet Nucleus Sounding Experiment by Radiowave Transmission, probed the comet's interior by studying radio waves that are reflected and scattered by the nucleus. It worked together with the one on the orbiter. In addition, CONSERT was used to help triangulate Philae's location on the surface, with the best fit solution pointing to a 21m×34 m area (Kofman et al. 2015).
COSAC, Cometary Sampling and Composition experiment, was a gas analyser for detection and identification of complex organic molecules from their elemental and molecular composition. It analysed samples entering tubes at the bottom of the lander kicked up during the first touchdown, mainly volatile ingredients of ice-poor dust grains. In this way it revealed a suite of 16 organic compounds comprising numerous carbon and nitrogen-rich ones, including compounds such as methyl isocyanate, acetone, propionaldehyde and acetamide that have never been detected before in comets (Goesmann et al. 2015).
PTOLEMY was an evolved gas analyser, which obtained accurate measurements of isotopic ratios of light elements. It was composed of a chromatograph and a mass spectrometer. Ptolemy sampled the gas entering tubes at the top of the lander and detected the main components of coma gases such as water vapour, carbon monoxide and carbon dioxide. It also sampled a small amount of carbon organic compounds, including formaldehyde which is implicated in the formation of ribose, which features molecules like DNA (Wright et al. 2015).
As a whole some of the compounds detected by Ptolemy and COSAC play a key role in the prebiotic synthesis of amino acids, sugars and nucleotides, which are the elements behind life.
MUPUS, Multi-Purpose Sensors for Surface and Subsurface Science, used sensors on the Lander's anchor, probe and exterior to measure the density, thermal and mechanical properties of the surface. MUPUS provided insight into the physical properties of Abydos site and showed that the surface and subsurface material sampled was substantially harder than that at Agilkia site, as inferred from the mechanical analysis of the first landing. The terrain had a thin layer of dust, less than 3 cm thick, covering a much harder compacted mixture of dust and ice at Abydos. At Agilkia this harder layer may exist at a greater depth than that encountered by Philae.
The MUPUS thermal sensor revealed a variation in the local temperature between about -180°C and -145°C in synchronization with the comet's 12.4 hour day. The thermal inertia implied by the measured rapid rise and fall in the temperature also indicates a thin layer of dust covering a compacted dust-ice crust (Biele et al. 2015).

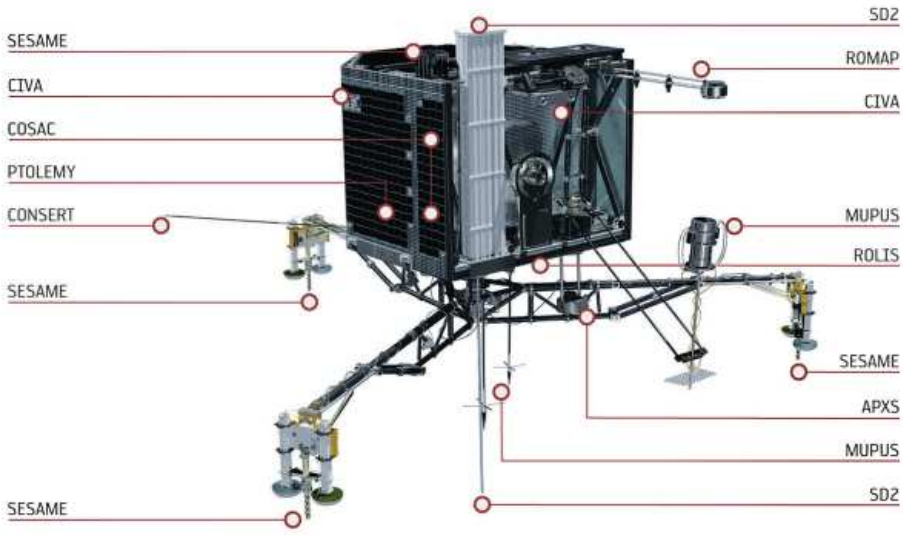

Figure 1.6: Representation of scientific instruments on board the lander Philae.

ROLIS, Rosetta Lander Imaging System, was a CCD camera to obtain high resolution images during descent and stereo panoramic images of areas sampled by other instruments. ROLIS images taken shortly before the first touchdown revealed a surface comprising metre-size blocks of diverse shapes, coarse regolith with grain sizes of 10–50 cm and granules less than 10 cm across. It revealed that the regolith at Agilkia is thought to extend to a depth of 2 m in places, but seems to be free from fine-grained dust deposits at the resolution of the images. Furthermore the largest boulder in the ROLIS field of view measures about 5 m high, with a peculiar bumpy structure and fracture lines running through it, that suggest erosional forces are working to fragment the comet's boulders into smaller pieces. The boulder has also a tapered tail of debris behind it, yielding clues of how particles lifted up from one part of the eroding comet are deposited elsewhere (Mottola et al. 2015).
ROMAP, Rosetta Lander Magnetometer and Plasma Monitor, was an instrument for the study of the local magnetic field and for the study of the comet and solar-wind interaction. ROMAP was crucial on defining the site of the second touchdown of Philae, as seen in section 1.2.
SD2, Sample and Distribution Device, was a system to drill more than 20 cm into the surface, collect samples and deliver them to different ovens or for microscope inspection, however as Philae does not anchored itself on the surface it was hard for SD2 to drill into the surface .
SESAME, Surface Electrical Sounding and Acoustic Monitoring Experiments, was a set of three instruments to measure the properties of the comet's outer layers. The Cometary Acoustic Sounding Surface Experiment (CASSE) measured the way in which sound travels through the surface, the Permittivity Probe (PP) investigated its electrical characteristics and the Dust Impact Monitor (DIM) measured dust falling back

to the surface.

Chapter 2

Comet 67P/Churyumov-Gerasimenko

Comet 67P/Churyumov-Gerasimenko is named after its discoverers Klim Churyumov and Svetlana Gerasimenko. It was first observed in 1969 during a survey of comets at the Alma-Ata Astrophysical Institute in Kazakhstan, and in particular it was recognized by Churyumov while he was examining a photograph of comet 32P/Comas Solá, taken by Svetlana Gerasimenko.
Comet 67P is classified as a short period comet, i.e. a comet characterized by orbital period of less than 20 years and low orbital inclination. Since its orbit is influenced by Jupiter's gravity, comet 67P belongs to the Jupiter Family comets. Short period comets include also the so called type Halley comets, whose orbital period ranges between 20 and 200 years. Lots of these comets perform a retrograde motion and display a high orbital inclination, between 0 and 90°. It is thought that short period comets originate from the Kuiper Belt (Davis and Farinella 2001), a large reservoir of small icy bodies located beyond Neptune. Some of these bodies are ejected into the inner Solar System towards the Sun, as a result of collisions or gravitational perturbations. Indeed, comets

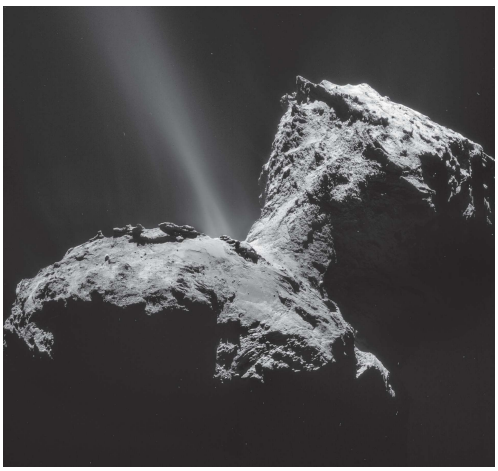

Figure 2.1: Comet 67P/Churyumov-Gerasimenko.

gravitationally interact with Jupiter as they cross its orbit, subsequently the orbit of

the comets gradually change, and they are eventually thrown out of the Solar System or collide with a planet or the Sun.
Before Rosetta rendez-vous comet 67P, on 11-12 March 2003 some images of comet have been acquired by the Hubble Space Telescope (HST). However, it was only with the images acquired by Rosetta that it was discovered the comet's real shape, which is composed of two lobes connected by a narrower region, hereafter neck. The overall dimension of the nucleus is 4.34 × 2.60 × 2.12 km, while the bigger lobe, called body, has dimensions of 4.10 × 3.52 × 1.63 km, and the smaller lobe, called head, is 2.50 × 2.14 × 1.64 km (Sierks et al. 2015). The neck features only the 7% of the entire volume.
The comet has a mass of 1.0×10^{13} kg and a volume of 18.7 km^3, from which it can be inferred a density of 533 kg/m^3 (Sierks et al. 2015). The low value of the density, less than half the density of the water, implies a high porosity of the comet.
The mean rotational period of comet 67P is 12.404 hours. This value changes along the orbit between 12.305 at perihelion, and 12.430 hours at aphelion, because of the torque due to non-gravitational forces (Jorda et al. 2016). The comet performs a prograde and elliptical orbit around the Sun with a revolution period of 6.45 years. The orbit has an eccentricity of 0.640 and an inclination of 7.04° with respect to the ecliptic plane. The perihelion and aphelion distances from the Sun are 1.243 AU and 5.682 AU respectively.
The spin axis of the comet has an inclination of 52° (Mottola et al. 2015), which leads to a strong seasonal variation of the insolation conditions. Indeed, the maximum insolation occurs at perihelion, the southern hemisphere is totally illuminated and part of the north is in shadow. In addition, the peculiar bilobed shape of the comet, together with the conformation of the neck, leads also to a diurnal variation in the surface illumination. The combined effect of seasonal and diurnal insolation is the origin of a high thermal gradient in the south of the comet. This affects the erosion activity due to ice sublimation which is higher by a factor of four in the southern hemisphere (H. Keller et al. 2015).

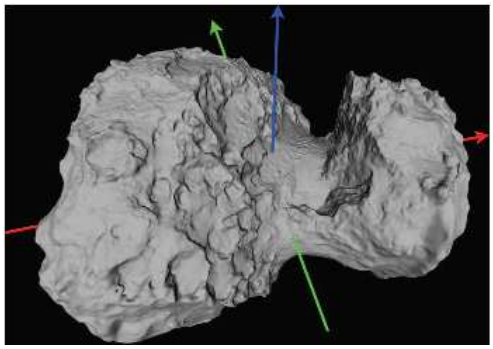

Figure 2.2: Shape model of comet 67P. The blue arrow indicates comet's rotation axis z, the red and green arrows display its equatorial x and y axes (Sierks et al. 2015).

Nucleus dimensions	4.34 km × 2.60 km × 2.12 km
Mass	1.0×10^{13} kg
Density	533 kg/m^3
Rotation period	12.4 h
Revolution period	6.45 years
Orbit inclination	7.04°
Spin axis inclination	52°
Orbit eccentricity	0.640

Table 2.1: Physical properties of comet 67P.

2.1 Constraints on its origin and shape

Concerning the origin of comets and kilometer-sized planetesimals in general, there are two main competing formation models, the *gravitational collapse of a pebble cloud* and *hierarchical collisional growth*. The gravitational collapse of a pebble cloud take place when primordial micrometer-sized dust and ice grains coagulate into pebbles, which cannot stick to each other because of the bouncing barrier, that prevents dust aggregates from growing larger than millimeter size. Pebbles are locally concentrated by many possible processes, for example by turbulent concentration or sedimentation until the streaming instability is triggered. When pebbles have accreted their size, the gravitational collapse can directly forms planetesimals with sizes up to 1000 km (Herique et al. 2019).
In the *hierarchical collisional growth*, particles coagulate in pebbles, which are able to overcome the bouncing barrier and continue to grow by mass transfer.
A study on the homogeneity of comet 67P as seen by CONSERT showed that the scenario that generate porosity heterogeneities at a scale smaller than one meter, is compatible with the model of a gentle gravitational collapse of a pebble cloud, which does not show heterogeneities on size scales larger than the pebble size, that is of a few centimeters (Herique et al. 2019). Thus, the predicted porosity of 73–78 % of planetesimals formed by gravitational collapse of a pebble cloud is in full agreement with the results obtained by CONSERT (Herique et al. 2019).
When high resolutions images of the comet have been detected in 2014, comet 67P revealed a peculiar bilobed shape. From that moment on different scenarios have been considered to explain its bilobed structure, although it is a still debated question. The comet's shape could be attributed to its primordial origin as well as to evolutionary effects that comet experienced along its orbit. Some of the hypothesis invoked define the comet as the result of the fusion of two objects initially separated or as a single body which has thinned in correspondence of its central part because of erosion and activity.
From the analysis of the OSIRIS images performed by Massironi et al. 2015, it has been found that the major lobe is enveloped by a nearly continuous set of strata, with a thickness up to 650 metres, the minor lobe has an independent envelope, while the neck lacks of an envelope stratum. Terraces and cuestas were the hints of a stratified

internal structure for the comet. These features have already been observed on the surface of comet 9P/Tempel 1 (Peter Thomas et al. 2007, Pious Thomas et al. 2013). Their origin has been explained either as the result of sublimation, or as the expression of an inner stratified structure related to the comet's primordial origin (Massironi et al. 2015). Using the best-fitting planes of terraces and cuesta-like features obtained from the stereo-photoclinometry shape model it has been discovered that strata are coherently oriented all around the comet, suggesting two separate strata envelopes for the head and the body lobe (Massironi et al. 2015).
Therefore the formation hypothesis which derives from the layering is that comet 67P is an accreted body of two distinct objects with 'onion-like' stratification, which formed before they merged. Thus, two independent kilometre-sized cometesimals accreted through gentle and low-velocity collisions in the primordial Solar System (Massironi et al. 2015). The two lobes display structural similarities which involve the onion-like structure as well as the surface features and composition, suggesting that the two cometesimals have passed through similar accretion processes. Based on the orientation and distribution of the identified strata, it is possible that the two lobes formed as pebble-pile planetesimals consisting of aggregates of primordial pebbles from the Solar nebula (Jansson and Johansen 2014).

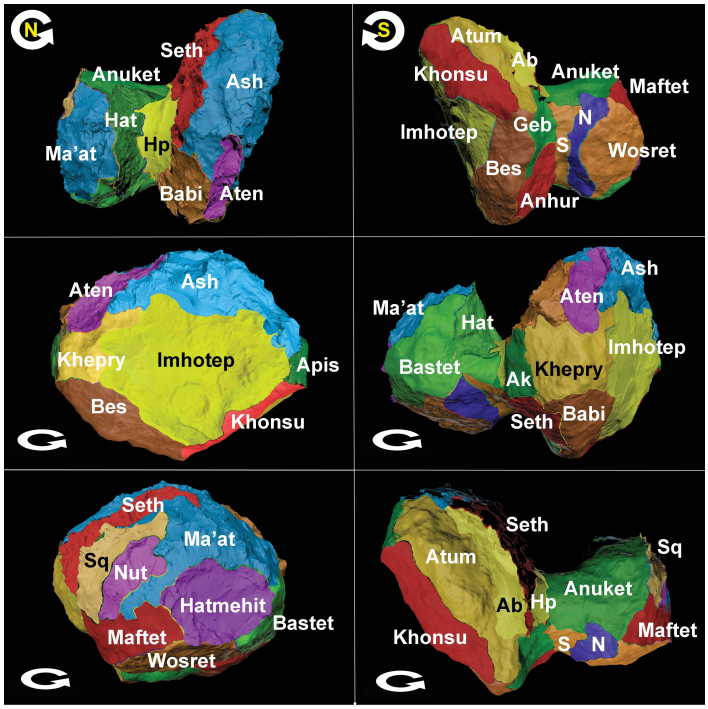

Figure 2.3: Six different viewing angles showing the 26 physiographic regions of comet 67P (El-Maarry et al. 2015b).

2.2 Morphology of the surface

Starting from May 2014 the OSIRIS camera acquired high resolution images of the comet surface at a distance lower than 100 km. Images revealed a complex surface morphology which is likely the expression of different processes which occurred at different times on the cometary nucleus.
The surface of the comet has been divided in 26 physiographic regions, 19 in the Northern hemisphere and 7 in the Southern hemisphere (Fig. 2.3). Each region is marked by different geological features and is named after ancient Egyptian deities. Regions on the smaller lobe were given female names, whereas regions on the larger lobe and on the neck were assigned male names, according to the general theme of the Rosetta mission in using ancient Egyptian names.
The surface of the nucleus displays a remarkable morphological diversity that can be classified into three main categories: consolidated regions, non-consolidated regions and large irregular depressions (El-Maarry, N. Thomas, Giacomini, et al. 2015).
Consolidated regions are units that appear rocky and cohesive, they often have the shape of outcrops and can display lineaments and fractures. Consolidated regions represent the most common region type on both lobes and it is very likely that they identify the terrain constituting the bulk of the nucleus. These materials on the comet could be fully exposed, partially buried by dust or enclose smooth terrains.
Consolidated regions are further divided in *strongly consolidated*, which show variable degrees of fracturing and *brittle* or *weakly consolidated* units, which have a high concentration of circular pits, and mass-wasting deposits in alcove-like features. These units are mainly located in the Seth and Babi region on the body lobe, and to a much lesser extent in Bastet and Ma'at on the head lobe (El-Maarry, N. Thomas, Giacomini, et al. 2015).
Non-consolidated regions comprise two main sub categories: smooth terrains and dust covered regions (Giacomini et al. 2016). *Smooth terrains* are generally covered with smooth deposits showing ripple and dune-like features. They occasionally contain boulders and may represent areas of current or past activity. Smooth terrains mainly characterize Imhotep and Anubis on the body lobe, and Hapi in the neck region. They can be found also in other regions as isolated areas. On the other hand, *dust-covered regions* mainly encompass the Ash and Ma'at regions and to a small extent Seth and Babi on the body lobe, and Anuket and Maftet on the head lobe. In some areas the dust cover gradually thins out, exposing the internal materials (Giacomini et al. 2016).
Finally large *irregularly-shaped depressions* are mainly represented by Hatmehit and Nut on the head lobe, and Aten and Anubis on the body lobe. They are characterised by mass-wasting or talus-like deposits. These depression could be at the origin of strong surface activity, indeed they often lack of a dust coverage (El-Maarry, N. Thomas, Giacomini, et al. 2015).
Other geologic units which characterise the regions described above are fine particle deposits and mass wasting deposits (Fig. 2.4a). In particular, all the areas covered by a fine material are classified as *fine particle deposits*. ROLIS data showed that these deposits have a granular aspect and dimensions down to centimetre size (Mottola et al. 2015, Pajola, Oklay, et al. 2016). Most of the larger lobe's surface, in particular the

Ash, Aten, Seth, Kephry and Babi regions, is covered by fine particle deposits. Their wide distribution on the Northern hemisphere can be due to the strong Southern activity at perihelion passage (N. Thomas, Davidsson, et al. 2015). *Mass wasting deposits* are deposits of material mainly located at the foot of steep walls, therefore they are thought to have been formed by the collapse of cliffs (J. Vincent et al. 2016).
Mass wasting deposits have different surface textures, morphologies and placement, thus they are further classified in: taluses, gravitational accumulation deposits and diamictons. *Taluses* are generally constituted by granular material and often show some larger blocks (Fig. 2.4d), (Pajola, J.B. Vincent, et al. 2015). *Gravitational accumu-*

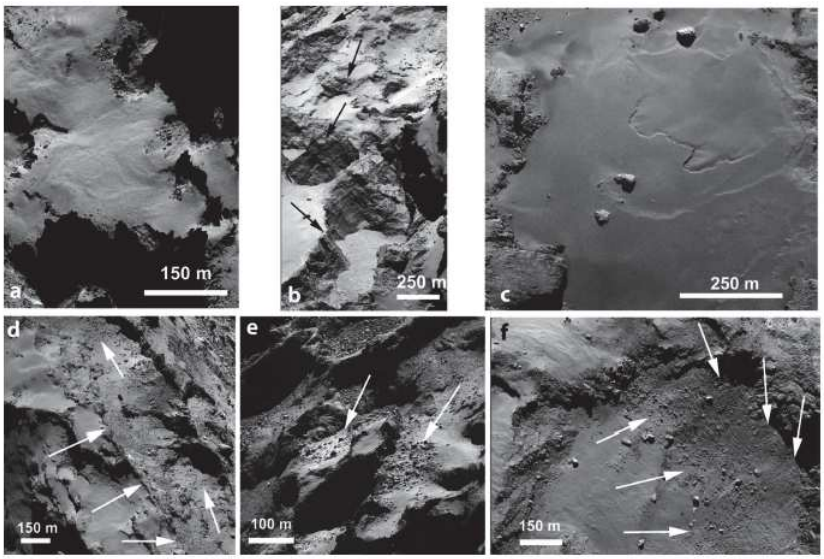

Figure 2.4: On the top examples of: (a) Fine particle deposits, (b) outcrops of consolidated terrain (indicated by black arrows) and (c) smooth terrains. On bottom: d) aluses (indicated by white arrows), (e) gravitational accumulation deposits and (f) diamicton (Giacomini et al. 2016).

lation deposits are composed of a material with a wide range of diameters, including large boulders from 2 to 30 m of diameter (Pajola, J.B. Vincent, et al. 2015) (Fig. 2.4e). *Diamicton deposits* involve poorly sorted material and their source region is still not clear (Fig. 2.4f, Giacomini et al. 2016).
Finally, the lineaments which characterize the consolidated regions are classified as: fractures, cuesta ridges or terrace margins, niches and strata. *Fractures* are mainly generated from stress activities and the consequently loss of cohesion in the terrain (Fig. 2.5a). When fractures cut the strata head suggest that fracturing process is younger than the layering. *Cuestas* are asymmetric ridges formed in the presence of tilted strata (Fig. 2.5b, Massironi et al. 2015, Pajola, J.B. Vincent, et al. 2015). When the strata are slightly inclined, the differential erosion creates terraces (Massironi et al. 2015, Pajola, Oklay, et al. 2016). On the Seth region (Fig. 2.6) terraces alternates with semicircular scarps delimiting the areas of material detachment called niches (Fig. 2.5c). *Strata* identify bedding planes which can extend for a few up to hundreds of metres, they are parallel to each other, usually detected on high walls or scarps (Fig.

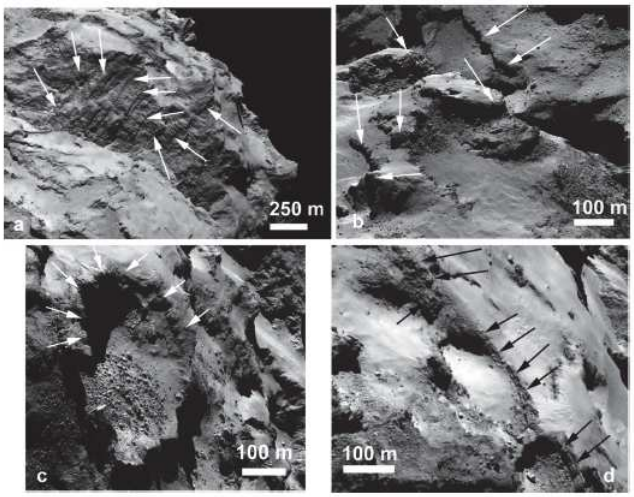

Figure 2.5: Examples of: (a) Fractures (indicated by white arrows) detected in the Hathor region, (b) Cuesta ridges, (c) semicircular niche formed by the detachment of material and (d) some strata (black arrows) detected on the larger lobe of the comet (Giacomini et al. 2016).

2.5d). As said before, strata also suggest the presence of a layered internal structures in 67P's nucleus(Fig. 5d; Massironi et al. 2015).
As expected for comets, 67P/Churyumov–Gerasimenko's surface morphology has been transformed, as it happened with the collapse of the Aswan cliff and the release of new boulders, and it will continue to evolve along its orbit.

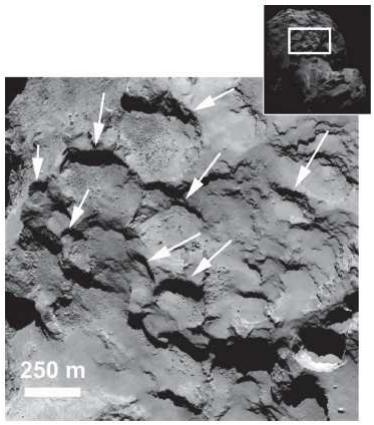

Figure 2.6: An enlarged view of a section of the Seth region showing particular semicircular features (white arrows) (Giacomini et al. 2016).

2.3 Global spectrophotometry

Comet 67P has been observed with different NAC and WAC filters of the OSIRIS instrument at different heliocentric distances along its orbit, providing first a global

view of the comet and then a focused insight on the different regions. As an example, images acquired in 20 filters almost a year before the perihelion passage, have been used to investigate the global spectrophotometric properties of the nucleus by Fornasier et al. 2015. The spectrum of the reflectance (I/F) as a function of the wavelength obtained for the nucleus is shown in Fig. 2.7. The NAC and WAC data are plotted together with a spectrum of comet 67P (gray line) acquired with observation from the ground (Cecilia Tubiana et al. 2008), in the visible and near-infrared range. It follows that OSIRIS spectrophotometry is fully consistent with ground-based observations (Fornasier et al. 2015) in the considered range. Overall, the spectrum of the nucleus diplays a nearly linear trend, with a red slope and no absorption features along visible and near-infrared wavelengths. Some variations are present only at smaller scales (Fornasier et al. 2015).

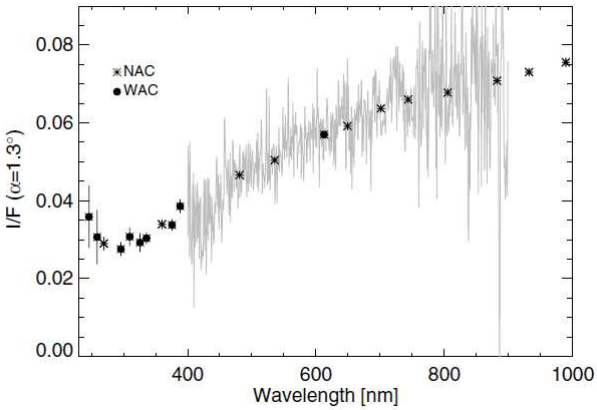

Figure 2.7: Average spectrophotometry of NAC and WAC observations obtained on 28 July (Fornasier et al. 2015). The continuous gray line represents a spectrum of comet 67P taken in 2007 from ground-based observations, when the comet was inactive (Cecilia Tubiana et al. 2008).

Beyond 750 nm the spectral slope appears slightly less steep in the NIR range than in the VIS, this behaviour might be attributed to the coma emissions (Fornasier et al. 2015). From Fig.2.7 it is visible that the flux rises up in the mid-UV (240-270 nm range) and a possible explanation of this broad band, which has a minimum close to 290 nm, may be attributed to SO_2 frost, which was detected by the ROSINA instrument (Fornasier et al. 2015). Compared to the nearby continua the spectra displays also an excess of the flux in the OH filter, centered at 309 nm. This implies that the OH radical, coming from water photodissociation, is also present in the coma, consistently with measurements of the MIRO and ROSINA instruments (Fornasier et al. 2015).
Global spectrophotmetry of the nucleus has been obtained also with the VIRTIS-M instrument, which provided images in the range 0.2-5.1 μm. The VIRTIS-M findings on the spectrum of the nucleus are consistent with the OSIRIS results and in addition they revealed a broad absorption feature from 2.8 to 3.6 μm, centered at 3.2 μm (Capaccioni et al. 2015). After laboratory experiments which recreated the vacuum pressure and low temperature conditions of the nucleus, a recent study proposed the presence of ammonium salts mixed with dust on the surface of comet 67P to justify

this broad absorption feature. The NH_4^+ in ammonium salts seems to be the main responsible for the absorption feature centered at 3.2μm (Poch et al. 2020) visible in the VIRTIS spectra (Fig. 2.8). Indeed it has been detected a similarity on band shapes and positions, both in the nucleus and ammonium salts spectra. The depth of the band suggests that semi-volatile ammonium salts are a substantial reservoir of nitrogen in the comet. Similar absorption features have been detected also in the spectra of some asteroids, implying a compositional link between asteroids, comets and the interstellar cloud from which they originated (Poch et al. 2020).
Concerning the spectrophotometric study we have to consider that data acquired by a spacecraft observing any planet or small body on the observation conditions related to the spacecraft-target position and to the illumination conditions of the surface by the Sun. Data used for the analysis in this study have been acquired at different phase angles. The phase angle is the angle defined between the incidence and emission rays, it is a fundamental parameter to take into account in the spectrophotometric analysis of the comet as it affects the spectral slope and reflectance measurements. The spectral

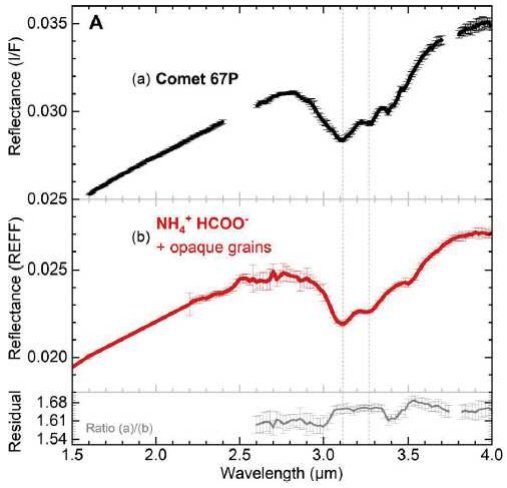

Figure 2.8: Comparison of NH_4^+ $HCOO^-$ spectrum with the average spectrum of comet 67P. Dashed gray vertical lines show that both spectra have the same shape and minima at 3.1 and 3.3 μm (Poch et al. 2020).

slope depends on the phase angle through the phase reddening effect, i. e. the increase in the steepness with increasing phase angles. In Fig. 2.9 it is shown the average spectral slope of the global nucleus obtained from a study performed before perihelion passage with the OSIRIS instrument, in the 535-882 nm range. The plot displays a variation of the slope from 11%/100 nm at a phase angle of 1.3° to 16%/100 nm at a phase angle of 52°, implying a phase reddening of 0.95%/°, which non negligible (Fornasier et al. 2015). Strong phase-reddening effects have been measured also using VIRTIS data, both in the visible (550-800 nm) and near-infrared range (1-2 micron) (Ciarniello et al. 2015). In this case it has been found a smaller phase reddening value, 0.44%/° in the VIS and 0.73%/° in the IR, compared to the one obtained by OSIRIS. This discrepancy has been explained with the different solar phase angle range considered in the two analysis, between 1.3°–53.9° for OSIRIS and between 20°-120° for

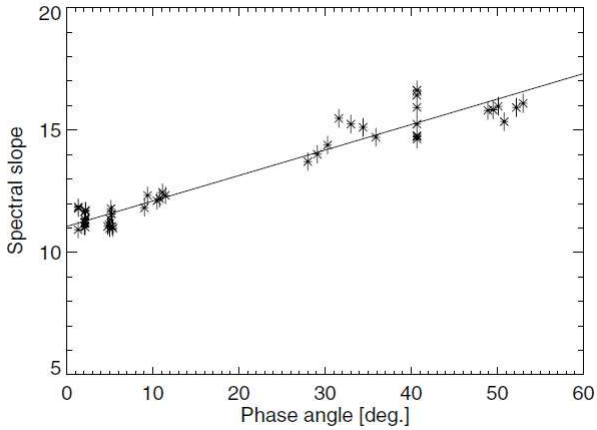

Figure 2.9: Variation of the mean spectral slope of the nucleus evaluated in the 882-535 nm range (Fornasier et al. 2015).

VIRTIS, which is wider. It is the first time that significant phase-reddening effects are detected on a comet nucleus, though this phenomenon is common to many planetary bodies, such as asteroids and icy satellites. Phase reddening is potentially attributed to the increased contribution of the multiple scattering at large phase angles and to the surface roughness (Ciarniello et al. 2015).
As mentioned above, the reflectance displays a phase angle dependence which is stronger at low values of the phase angle, where the phase curve has a peak, while it decreases for higher values of the phase angle. This behaviour is shown in Fig. 4.4, where the phase curve obtained for asteroid 21 Lutetia is plotted. The phase curve behavior of comet 67P has been studied with OSIRIS data acquired before perihelion using the visual magnitude instead of the reflectance (Fig. 2.11). Data have been plotted and interpolated with a linear fit (dashed line), from which it has been derived the linear slope and the magnitude at phase angle 0°, which turn in $\beta = 0.047 \pm 0.002$ mag/° and H_V=16.14 $\pm$ 0.006 mag, respectively. The slope value obtained for the linear fit is close to the average value for Jupiter-family comets ($\beta = 0.053 \pm 0.016$ mag/°, Fornasier et al. 2015). The best fit of the data is obtained with the HG IAU model (continuous line).

From the global spectrophotometry of the nucleus performed both before and after perihelion it has been derived a spectral evolution of the surface which has been ascribed to seasonal effects. Indeed, as shown in Fig. 2.12 the colour evolution of the nucleus is visible which at perihelion has become relatively bluer, i.e. the spectral slope has decreased (Fornasier et al. 2016), compared to red spectral colour that was dominant a year before the perihelion. The spectral blue colour has been interpreted as an abundance of water ice, which becomes higher when the comet's activity increases. Indeed, approaching perihelion because of the low distance from the Sun the volatile elements present on the surface sublimate, as well as the dust cover is partially removed. As a consequence the internal material become exposed attributing to the comet an overall blue aspect. Then, as the comet orbits towards the outer solar system the activity decrease and dust particles settle again on the surface, which retrieve a red

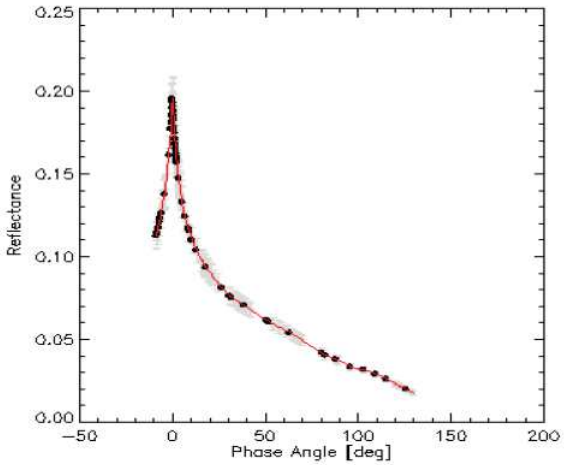

Figure 2.10: Phase curve showing the reflectance trend as a function of the phase angle.

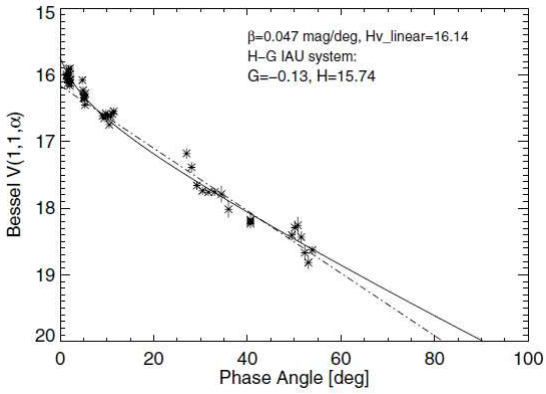

Figure 2.11: Phase curve of the nucleus from OSIRIS observations in the NAC green filter. The continuous line represents the HG IAU model that best fits the data, the linear fit to the data is plotted as the dashed-dotted line (Fornasier et al. 2015)

.

spectral colour. As the bluer aspect at perihelion involves the entire surface, it follows that the water ice component characterize almost the whole nucleus (Fornasier et al. 2016).

A spectrophotometric analysis performed on OSIRIS/NAC images acquired before perihelion by Fornasier et al. 2015 allowed to derive a spectral classification of the global surface. Considering high, medium and dark reflectance regions, the surface has been classified in *low spectral slope* terrains with values of the spectral slope between 11.0 and 14%/100 nm (at a phase angle $\alpha \sim 50°$). These regions are usually referred to as blue regions, showing a higher albedo than the other terrains and are correlated with sources of activity like active pits, alcoves and bright spots (Oklay et al. 2016). Hathor, Hapi, and part of the Seth region belong to this group, as well as portions of Ma'at and Babi. *Average spectral slope* regions have spectral slope values between 14 and 18%/100 nm, (at $\alpha \sim 50°$). Anuket and Serqet are some examples of this group, together with part of the Ma'at and Ash regions. *High spectral slope* regions have a

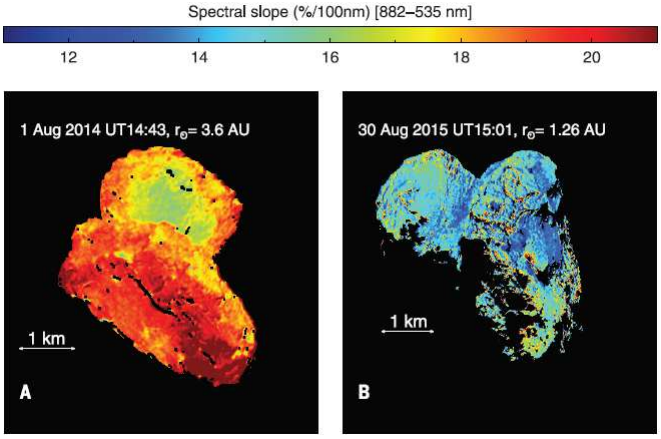

Figure 2.12: Spectral slope maps of the nucleus in early August 2014 and in late August 2015 (Fornasier et al. 2016).

spectral slope above 18%/100 nm (at $\alpha \sim 50°$), and are associated with a red colour and to inactive areas (Oklay et al. 2016). Several regions of the nucleus are associated with this group, although only the Apis region is entirely correlated with it. Regions which partially display high spectral slope values are Hatmehit and Imhotep (Fornasier et al. 2015). Hence, this spectrophotometric global study revealed that reflectance is anticorrelated with the spectral slope on the comet's surface. Subsequently, the work by Oklay et al. 2016 associated the spectral slope values to active, inactive or mixed regions.

2.4 Regional spectrophotometry

Spectrophotometric studies of the surface have been performed locally on regions visible in high resolution NAC images, often acquired at small spacecraft-comet distance. From a regional study of the surface it is possible to investigate if there are local colour and composition variegation, and comparing results obtained at small and large heliocentric distances it is possible to see if some changes have occurred, varying the spectral appearance of the region. In the following, we report the main results obtained for the regions which have been analyzed to date and available in literature. The **Hapi** region, located on the neck of comet, has been spectrophotometrically studied from images acquired before perihelion (on August 2014) with nine NAC filters by Oklay et al. 2016. Hapi displayed the lower spectral slope values and bluer colours of the whole comet and it is characterized by active features and bright patches. In addition, Pajola et al. (2019) considered two sets acquired on August 2014 with the orange filter, revealing that Hapi's spectral slope values are almost 2–3 %/100 nm bluer compared to the surrounding regions. Region of interest located on different geological units, revealed a very slight variegation on the surface. The bluer colour of Hapi has been interpreted with a high content of water-ice, which is also at the base of its high

activity. Water-ice is preserved on Hapi because of its peculiar shape and position, which often cast Hapi in the head or body lobe shadow. In addition, because of the seasonal effects Hapi, as well as great part of the Northern hemisphere, is not illuminated at perihelion, thus the overall homogeneity could be attributed to the dust covering coming from the intense activity of Southern hemisphere (Pajola, Höfner, et al. 2017).

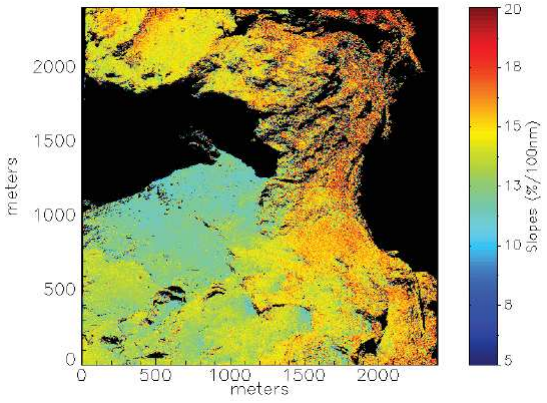

Figure 2.13: Spectral map of the Hapi region and its sorrounding regions: Seth and Anuket. Hapi displays the bluer slope (Oklay et al. 2016).

The **Seth** region on the body lobe is composed of terraces and numerous niches and pits from which high activity has been detected. The geomorphological map of the Seth region displays different geologic units, which correspond to a superficial colour variegation. Seth circular niches have been studied by Lucchetti et al. 2017 before perihelion using a dataset acquired on November 2014, with seven NAC filters, and post-perihelion by use of two sets acquired on July 2016 with three filters. Before the perihelion passage a local heterogeneity in the spectral slope is observed depending on the specific unit, as shown in Fig. 2.14. On average the spectral slope of Seth before and after perihelion has not changed significantly (16.6 $\pm$ 1.4 %/100 nm in the pre-perihelion dataset, 16.8 $\pm$ 2.1 %/100 nm and 16.6 $\pm$ 2.6 %/100 nm in the two post perihelion datasets) even if it displays a higher dispersion (Lucchetti et al. 2017). Compared to the pre-perihelion observations, the post-perihelion analysis displays several bright features close to shadows, that have been interpreted as the presence of water-ice mixed with refractory materials. Bright features show a flat spectrophotometric behavior (Lucchetti et al. 2017).
Located on the Seth region, the Aswan site has been studied with 2 datasets acquired before perihelion on 2014, as it was a candidate landing site for the Philae lander. Aswan is characterized by different morphologic units, however no spectral differences have been detected. This spectral behaviour has been linked to the re-disposition of dust particles coming from cometary activity (Pajola, Oklay, et al. 2016).
The **Imhotep** region has been investigated by Oklay et al. 2016 on images acquired on 2014 along 67P orbit toward perihelion, with seven filters. It displays a variegated surface mainly composed of circular niches, a basin of fine particles deposits and bright

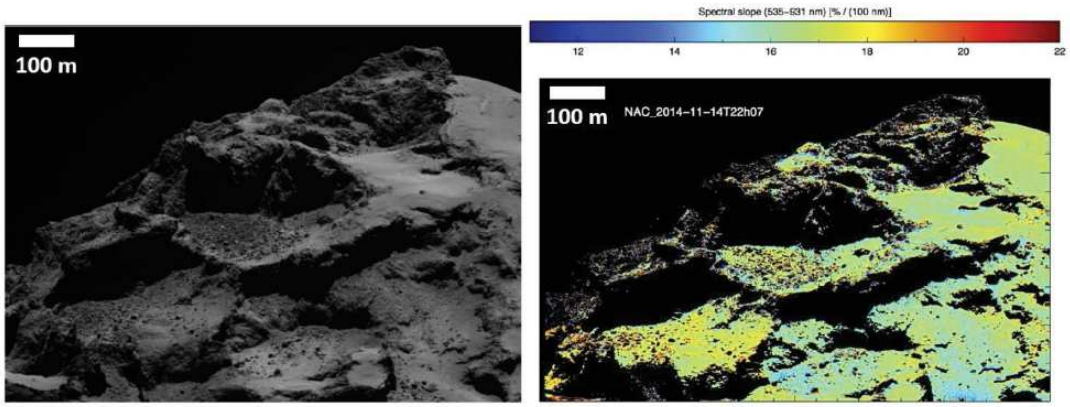

Figure 2.14: Seth's niches and their spectral slope map computed in the 535–931 nm range (Lucchetti et al. 2017).

patches. Overall, the spectral slope behaviour of the bright features is definitely flat, while the surrounding terrain is redder. The presence of water frost has been detected in correspondence of shadows, where it was visible a bluer behaviour compared to the terrain around. This phenomenon was interpreted as due to diurnal presence of morning shadows. In Fig. 2.15 the evolution of the spectral slope near to shadows is shown on Imhotep which varies in less than hour (Fornasier et al. 2016). Imhotep was also investigated by Feller et al. 2019 after the comet perihelion passage, during the April 2016 fly-by. In the Imhotep–Khepry transition, a different spectral behaviour according to different geological units was confirmed. Fine particle deposits show an average reflectance and spectral slope, while consolidated terrains, outcrops and boulders display a lower reflectance and a higher spectral slope.

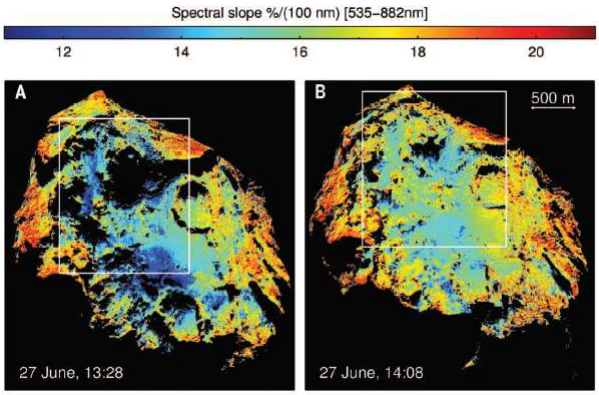

Figure 2.15: Spectral slope maps of Imhotep showing the changes in color due to morning shadows, for images taken 40 minutes apart (Fornasier et al. 2016).

On the head lobe, of particular interest was the landing site of the Philae lander, **Agilkia**, for which it has been performed a geomorphological and spectrophotometrical analysis by La Forgia et al. 2015. The study has been conducted on 9 sets of images

acquired on September 2014. From this analysis a correlation of the spectral slope with the morphological units has been derived, showing a slightly diverse spectral slope for each unit. For example the finest deposits show the highest reflectance and the bluest spectra, followed by taluses and gravitational accumulations, which are slightly darker and redder (Fig. 2.16). The diamictons have the widest spread in spectral behavior, which could be attributed to their variety in texture. Finally, outcrops are the darkest and reddest material (La Forgia et al. 2015). A correlation between morphology and

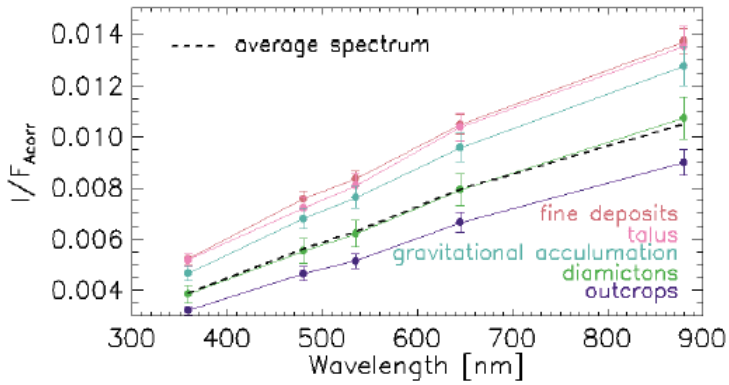

Figure 2.16: Low resolution spectra obtained on different types of terrains (La Forgia et al. 2015), dashed line represents the overall average spectrum.

colors has been highlighted as the fine material deposits show the bluest colors and from fine to rough material the colors gradually becomes redder. In addition, some color differences are observed within the same geological unit (La Forgia et al. 2015). The variations of the spectral slope and colors with the morphology of the terrain have been interpreted as an indication of a chemical composition variegation (La Forgia et al. 2015), indeed the bluest regions are ice rich, while the reddest are characterised by organic compounds. Finally, it has been detected a link between reflectance and morphology, with an higher reflectance for the fine deposits of material and the lowest reflectance for the consolidated terrains.

Spectrophotometric studies have been performed also in the Southern hemisphere, which is dominated by consolidated material compared to the North. Because of the strong activity to which it is exposed during perihelion, it is thought that it reveals the comet's pristine nature.

The **Anhur-Bes** regions belong to this hemisphere and their spectral behaviour has been studied with sets of images acquired both before and after perihelion by Fornasier et al. 2017. A significant phase reddening for images acquired post-perihelion has been detected at larger heliocentric distances, in particular images acquired at the same phase angle display an increase in the slope from 14.9 %/100 nm, in 2015, to 16.4 %/100 nm, in 2016. Bright patches with bluer spectral slope have been detected both before and after perihelion, suggesting a composition of water ice for the surface. On 2014 an extended bright feature of CO_2 was visible for less than three weeks, while another extended patch of water ice was visible for almost ten days.

The **Khonsu** region is characterized by a variety of geological features, whose spectral

behaviour has been studied by Deshapriya et al. 2016, both before and after perihelion by use of two sets of images acquired in nine NAC filters. From the spectrophoto-

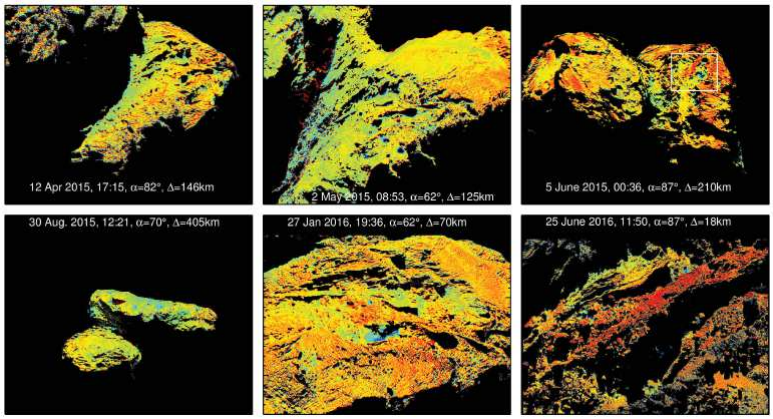

Figure 2.17: Spectral slope map of the Anhur-Bes region for images acquired from April 2015 to June 2016 (Fornasier et al. 2017).

metrical analysis, the different geologic units display a slight variation in reflectance, with smooth terrain showing the highest reflectance, whereas consolidated terrains have the lowest reflectance. Overall the different geologic units share a red spectral behaviour, thus according to the spectral classification mentioned above, Khonsu has been classified as an average spectral slope region. Some bluer areas have been observed especially after the perihelion passage, with a spectral slopes of 11%/100 nm, resulting to be dominated by water ice.

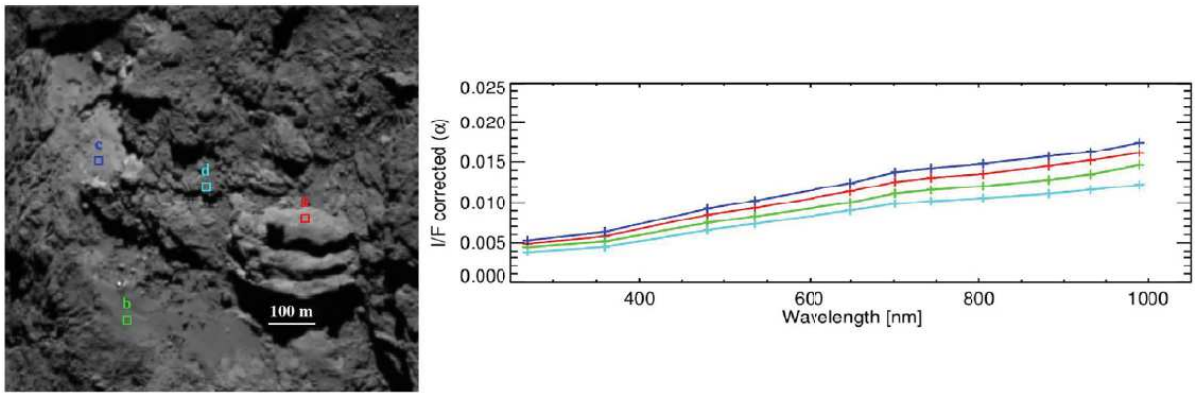

Figure 2.18: Different geological features on the Khonsu region, the spectrophotmetric analysis has been performed on the selected boxes (on the left). On the right the spectrum of the reflectance as a function of the wavelength obtained for each box (Deshapriya et al. 2016).

A study performed on six regions of the body lobe: Ash, Apis, Atum, Khonsu, Bes and Imhotep by Ferrari et al. 2018 has related the different colour of the surface with the internal layering of comet. The analysis was made with two datasets acquired after perihelion (on January 2016) with nine NAC filters. Taking into account the onion-like structure of the comet (Massironi et al. 2015) the relation between the spectral

slope and the comet's layering has been investigated. By use of the elevation model (EM) which models the layered structure of the nucleus, two classes of autochthonous terrains have been identified: the outer and the inner class, distinguished by spectral properties. The *outer class* is darker and located on the outermost stack of layers of the big lobe. Some examples of this class can be found along Ash, Apis and the tops of Khonsu, Atum and Bes regions. The *inner class* is brighter at all wavelengths and can be found on the innermost outcrops of Imhotep, Bes and Khonsu (Ferrari et al. 2018). The inner class displays a higher reflectance with respect to the outer one, i.e the outer layers are the reddest. The photometric variegation determined between the two classes is associated with the different surface brightness, which is probably linked to the texture of the consolidated terrain or to a different composition and content of refractory materials (Ferrari et al. 2018). The brighter inner layers appearance is linked to a recent exposure due to the removal of outer layers as a consequence of intense activity.

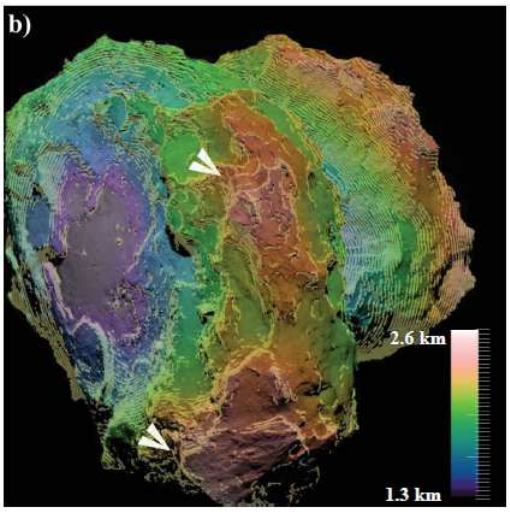

Figure 2.19: Innermost and outermost layers of the big lobe obtained with an ellipsoid model, in blue are shown the innermost layers, in red the outermost layers (Penasa et al. 2017).

2.4.1 Ice exposure

OSIRIS NAC and WAC camera provided us images under changing illumination conditions and variable spatial resolution, in different wavelength bands. Although comet 67P globally displays a uniform gray color, it has been possible to identify over one hundred meter-sized bright spots in numerous types of geomorphologic regions, mostly located in areas receiving low insolation.
The observed bright features have been classified into three categories (Pommerol et al. 2015): *clusters of bright features* presenting more than three bright spots (Fig. 2.20), *isolated bright features* consisting of up to three features in close vicinity (Fig. 2.21), and *boulders displaying bright patches at their surface* (Fig. 2.22). Isolated bright spots can be observed in all types of regions, as on consolidated areas or lying on smooth dust units, as in the Ash region. In some cases the bright spot seems to be part of the

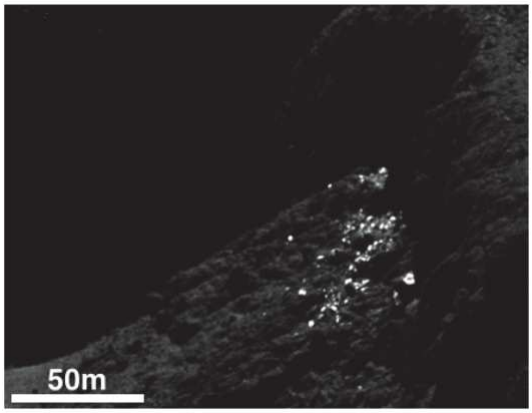

Figure 2.20: Example of clusters of bright spots observed at Khepry. They consist of few tens of meter-sized boulders spread over a few tens of meters (Pommerol et al. 2015).

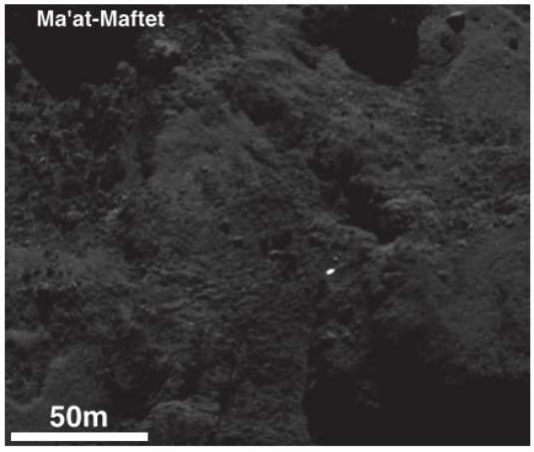

Figure 2.21: Example of isolated bright spots observed at the boundary between Ma'at and Maftet (Pommerol et al. 2015).

unit over which it appears, in other cases it seems to have a different source origin. In particular, the collapse of walls and mass wasting processes seem to be responsible for the meter-sized exposures of ice (Pommerol et al. 2015). Thus, clustered bright spots could have been formed by the collapse of overhang material, while isolated spots could be boulders that have been redeposited in a different location because of low velocity emissions. From high resolution observations it appears that bright spots occupy only a fraction of the boulder's surface in which they appear. Thus, most of the surface of the boulder shows a reflectance similar to the surrounding terrain, and the bright fraction only occupies a minor part of the boulder's surface (Pommerol et al. 2015).
As mentioned above, an example of extended bright patches are the one located on the the Anhur/Bes regions. In this case, taking into account the period of time in which ice was visible, it has been estimated the thickness of the ice layer which ranges between 1.5 and 27 mm for the ice patches. The presence of a hard icy layer has been detected also in the Abydos site by the Philae lander (Fornasier et al. 2016). It follows that

when dust has been removed from the surface, the icy layers are exposed, suggesting a local heterogeneity in the surface composition.

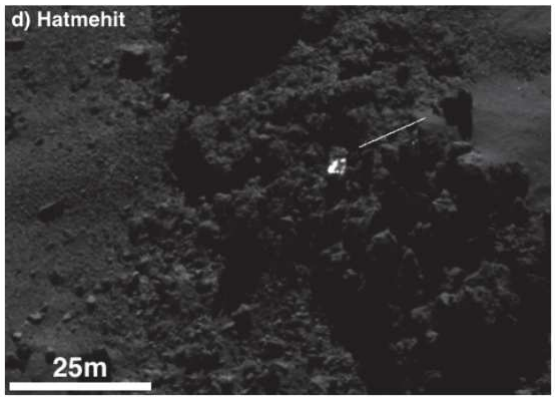

Figure 2.22: Example of a boulder, located in the Hatmehit region, displaying a bright patch on its surface (Pommerol et al. 2015).

The bright material characterizing bright features has been interpreted invoking the presence of ices, as they show the high reflectivity required to explain the observations. Various ices, H_2O, CO_2, and CO would be consistent with both the brightness and color of bright spots mixed with dust, however at the heliocentric distances at which the observations were made, super-volatiles such as CO and CO_2 would sublimate very rapidly if exposed to direct solar illumination. Thus the exposure of H_2O ice at the surface of boulders is the most plausible scenario, indeed water ice sublimates at a lower rate which is compatible with the OSIRIS observations (Pommerol et al. 2015).
The results of laboratory experiments [1] offer additional support for this hypothesis by demonstrating how the sublimation of a mixture of H_2O ice with mineral and organic dust can reproduce the spectrophotometric properties observed on the nucleus, to a first approximation (Pommerol et al. 2015). Thus, the relatively dark and red surface of the nucleus, only punctuated by the meter-scale bright spots, can be explained by the presence of a thin dust mantle composed of refractory mineral and organic material. As shown by laboratory experiments, some portions of the dust mantle can be easily removed if they lack of a strong cohesion with the underlying material. Finally, the exposed water ice will sublimate with time, at different rates depending on the heliocentric distance, forming a new dust mantle at the surface of the icy features.

[1]The KOSI experiments conducted at the DLR in the 1980s on the behavior of H_2O and CO_2 ices mixed with mineral contaminants under simulated comet surface conditions (Pommerol et al. 2015).

2.5 Coma

As comet approaches perihelion, surface activity is triggered by the strong solar irradiation, which causes sublimation of volatile molecules on the surface, and the removal of the dust coating due to the coupled action of the sublimating gas and rotation of comet. The overall coma of comet 67P was visible since March 2014 at a heliocentric distance of about 4.3 AU (Tubiana et al. 2015), while approaching perihelion cometary activity is continuously powered by several faint outbursts, with a variable duration that sometimes is extremely short, just few minutes. Outbursts are events similar to an explosion in the subsurface, releasing a large amount of material in a very short time relatively to other forms of activity such as jets and continuous outgassing (Vincent et al. 2016b). Outbursts can origin when high pressure develops under superficial layers leading to the formation of a small pit or depression and the subsequent exposure of fresh volatile material that continue to sublimate. Moreover, on comet 67P it has been revealed that the same area can outbursts shortly after noon or early in the morning (Fornasier et al. 2015), following the presence of shadows.These events are periodic and follow the sublimation and recondensation of water ice. As most outbursts are located near cliffs presenting evidence of mass wasting, another possible mechanism invoked to explain the origin of outbursts is the collapse of a cliff, which could cause the release of large quantities of dust, without the need for local ice reservoirs, or specific illumination conditions. Activity triggered by cliff's collapse require a gas flow to accelerate the dust away from the surface.

From mid-July 2014, when comet was at $\sim$ 3.7-3.6 AU, the OSIRIS camera observed a clearly non-isotropic dust coma, which pointed out the presence of dust jets, whose appearance changes with nucleus rotation and with date (Lara et al. 2015). Since the start of the monitoring phase, the dust jets were most prominent in the northern part of the coma, and they seemed to originate from the center of the Hapi region (Sierks et al. 2015, Lara et al. 2015). Then, different active areas have been identified over the nucleus, for example during July and August 2014, i. e. at perihelion, active areas pertain to the Hapi, Hathor, Anuket, Ma'at, Serqet, Ash, and Aten regions (Lara et al. 2015). Later, the number of identified active sources has increased. All of these active regions show distinct geomorphological features: Hapi has a very smooth terrain, Hathor, Hapi, Seth and Ma'at display a low spectral slope (Fornasier et al. 2015) and high albedo, while Anuket and Serqet are slightly redder than Hapi. Therefore, although the global comet activity is driven by solar insolation, there are some distinct areas where activity is enhanced and gas and dust are emitted in the form of large-scale dust jets.

Overall, it seems that the main driver of jets is insolation coupled with local compositional inhomogeneities, i.e. areas that are brighter and have colors relatively bluer than the dark terrain of the comet, indicating a local enrichment in volatiles that once illuminated sublimate (Fornasier et al. 2018). Indeed, sources of jets are usually found below cliffs, scarps, or inside cavities or alcoves, which are often in shadow, but they are also found on smooth terrains (Fornasier et al. 2018). Moreover, because of comet's complex shape and morphology, a contribution is also given by varying diurnal illumination cycles that the nucleus experience on different locations. Indeed, outbursts

have been detected either in the early morning or shortly after the local noon. The main source of periodic activity on comet 67P has been identified on the sublimation of water ice through the comet's porous mantle (Fornasier et al. 2018).

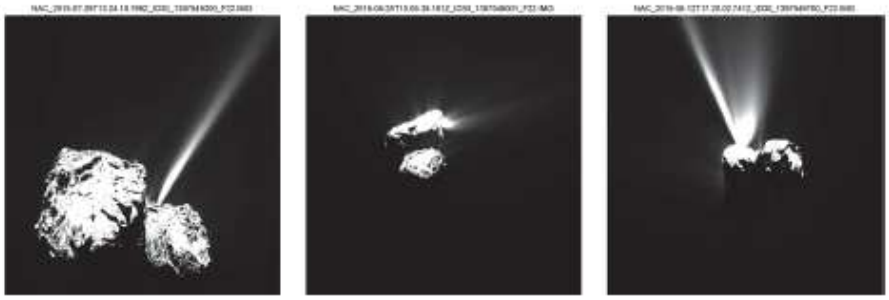

Figure 2.23: Three morphologies of outbursts defined as jet, broad plume, and complex jets (Vincent et al. 2016b).

The VIRTIS instruments observations at perihelion provided important information on the composition of the coma. In particular it has been possible to identify the fluorescence emission lines of H_2O, CO_2, $^{13}CO_2$, OCS and CH_4 (Bockelee-Morvan et al. 2016). Comparing the production rate of gas species with respect to water that are released from the two hemispheres, it follows that the southern hemisphere is up to a factor of 10 more productive in CO_2 and OCS relative to water, and by a factor of 2-5 more productive in CH_4 (Bockelee-Morvan et al. 2016). This trend has been attributed to the strong differences in illumination conditions experienced by the two hemispheres at perihelion. The detection of low levels of CO_2 production from the northern hemisphere indicates that probably most of the CO_2 ice was below the level of the thermal wave, with only a small portion of CO_2 ice reached by the heat (Bockelee-Morvan et al. 2016). Moreover, based on modelling, the low CO_2/H_2O ratio measured in the northern hemisphere during summer (1-3 %) could be not original, but the result of the devolatilization of the uppermost layers (Bockelee-Morvan et al. 2016).
Production rate ratios relative to water of CO_2, OCS and CH_4 have been measured in other comets, and display variations by a factor of up to ~ 10. The CO_2/H_2O ratio measured post-perihelion indicates that comet 67P is CO_2-rich. The OCS/H_2O ratio is in the range of values measured in other comets, though the post-perihelion value is slightly above the mean value of $\sim 0.1\%$ (Biver and Bockelee-Morvan 2015). The CH_4/H_2O ratio in 67P is also within the range of the values measured in other comets.

The comet perihelion passage allowed the Rosetta spacecraft to closely monitor the comet activity, thus a large amount of OSIRIS images clearly have revealed the presence of individual dust grains, characterizing the overall coma.
Dust analysis showed that several complex processes act on the grains, modifying their release and movements. As a consequence of water sublimation, at perihelion dust grains are removed and accelerated by gas drag, thus part of them exceed the escape velocity (about 1 m s^{-1}) and leaves the cometary coma (N. Thomas, Davidsson, et al. 2015), while another part falls back on the surface (La Forgia et al. 2015).

Spectrophotometry has been applied to study dust grains properties, by use of OSIRIS NAC images in different filters. This kind of analysis allowed the spectral classification of dust particles according to their colour and composition. As an example, using images acquired from 2015 July to 2016 January, Frattin et al. 2017 identified three types of dust grain spectra, which includes very steep slope spectra (>15 % /100 nm), spectra with intermediate slope values (5–15 %/100 nm) and spectra presenting a flat slope trend (<5 %/100 nm). Following this classification, grains have been grouped into three categories to classify their relative composition: organics in the case of steep slope spectra, this group well fit the spectral behaviour of nucleus dust terrains, a mixture of organics and silicates in the intermediate slope values and a much higher abundance of ices or carbonaceous material in the case of lowest slope values (Fig. 2.24). The intermediate group is the most populated.

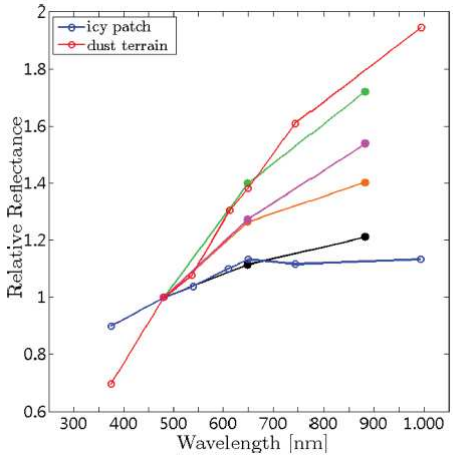

Figure 2.24: Comparison of normalized spectra of dust grains and of two terrains (in red, a dust terrain and in blue an ice patch). In green an example of a very steep slope grain spectrum, it is related with the dust terrain (red) and probably mostly composed by organics; the two intermediate slope spectra (pink and orange) are associated with a mixture of organics and silicates and the flatter spectrum (black) is similar to the one of an icy patch and likely composed by water ice (Frattin et al. 2017).

Chapter 3

Spectrophotometric analysis

The aim of this work is to perform a spectrophotometric study of the Anubis region, in order to analyse its surface variegation in terms of the spectral slope values. Moreover, the main objective is to compare the Anubis spectrophotometric properties before and after the perihelion passage, in order to see if evolutionary processes have operated on the surface of this region, changing its spectral appearance. Finally, we aim to investigate the spectrophotometric properties of a potential bright boulder located at the border of the Anubis and Seth regions.
As previously mentioned, the nucleus has been divided in 26 physiographic regions (El-Maarry at al. 2015b), most of which have been investigated by means of spectrophotometric and geomorphologic analysis (Deshapriya et al. 2016, Ferrari et al. 2018, Fornasier et al. 2019, La Forgia et al. 2015, Lucchetti et al. 2017, Oklay et al. 2016, Pajola et al. 2016). Regions which have already been studied are: Khepry, Seth (Lucchetti et al. 2017), Imhotep (Oklay et al. 2016), Ash , Anhur and Bes (Fornasier et al. 2017), Khonsu (Deshapriya et al. 2016), Hapi , Hatmehit (La Forgia et al. 2015, Lucchetti et al. 2016b), Nut, Maftet, Bastet and Ma'at. Thus, we have researched on the available literature which regions were still missing this kind of analysis. It has been found that Aker, Anubis, Apis, Aten, Babi and Geb on the body lobe, Anuket, Hathor and Neith on the head lobe, and Sobek on the neck have not been investigated yet.
We focused on images acquired with the OSIRIS/NAC camera which are collected in the OSIRIS calibrated Archive. In order to choose an interesting region to study, the first step was to create a catalogue of the images in which regions not yet spectrophotometrically analysed were visible and illuminated. In the OSIRIS Archive are collected all the data acquired from this instrument during the Rosetta mission, including data concerning the flyby with Earth, Mars and asteroids 21 Lutetia and 2867 Steins. The calibrated Archive of comet 67P images consists of a total of nearly 100 000 images sorted in order of acquisition time and in particular arranged in 35 different folders corresponding to the 35 Medium-Term-Planning observational periods. Each Medium-Term-Planning (MTP) period covers a time interval of almost four weeks. MTPs are further divided into Short-Term Planning-cycle (STP), which are observational periods corresponding to nearly a week. Within each STP, images are further divided

in "sequences" which are identified by a tag describing the scientific motivation for that sequence. Different sequences have been acquired with different exposure times according to the aim of the sequence. For example the sequences dedicated to the morphology and spectrophotometry of the nucleus have exposure times chosen to optimize the signal of the comet surface (exposure tag NUCLEUS), while sequences dedicated to the coma have been acquired with exposure times chosen to optimize the signal of the coma (exposure tag COMA), which might mean that the nucleus is saturated in those sequences. The catalogue created for this work is based on images acquired with exposure tag named NUCLEUS. In agreement with the aim of this work, the catalogue takes into account the sequence COLOR MAP, which comprises images dedicated to the study of the colors and spectrophotometry of the comet surface. Depending on the number of filters used for these observations, different types of information can be retrieved on the characteristics and colors of the surface. There were some MTPs lacking a COLOR MAP sequence. In this case we choose to catalogue the images within the sequences tagged SHAPE, that is observations realised for a 3D shape reconstruction of the comet.
Hence, the catalogue that has been generated for this study is made of datasets taken among the sequences tagged COLOR MAP and SHAPE. For each dataset the information reported on the catalogue are: MTP's and STP's number, tag name, number of filters used for the acquisition of images, date and time of the acquisition, name of the visible regions available for a new spectrophotometric study, the lobe and hemisphere to which the classified regions belong, the phase angle and the spacecraft-comet distance. Knowing the distance between the spacecraft and the comet the resolution of the images has been estimated, which have been classified as low, intermediate and high resolution respectively for values above 6 m/pix, from 2 to 6 m/pix and below 2 m/pix . Using the resolution of the images as a parameter, a good candidate for the spectrophotometric analysis seems to be the region with high resolution images acquired both before and after perihelion passage. According to this criterion it has been chosen to analyse the Anubis region on the body lobe (Fig. 3.1).

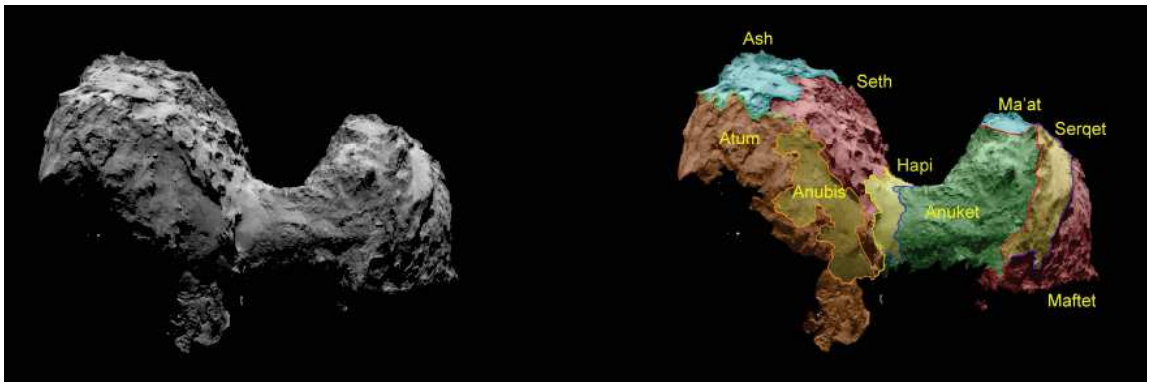

Figure 3.1: Image showing the Anubis location on the body lobe of comet 67P and the regions around it.

The catalogue realised for this work could find further applications in the future,

for example concerning the spectrophotometry of the regions still available for this kind of investigation. In general, it is useful to have a rapid access to sequences in which is visible a specific region, to information on the illumination conditions of a specific dataset, to retrieve high resolution images and to know the distance of the spacecraft from the target at a given instant of the spacecraft orbit.

3.1 Dataset

In this work level 4 calibrated images have been used for the analysis, images downloaded from the spacecraft system undergo a series of calibrations in order to be used for the data analysis. Level 0 images are the raw data gathered from the spacecraft, level 1 are raw images calibrated with the header information, such as hardware parameters and spacecraft information. Raw images are then calibrated with the OSIRIS scientific calibration pipeline, OsiCalliope, a software package that converts the raw images (level 1) to radiometrically calibrated images through a series of operations, including bias subtraction, flat field correction, dark current and bad pixels removal (Tubiana et al. 2015). Level 3 images are corrected for geometric distorsion and finally level 4 images are georeferenced. Indeed, level 4 images have been used to built the shape model of comet 67P, they contain additional geometric references, the maps of the coordinates and of the illumination angles, which are built pixel by pixel.
Three datasets have been selected consisting respectively on 11, 11 and 9 images acquired on 22 May 2015 (pre-perihelion), 9 January 2016 and 28 January 2016. The first two datasets are well suited to investigate the seasonal evolution of the Anubis surface since they have been acquired respectively almost three months before and five months after the perihelion passage of the comet, which was on 13 August 2015. The pre-perihelion cube has been acquired at a phase angle $\alpha = 61°$, with a resolution of 2.3 m/pix. At the acquisition time of the images the spacecraft was at a distance of 126 km from the comet. The post-perihelion cube has been acquired at a phase angle $\alpha = 90°$, with a resolution of 1.4 m/pix. At the time of acquisition of the images the spacecraft was at 77 km from the comet.
The third dataset has been selcted to analyse the spectral behaviour of a boulder located at the boundary of the Anubis and Seth region, with a bright feature on it respect to the surrounding terrain. This dataset belongs to the SHAP7a, a sequence used for the shape model of the comet. This dataset has been acquired on 28 January 2016 at 00:22, after the perihelion passage, at a phase angle $\alpha = 62°$. It has a resolution of 1.2 m/px, and was acquired when the spacecraft was at a distance of 67 km from the spacecraft.
Fig. 3.2, 3.3, 3.4 on the right panels have been produced using the stereo-photoclinometry (SPC) shape model. Two main techniques have been developed to retrieve 3D global shapes of small bodies from OSIRIS images: stereo-photoclinometry (SPC) and stereo-photogrammetry (SPG) (Preusker et al. 2017). These comet's shape models have been developed from a three-dimensional mathematical model of the cometary surface and using high resolution OSIRIS images of the nucleus.

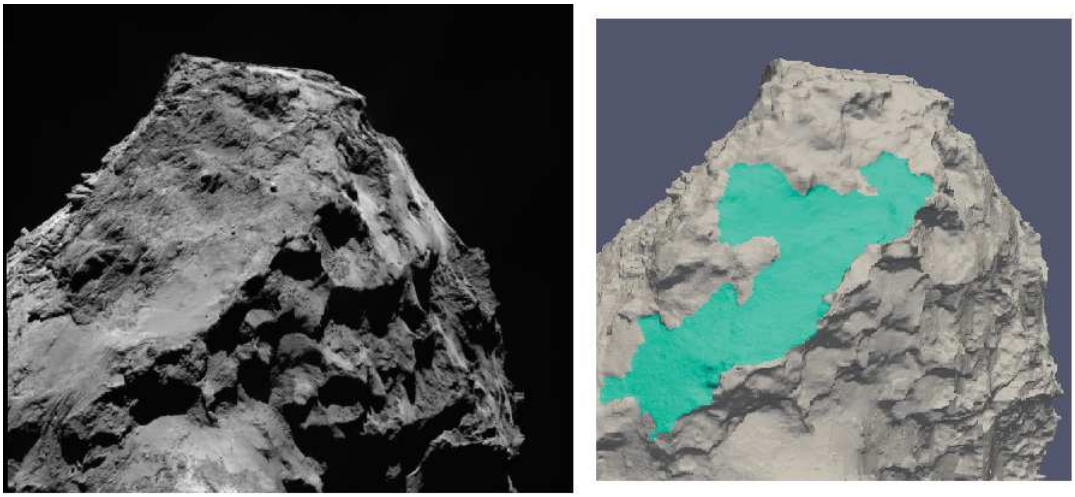

Figure 3.2: The reference image for dataset 1, on the right the Anubis region has been selected in light blue, as a comparison on 67P shape model.

Figure 3.3: The reference image for dataset 2, on the right the Anubis region has been selected in light blue, as a comparison on 67P shape model.

We refer to datasets as dataset 1, 2 and 3, as reported in Tab. 4.1. Each dataset is composed of images acquired with the OSIRIS/NAC camera, with broad band filters in a wavelength range between 250 and 1000 nm (Tubiana et al. 2015b). All datasets have been acquired entirely within nearly three minutes.
In the following paragraph it will be discussed the correction and transformation applied to the datasets in order to obtain low-resolution spectra of the surface of the Anubis region.

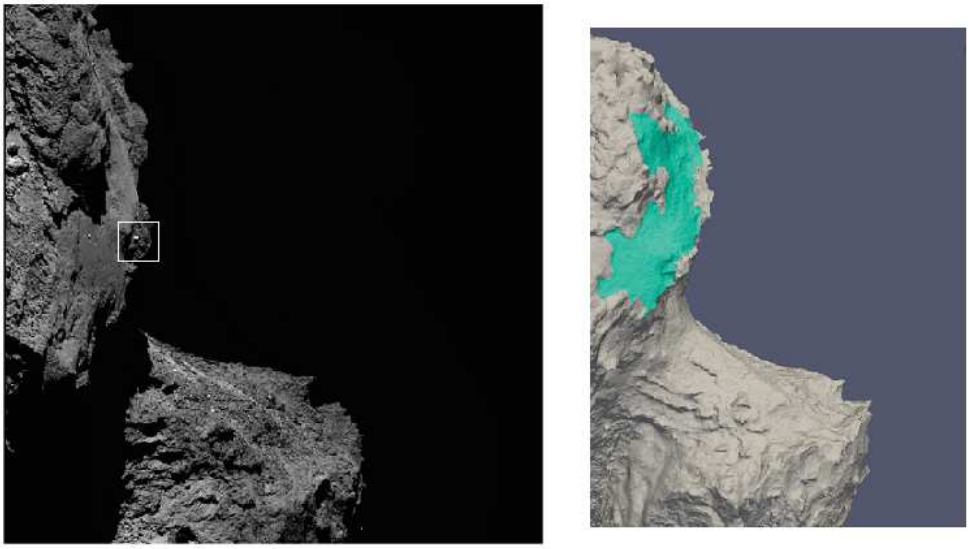

Figure 3.4: The reference image for dataset 3, on the right the Anubis region has been selected in light blue, as a comparison on 67P shape model.

Dataset	Sequence	Date, time	Scale [m/px]	α[°]	r_h[AU]
1	MTP016P/ STP057/ COLORMAP RASTER	2015-05-22 18:57:52 - 18:59:59	2.3	61	1.59
2	MTP024P/STP090/ COLORMAP002	2016-01-9 18:03:27 - 18:05:46	1.4	90	2.09
3	MTP025P/STP093/ SHAP7a	2016-01-28 00:22:31 - 00:24:11	1.2	62	2.22

Table 3.1: The main characteristics of the datasets used in this study: the OSIRIS NAC sequences, the date and time of acquisition of images, the spatial resolution in m/px, the phase angle α and the heliocentric distance in AU.

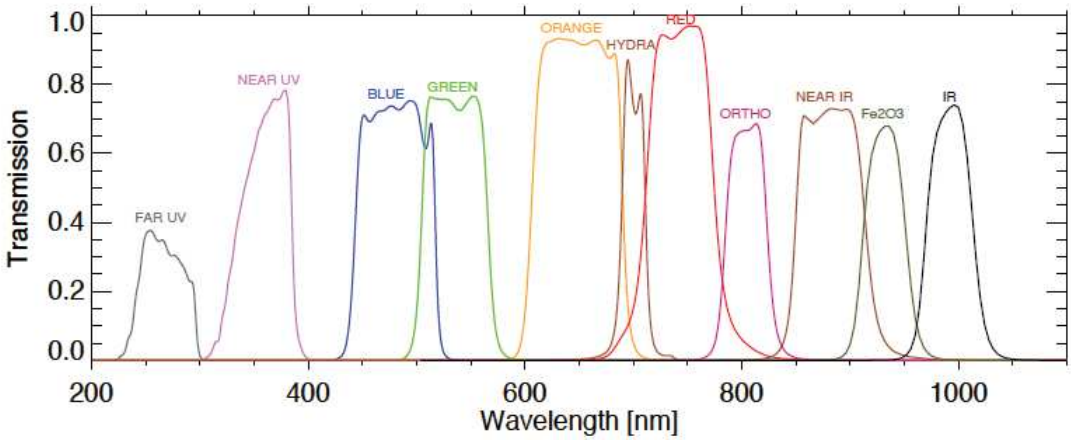

Figure 3.5: Transmission curves of the NAC filters.

Filter name	Filter ID	Wavelength	Dataset
Far-UV	15	269.3 nm	1, 2, 3
Near-UV	16	360.0 nm	1, 2
Blue	24	480.7 nm	1, 2, 3
Green	23	535.7 nm	1, 2, 3
Orange	22	649.2 nm	1, 2, 3
Hydra	27	701.2 nm	1, 2, 3
Red	28	743.2 nm	1, 2, 3
Ortho	51	805.3 nm	1, 2
NIR	41	882.1 nm	1, 2, 3
Fe_2O_3	61	931.9 nm	1, 2, 3
IR	71	989.3 nm	1, 2, 3

Table 3.2: Name, number and central wavelength of the NAC filters used to acquire images for each dataset.

3.2 Conversion to reflectance

As mentioned above, OSIRIS level 4 images have been calibrated in radiance, expressed in $\mathrm{W\,m^2\,nm^{-1}\,sr^{-1}}$, using the OSIRIS standard calibration pipeline (Tubiana et al. 2015b). However, the radiance observed is due to the solar irradiation, which is partially absorbed and re-emitted in a different way from the surface, depending on the material on the terrain. For the spectrophotometric analysis it is fundamental to convert each image from radiance to reflectance units, that is to normalize the measured radiance to the solar radiance received by the comet. This step is essential in order to retrieve information on the surface which reflects the radiation. In particular reflectance values are lower for dark terrains, while they are higher for bright terrains. The procedure of conversion to reflectance is made pixel by pixel for each image of the datasets. Reflectance is a dimensionless quantity, defined as:

$$I/F_{meas,\lambda} = \frac{\pi I_{meas}}{F_{Sun,\lambda}} \tag{3.1}$$

where I_{meas} is the measured radiance of the comet. $F_{Sun,\lambda}$ is the solar irradiance at the heliocentric distance of the comet (r_h) and it is retrieved for each filter as:

$$F_{Sun,\lambda} = \frac{F_{central,\lambda}}{r_h^2} \tag{3.2}$$

where $F_{central,\lambda}$ is the solar irradiance at 1 AU measured at the central wavelength of each filter, $\pi/F_{Sun,\lambda}$ is also called "absolute calibration factor" and depends on the wavelength and on the heliocentric distance of the comet. The heliocentric distance is measured in AU and for dataset 1, 2 and 3 it is 1.59, 2.09 and 2.22 AU, respectively. The variation of the r_h value among the images of each dataset is so small that it has been assumed constant. The heliocentric distance values have been obtained as the difference of the vector Sun-spacecraft and of the vector spacecraft-comet, whose

values are reported on the headers of the images in km. Then, computing the modulus of the vector and converting to AU we obtained the r_h values.

3.3 Warping the images

The second procedure to apply on the images in order to perform a correct spectrophotometric analysis is the co-registration of the images in different filters within each cube. Indeed, the images of each dataset acquired in different filters are not recorded simultaneously but sequentially, over a time interval of less than three minutes. Despite the short interval, there is a delay of few seconds between two consecutive images and because of the rotation of the comet and the spacecraft motion during the acquisition of the images, the field of view of each image is slightly shifted and rotated. Therefore, images acquired in the same sequence with different filters need to be co-registered in order to perform a correct spectral analysis.
A reference image has been chosen for each dataset and all the other images have been warped with respect to the reference one. The reference image is the image acquired in the middle of the acquisition time of each dataset. Some control points equally spaced on the visible portion of the comet have been selected and the warping procedure is achieved by use of the IDL WARP TRI function, that is a linear interpolation method to align the coordinates of each image to the coordinates of the reference image. The warping procedure has been tested over 100, 169 and 225 control points, then for each set of control points it has been computed the correlation coefficient between the x, y and z coordinates of the warped images with respect to the coordinates of the reference image. Indeed, the correlation coefficient provide an estimate of the goodness of the warping procedure, which is higher for values similar to 1. The best correlation coefficient has been obtained using 225 control points (Tab. 3.3) thus, in this work, the images have been warped by means of 225 control points.
Finally, the images converted to reflectance and coregistered have been sorted for increasing values of the filter wavelength and collected in a multispectral image, named cube. A cube has been created for each dataset and it has been used for the spectrophotometric analysis.

3.4 Topographic and photometric correction

The local variations in the observed reflectance of the surface of the comet in each filter are due to three main factors: the different morphology and elevation of the terrain, the observation and illumination conditions, and the true chemical composition of the terrain. Our aim is to investigate the true chemical composition and spectral properties of the terrain. In order to get rid of the topography of the terrain and of the observation and illumination conditions to a first order we performed a topographic/photometric correction.
The topographic/photometric correction allows to transpose the three-dimensional sur-

Dataset	Control points	x corr. coeff.	y corr. coeff.	z corr. coeff.
1	100	0.997172	0.998583	0.998409
	169	0.997374	0.998428	0.998354
	225	0.998100	0.998738	0.998554
2	100	0.997155	0.999530	0.998361
	169	0.997215	0.999545	0.998449
	225	0.997508	0.999548	0.998520
3	100	0.999441	0.998728	0.999795
	169	0.999562	0.998987	0.999821
	225	0.999571	0.999075	0.999842

Table 3.3: Correlation coefficients for the x, y and z coordinates for each datset as an estimate of the warping goodness.

face of the comet to a bi-dimensional plane, for both smooth and sharp morphologies. To perform this correction it is necessary to know the maps of the emission and incidence angles, describing point by point on the surface the values of these angles. Emission and incidence angles are defined as the angles between the emission and incidence rays respectively, and the normal to the surface in the considered point (Fig. 3.6). Indeed the reflectance value depends on the phase angle, which is the angle between the emission and incidence rays. Thus, these angles change point by point on the surface. Level 4 images used for this work contain maps of the illumination angles (see Fig. 3.21, 3.22, 3.22) as additional layers of the images, in particular we considered the angles maps of the reference image, as all images have been warped to the reference one.
In order to correct the illumination and topographic effects the Akimov disk function has been used. A disk function is a theoretical function which describes the variation of the reflectance on the surface as a function of the emission and incidence angles. In our case, D(α, i, e) has been computed using the maps of the illumination angles of the reference image for each cube. When using a Disk Function for the topographic/photometric correction, the direct dependence on the phase angle is neglected. In our case this is considered adequate since the value of the phase angle does not show significant variations among the images of the cube ($\Delta\alpha \sim 0.00076°$ between the first and last image acquired of the dataset) and also within the same cube (see Fig. 3.23), and since in this study we did not intend to investigate the direct dependence on the phase angle (phase function) which is a different topic and might be argument for future developments. In order to make an accurate correction, in this work values of the emission and incidence angles grater than 85°, which correspond to non observable and non illuminated areas of the surface, have been excluded.

Different disk functions (D) have been proposed to describe the changes in the reflectance due to illumination conditions. The simplest function is the Lommel-Seeliger

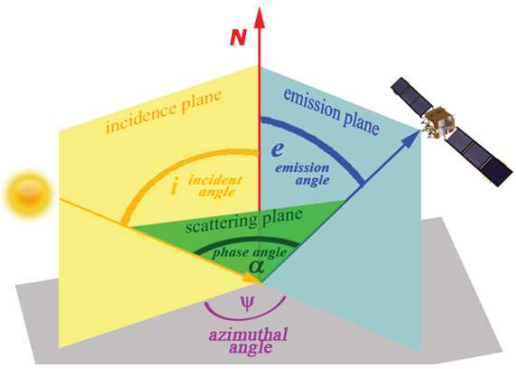

Figure 3.6: Scheme of the emission, incidence and phase angle.

law:

$$D_{LS} = \frac{2\cos i}{\cos i + \cos e} \tag{3.3}$$

a variant of this function takes into account the Lambert scattering law. The Lommel-Seeliger law was adopted by Fornasier et al. 2015 for the global photometric correction of comet 67P. The Minnaert law is an empiric function, which introduces a parameter k depending on the albedo and phase angle:

$$D_M = (\cos i)^k (\cos e)^{(k-1)} \tag{3.4}$$

In this analysis it has been used the parameterless Akimov disk function, indeed the disk function mentioned above have been applied on the analysis of asteroid Vesta and it has been found that by use of the Akimov model it can be achieved almost the same results. Moreover, the Akimov model has been tested on comet 67P itself and compared with the complex Hapke model, showing its goodness in describing the reflectance trend among the surface with the advantage of being parameterless (La Forgia et al. 2015).
The Akimov disk function is defined as:

$$D(\alpha, \beta, \gamma) = \cos\left(\frac{\alpha}{2}\right) \cos\left[\frac{\pi}{\pi - \alpha}\left(\gamma - \frac{\alpha}{2}\right)\right] \frac{\cos(\beta)^{\alpha/(\pi-\alpha)}}{\cos(\gamma)} \tag{3.5}$$

where β and γ are respectively the photometric latitude and longitude, which in turn depend on the incidence, emission and phase angles as follows:

$$\cos i = \cos\beta \cos(\alpha - \gamma) \tag{3.6}$$

$$\cos e = \cos\beta \cos\gamma \tag{3.7}$$

The choice to use the Akimov disk function is also made in order to limit the uncertainties associated to the correction. Indeed, a parameterless function has less uncertainties because it lacks of the introduction of additional conditions linked to parameters.

Therefore, to correct the effects due to topography, illumination and observation conditions, the reflectance has been photometrically corrected pixel by pixel for the Akimov disk function, defining the Akimov corrected reflectance as:

$$I/F_{Acorr,\lambda} = \frac{I/F_{meas,\lambda}}{D(\alpha, i, e)} \tag{3.8}$$

where $I/F_{meas,\lambda}$ is the measured reflectance on the comet's surface. Since level 4 images are provided with maps (pixel by pixel) of e, i, and α, the Akimov Disk function is also computed as an image-map pixel by pixel and the correction is therefore spatially resolved.
Hence, thanks to this correction it has been possible to underline the only changes in the reflectance values due to the heterogeneity of the superficial chemical composition. In the following we will refer to the Akimov corrected reflectance as simply reflectance.

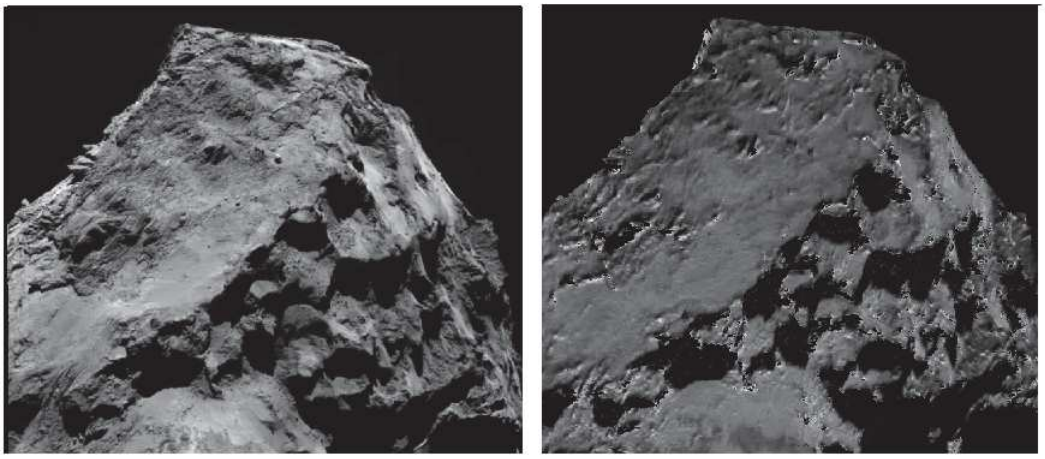

Figure 3.7: Example of the topographic/photometric correction for dataset 1, on the left the original image, on the right the corrected image.

3.5 Resolved spectrophotometry

In order to perform the spectrophotometric analysis some geometric layers have been added to each multispectral cube. In particular the cartesian coordinates have been transformed to spherical coordinates: radius, latitude and longitude. Then for each cube, maps of the latitude and longitude coordinates have been created point by point. Thus, the three cubes are composed of the acquired images plus the maps of emission, incidence and phase angles of the reference image, as well as the comet distance, the x, y and z coordinates of the reference image and the latitude and longitude maps. Hence, the cubes of the datasets 1 and 2 are made of 21 layers and the cube of dataset 3 is made of 19 layers.
At this point, in order to study the spectrophotometric behaviour of the Anubis region the Akimov corrected reflectance has been studied for all available filters as a function of the wavelength in each cube, providing a low-resolution spectrum of the resolved

surface. In particular, different boxes have been selected on the reference image of each cube in order to investigate areas with varying brightness/colors within Anubis. For dataset 1 and 2, five boxes of 16 × 16 pixel, have been selected corresponding to 36.8 × 36.8 m on the surface of the comet for dataset 1 and to 22.4 × 22.4 m for dataset 2. For dataset 3, the selected dimension of the box is 8 × 8 pixel, corresponding to 9.6 × 9.6 m on the comet. The selection of different box dimensions is due to the different spatial resolutions of the datasets and the necessity to describe an area that is sufficiently large to contain the local diversities of the surface. As an example, in the last dataset the aim is to investigate the spectral properties of a boulder respect to the surrounding terrain, thus the dimension of the box has been adapted to the boulder dimension on the images (Fig. 3.8).

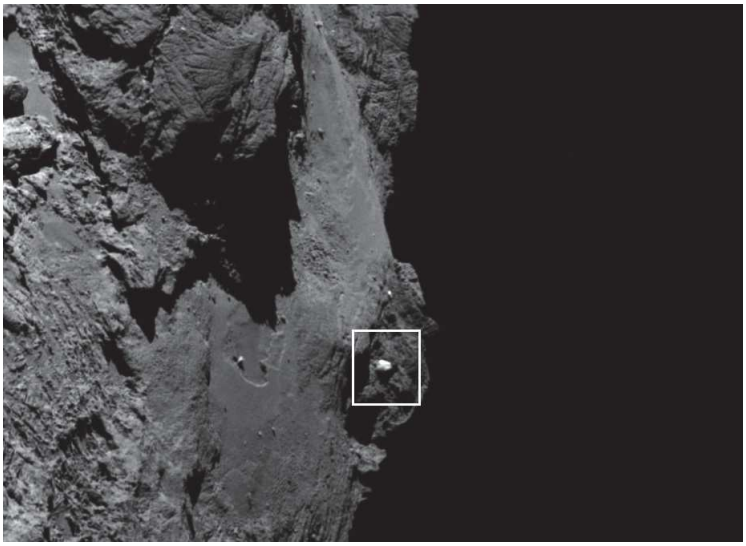

Figure 3.8: Detail of the Anubis region visible in the images of dataset 3. The white box indicates the bright boulder analysed in this work.

Spectra are obtained computing the mean reflectance inside each box for each filter. To compare the evolution of the terrain due to the perihelion passage, boxes with almost the same latitude and longitude coordinates have been selected for dataset 1 and 2. In the third dataset, part of the Anubis region is not observable, thus boxes have been considered in different positions with respect to the other datasets (Tab. 3.4, Fig. 3.9, 3.10, 3.11).
Fig. 3.9, 3.10, 3.11 display the reference image of the cubes and the boxes selected on it. In order to easily recognise the comet's orientation, at the time of acquisition of the images, and the location of the Anubis region on the surface, for each cube it is reported an image of the comet's shape model, in which the Anubis region has been highlighted in light blue (Fig. 3.2, 3.3, 3.4). Indeed Anubis is actually pictured with very different illumination and orientation conditions in the three distinct cases.
Fig. 3.12, 3.13, 3.14 display the low-resolution spectra for the three cubes. Boxes have been selected almost with the same latitude and longitude coordinates for dataset 1 and 2, in order to make an easier comparison.

In addition, relative reflectance plots have been considered (Fig. 3.15, 3.16, 3.17). These spectra have been obtained normalizing the reflectance to the reflectance value at NAC green filter, centred at 535.7 nm. Relative reflectance spectra allow to easily compare the local variations in the spectral slope of the selected areas on the terrain. A quantitative estimate of the differences in the spectral slope values between different location in the same image and between different cubes, is given considering the spectral slope. The spectral slope S, also called reddening, is defined in %/100 nm, as:

$$S = \frac{I/F_{\lambda_{NIR}} - I/F_{\lambda_{Green}}}{I/F_{\lambda_{Green}}} \frac{100 \cdot 100}{\lambda_{NIR} - \lambda_{Green}} \tag{3.9}$$

where $I/F_{\lambda_{NIR}}$ and $I/F_{\lambda_{Green}}$ are the reflectance values in the near-infrared and green filters, at 535.7 nm and 882.1 nm respectively. Values of the spectral slope for each cube in all three datasets are reported in Tab.3.4.
The spectral slope maps (Fig. 3.18, 3.19, 3.20) between near-IR and green show the overall spectral behavior of the comet. It has been obtained applying eq. 3.9, pixel by pixel, over the whole visible surface of the comet. The color bar was chosen so that regions with a lower slope than average are colored in blue and regions with higher slope than the average are colored in red. However the resolution of these spectral maps displays a high roughness to describe the real spectral trend of the surface.

Dataset	Box color	Latitude	Longitude	Spectral slope
1	Black	-33.41°	-113.07°	15.9 ± 0.9 %/100 nm
	Red	-17.60°	-115.25°	15.7 ± 0.9 %/100 nm
	Green	-14.51°	-122.50°	16.1 ± 0.9 %/100 nm
	Blue	-2.40°	-124.52°	14.5 ± 0.9 %/100 nm
	Yellow	6.77°	-135.43°	14.6 ± 0.9 %/100 nm
2	Black	-34.50°	-112.78°	18.0 ± 0.9 %/100 nm
	Red	-17.33°	-115.52°	17.8 ± 0.9 %/100 nm
	Green	-13.03°	-122.09°	18.1 ± 0.9 %/100 nm
	Blue	-3.16°	-125.99°	17.5 ± 0.9 %/100 nm
	Yellow	6.06°	-134.34°	17.0 ± 0.9 %/100 nm
3	Black	-37.24°	-117.63°	17.9 ± 1 %/100 nm
	Red	-34.35°	-113.40°	16.3 ± 1 %/100 nm
	Green	-27.71°	-115.99°	16.8 ± 1 %/100 nm
	Blue	-16.57°	-118.61°	16.6 ± 1 %/100 nm
	Yellow	-24.01°	-109.57°	22.6 ± 1 %/100 nm

Table 3.4: Values of the latitude, longitude and spectral slope of the selected box for each dataset.

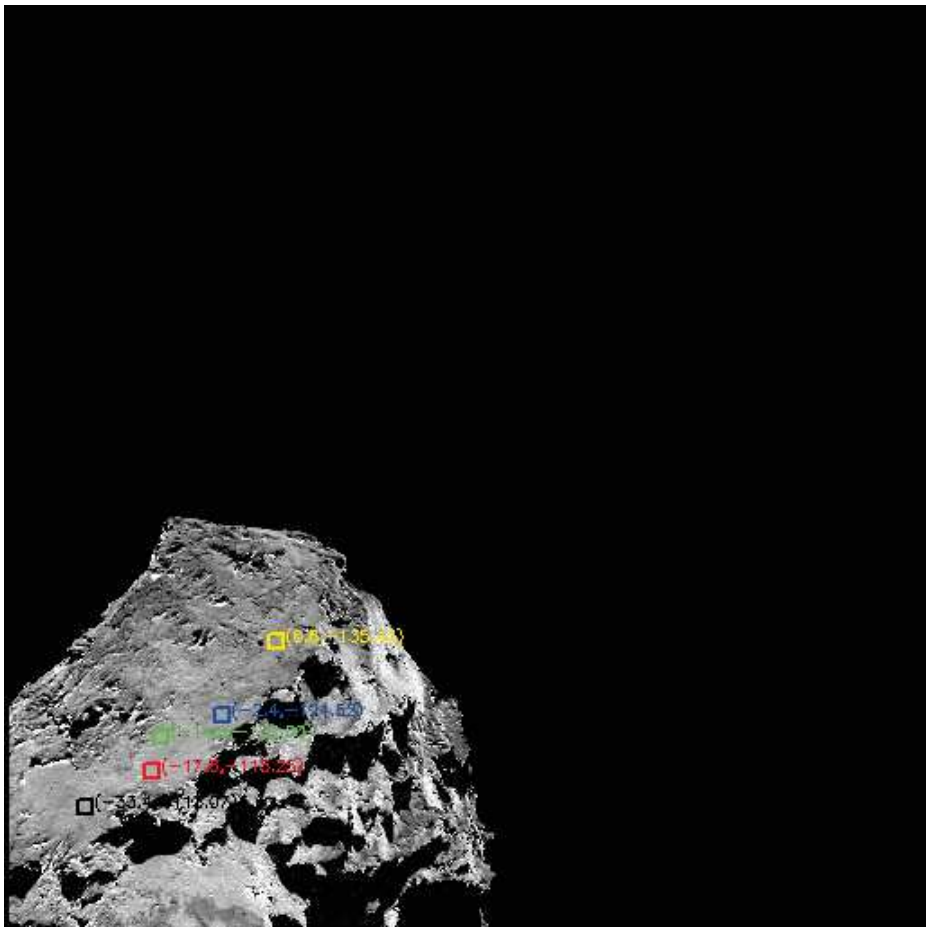

Figure 3.9: The reference image (F27) for dataset 1 and selection of five boxes of 16 × 16 pixel on the Anubis region.

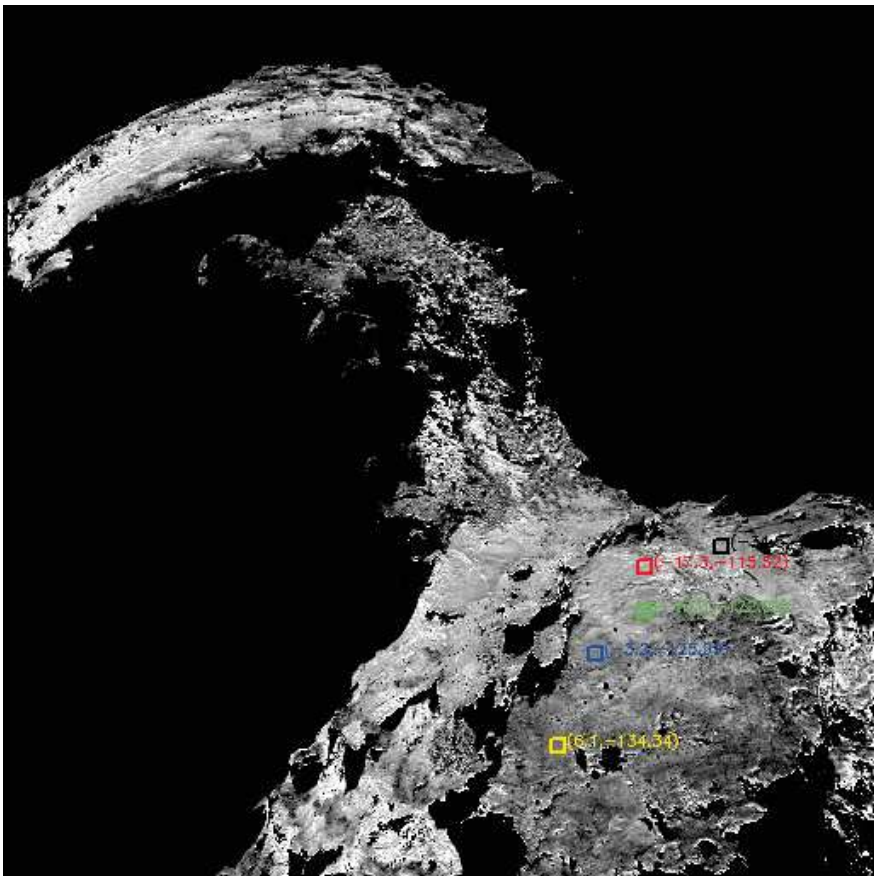

Figure 3.10: the reference image (F28) for dataset 2 and selection of five boxes of 16 × 16 pixel on the Anubis region.

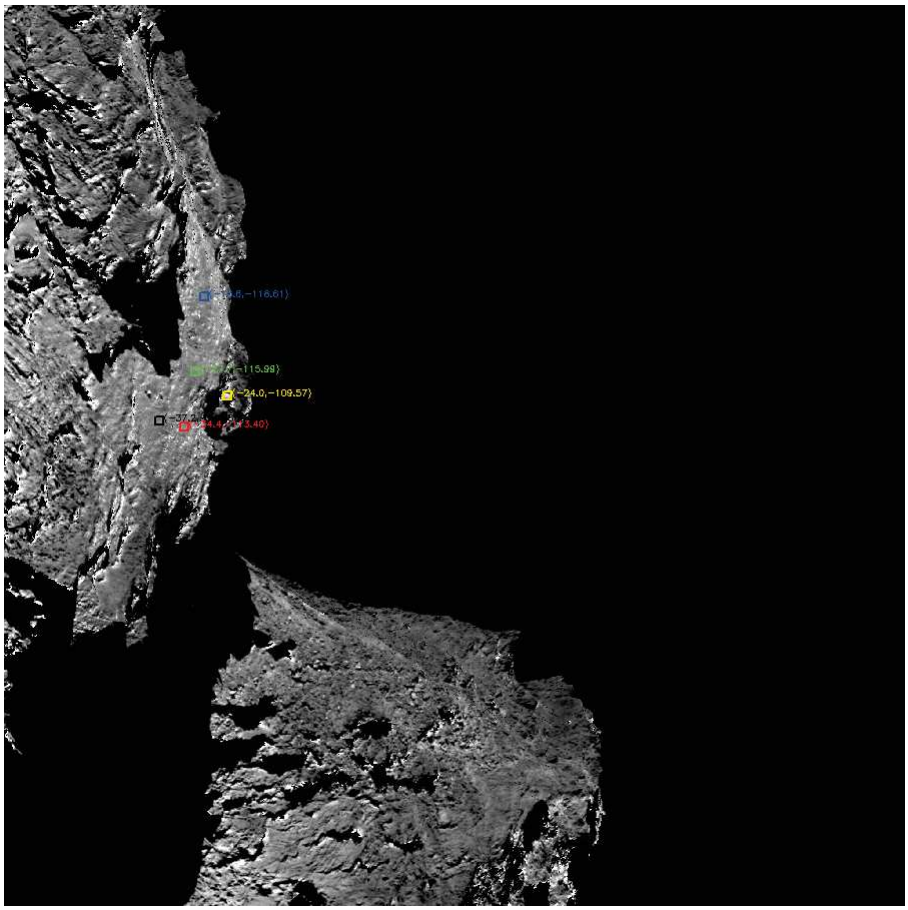

Figure 3.11: The reference image (F28) for dataset 3 and selection of five boxes of 8 × 8 pixel on the Anubis region and on the boulder (yellow box) between the Anubis and Seth region.

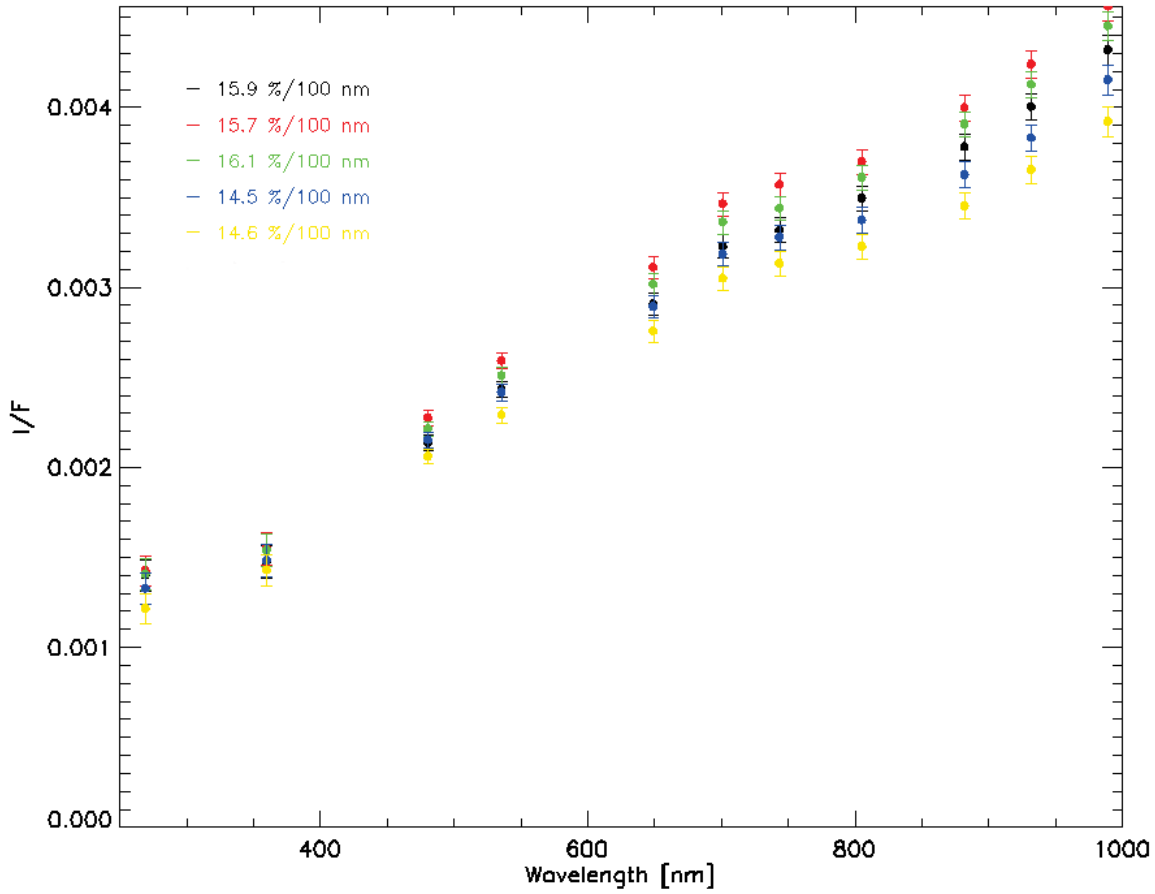

Figure 3.12: Absolute low resolution spectra of the Anubis region from dataset 1. The reflectance values are corrected with the Akimov disk function and plotted with the associated error bars. The legend shows the spectral slope values for each selected box.

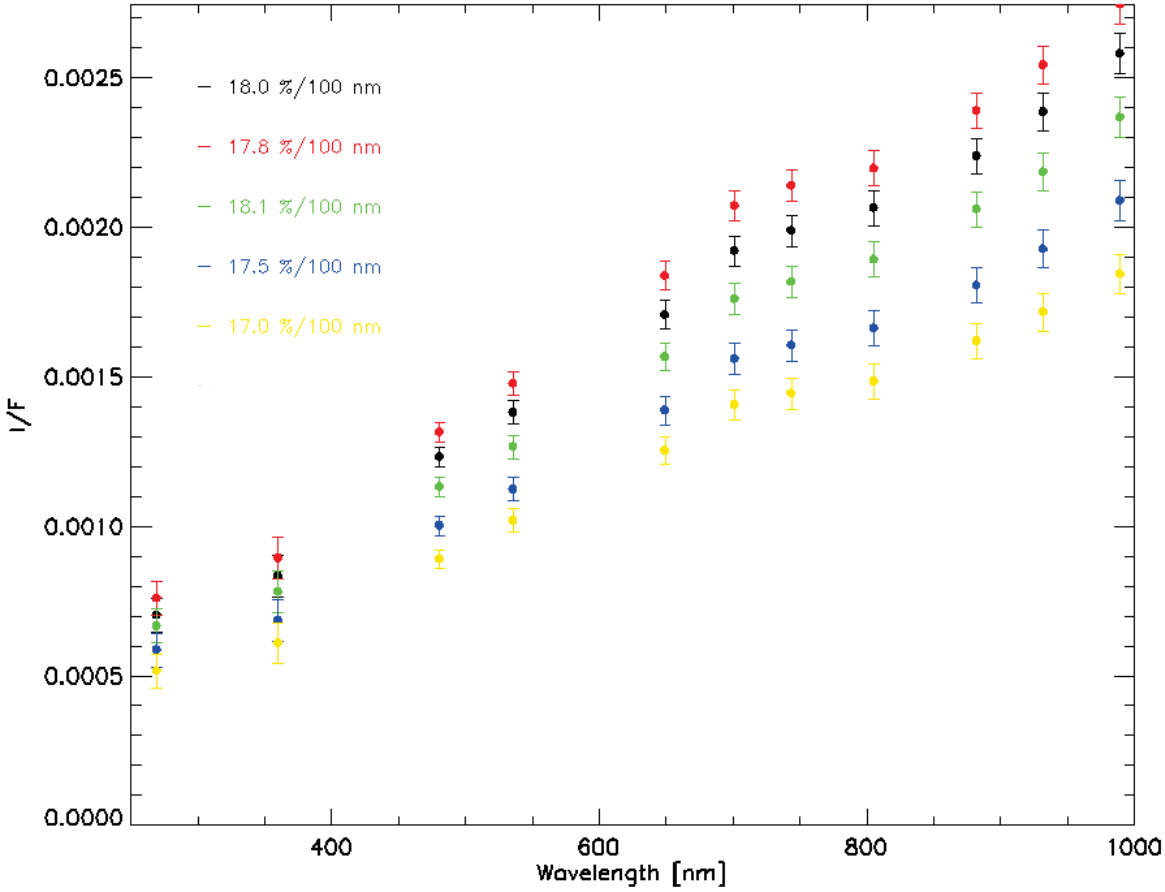

Figure 3.13: Absolute low resolution spectra of the Anubis region from dataset 2. The reflectance values are corrected with the Akimov disk function and plotted with the associated error bars. The legend shows th spectral slope values for each selected box.

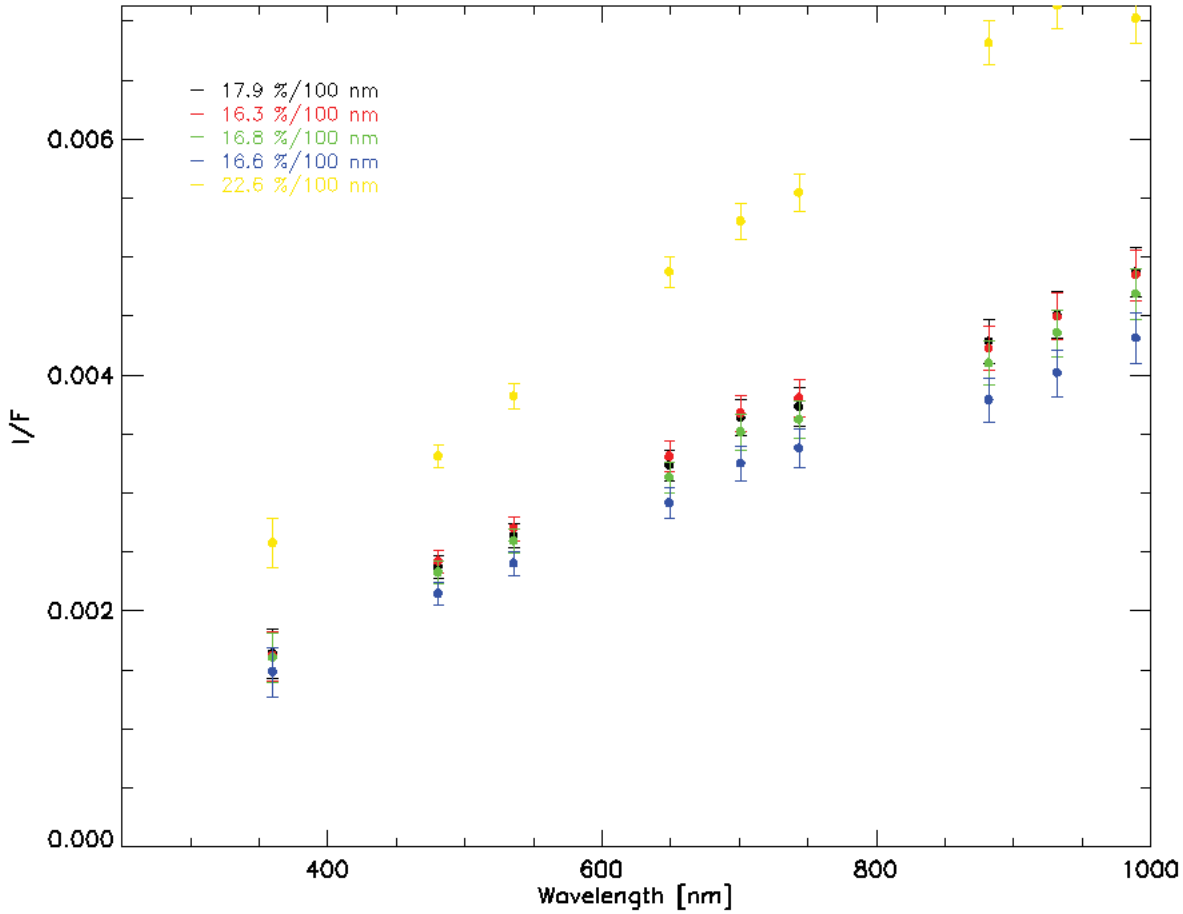

Figure 3.14: Absolute low resolution spectra of the Anubis terrain and of the boulder with a bright feature located between the Anubis and Seth region for dataset 3. The reflectance values are corrected with the Akimov disk function and plotted with the associated error bars. Nine filters were available for this dataset. The legend shows spectral slope values for each selected box.

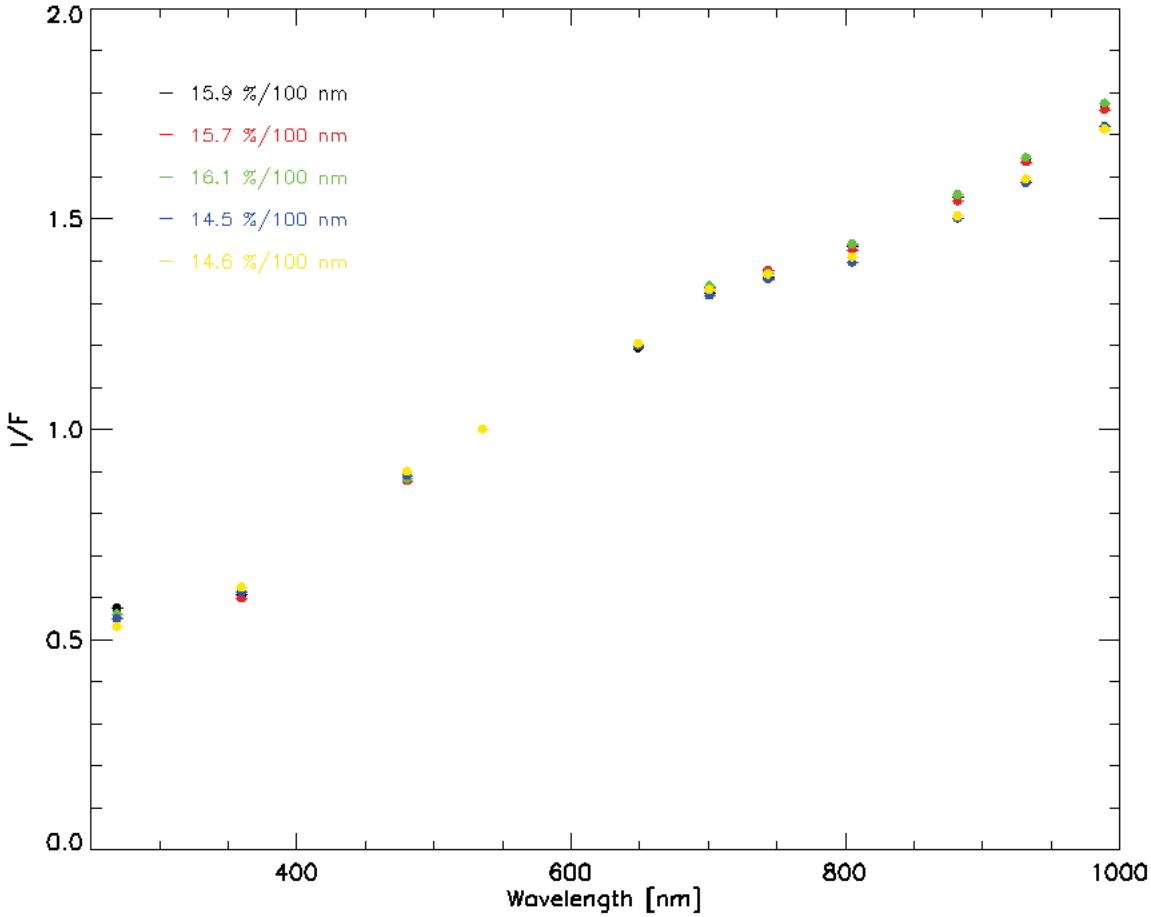

Figure 3.15: Low resolution spectra normalized at 535.7 nm (green filter) from dataset 1. Error bars are inside the symbol dimension.

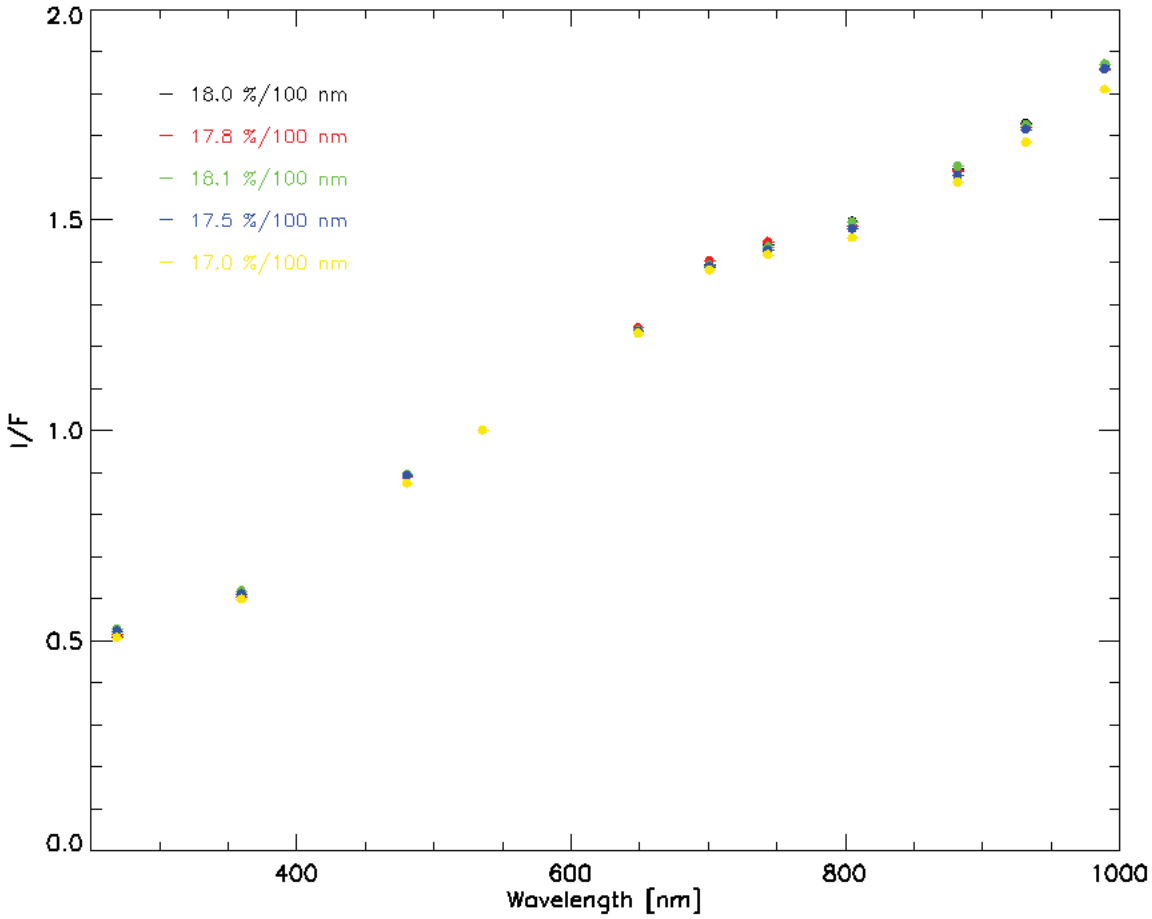

Figure 3.16: Low resolution spectra normalized at 535.7 nm (green filter) from dataset 2. Error bars are inside the symbol dimension.

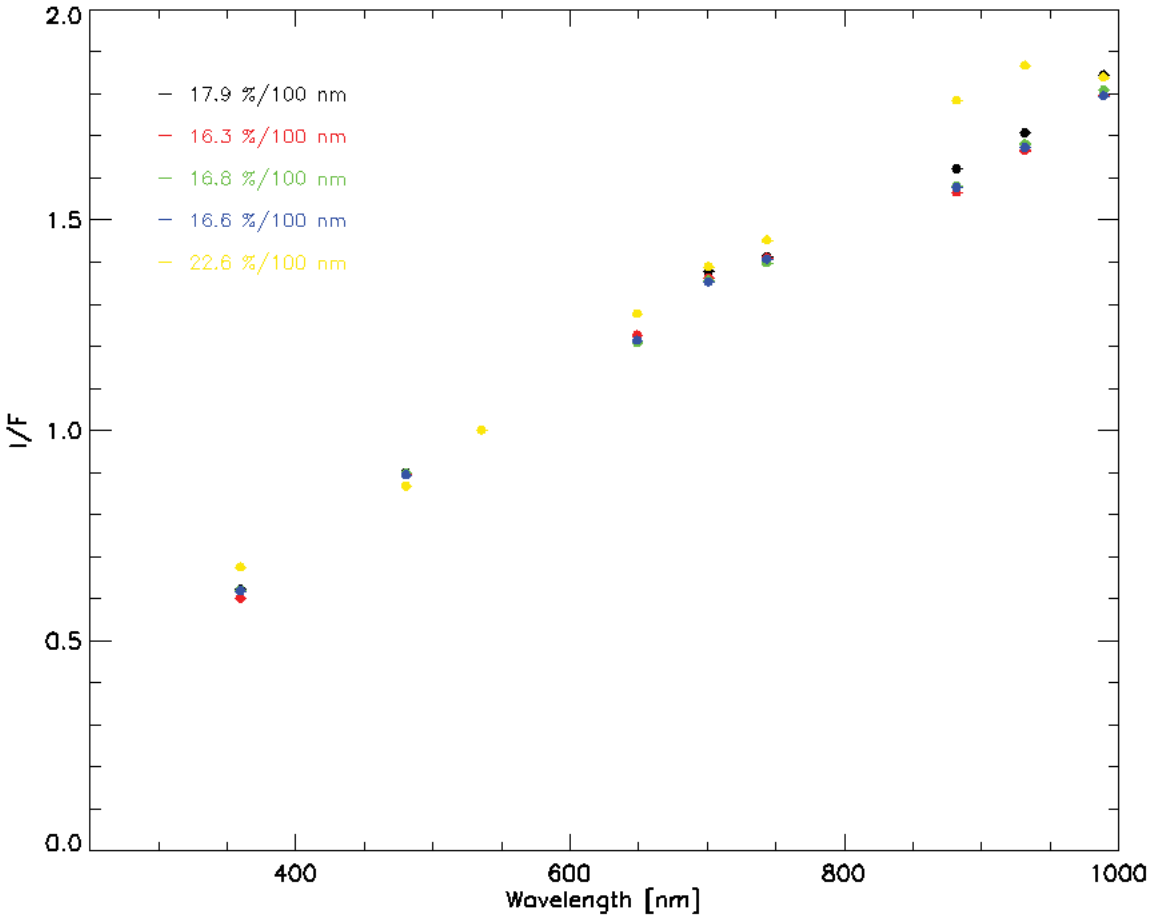

Figure 3.17: Low resolution spectra normalized at 535.7 nm (green filter) from dataset 3. Nine filters were available for this dataset. Error bars are inside the symbol dimension.

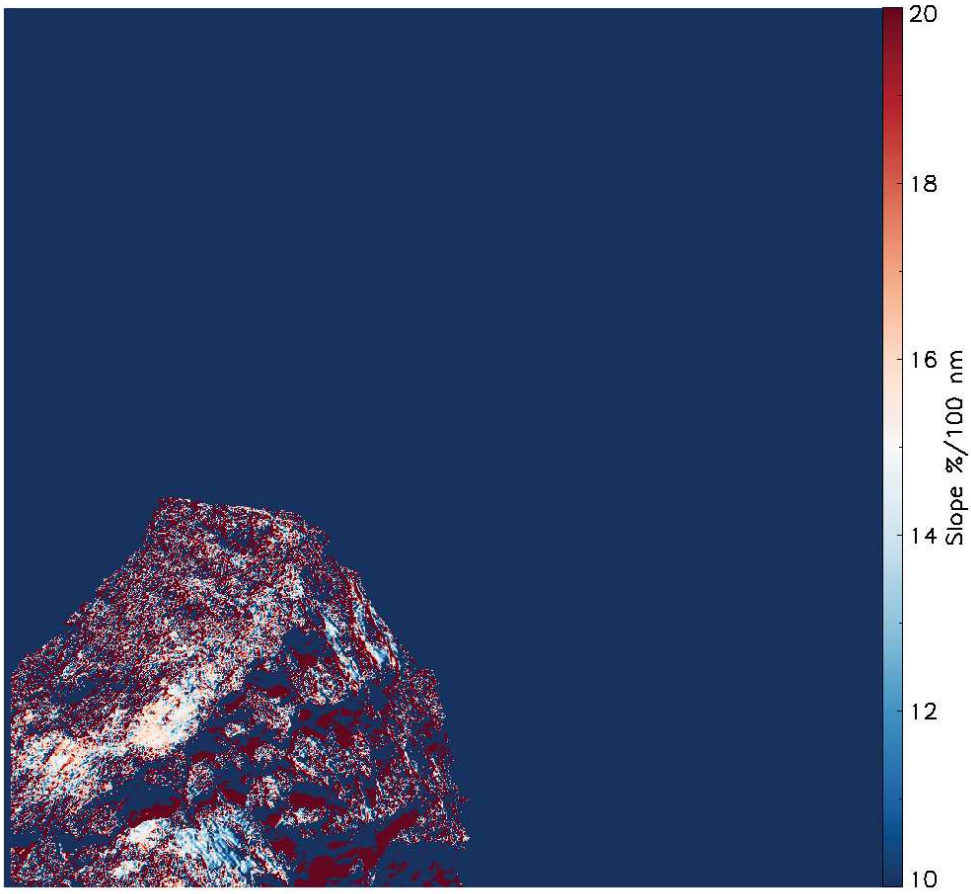

Figure 3.18: Spectral slope map of the comet, obtained with near-IR and green filters for dataset 1. The color bar displays in blue areas with a spectral slope lower than the average, in red slope values higher than the average.

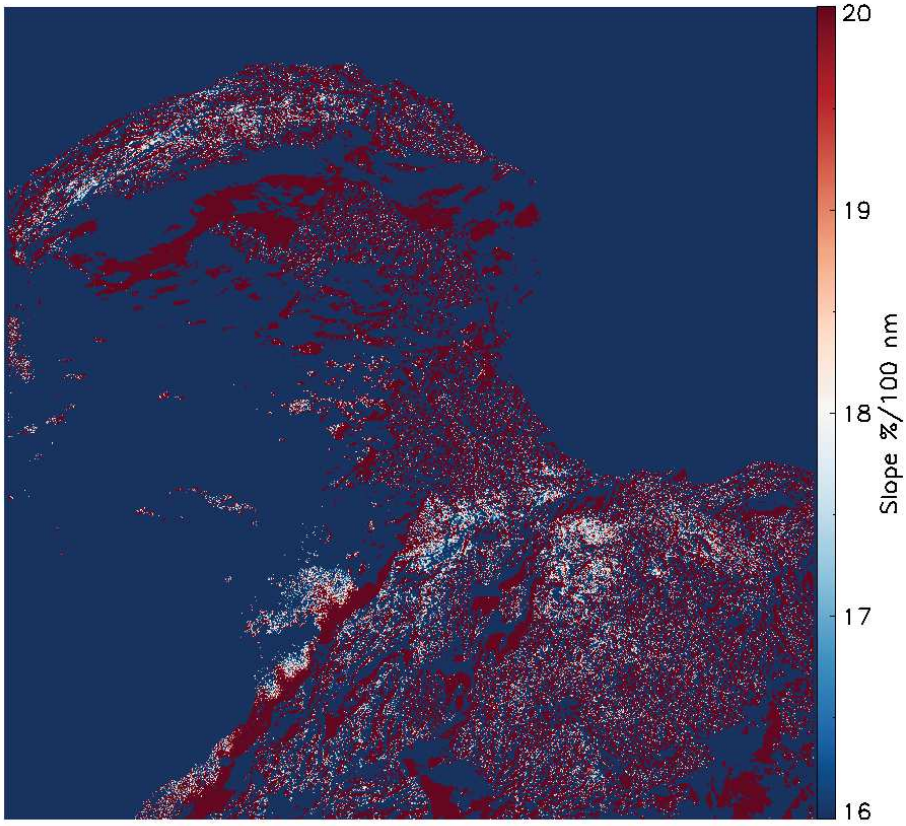

Figure 3.19: Spectral slope map of the comet, obtained with near-IR and green filters for dataset 2. The color bar displays in blue areas with a spectral slope lower than the average, in red slope values higher than the average.

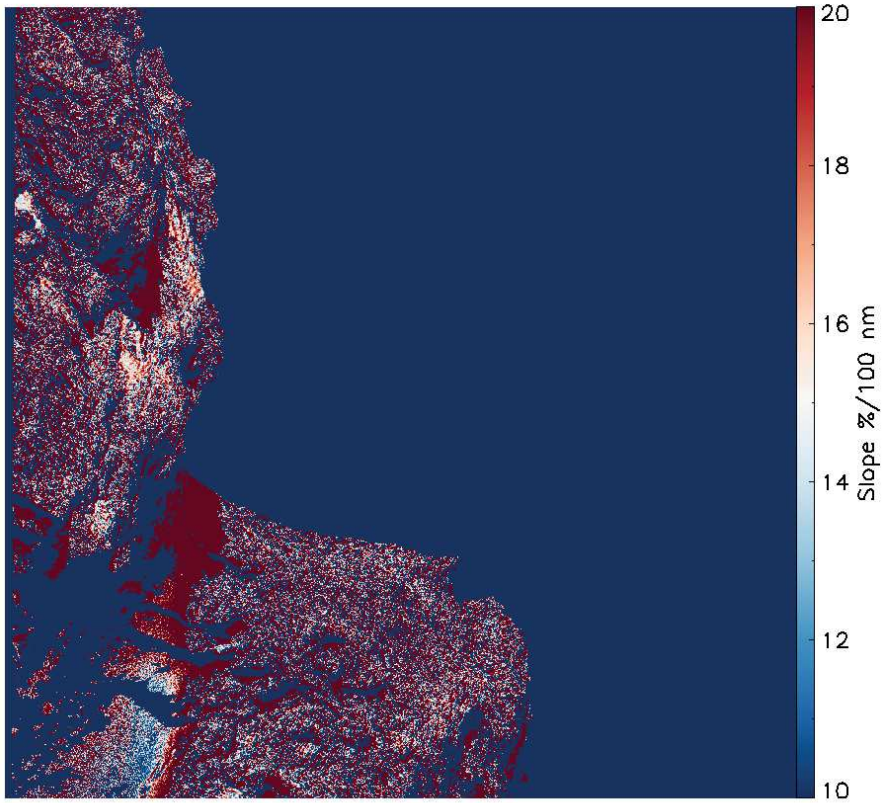

Figure 3.20: Spectral slope map of the comet, obtained with near-IR and green filters for dataset 3. The color bar displays in blue areas with a spectral slope lower than the average, in red slope values higher than the average.

3.6 Estimate of the uncertainties

As seen above, spectra of each dataset display the reflectance values as a function of the wavelength and the error bars associated to the reflectance values have been plotted for each filter. Indeed, according to eq. 3.8 the reflectance is affected by the uncertainties in each filter and by the errors due to the Akimov disk function D, used for the topographic correction. Thus, according to the theory of the propagation of uncertainties, the uncertainty on the I/F_{corr} values plotted in the spectra is:

$$d(I/F_{cor,\lambda}) = \sqrt{\left(\frac{\partial(I/F_{cor,\lambda})}{\partial(I/F_{meas,\lambda})} d(I/F_{meas,\lambda})\right)^2 + \left(\frac{\partial(I/F_{cor,\lambda})}{\partial D} dD\right)^2} \tag{3.10}$$

In order to estimate the errors linked to the measured reflectance ($I/F_{meas,\lambda}$), we considered relative errors associated to the NAC filters, which have been described by Tubiana et al. 2015b. In particular, the photometric accuracy expressed in terms of

the uncertainty of I/F, has different contributions. These contributions are related to: the aperture photometry of the standard star images, the spectrum of the star and of the Sun taken as reference, the uncertainty on the central wavelength of each filter, particularly critical for the UV region, the contribution of pinholes in some filters and stray light rays for different observing geometries. Thus, taking into account all these contributions the relative uncertainty associated to the NAC UV filters is $\sim$ 4-6%, while the visible and near-IR filters have a much higher accuracy $\sim$ 1-1.7%, thanks to cross-camera calibration and observations of Vesta performed before Rosetta entered hibernation (Tubiana et al. 2015b). Considering these estimates, in this work it has been assumed an error of 5% for the UV filters and an error of 1.5% for the filters in the visible and near-infrared range.
For the theory of the propagation of uncertainties, in eq. 3.10 it must be used the absolute value of the errors, thus the relative errors above have been converted to absolute errors by multiplying for the mean value of the measured reflectance in each filter:

$$d(I/F_\lambda) = \left(\frac{d(I/F_{\lambda,rel})}{100} I/F_{\lambda,mean} \right) \tag{3.11}$$

The mean value of the measured reflectance has been evaluated, image by image, considering the I/F_{meas} values at the latitude and longitude coordinates of the selected boxes for each cube. Between these selected values of I/F_{meas}, it has been computed the average value $I/F_{\lambda,mean}$, which has been used for the estimate of the uncertainties. Hence, each image of the datasets has a different value of $I/F_{\lambda,mean}$ and of $d(I/F_\lambda)$. On dataset 3 it has been analysed the reflectance of a boulder with a bright patch on its surface. Thus, in addition to the reflectance values in the area of the selected boxes in the Anubis region, the reflectance on the boulder's surface has been considered to estimate the I/F_{mean} of each image.
Concerning the uncertainties on the map of the disk function D(α, i, e), it must be considered eq. 3.5, where it is clear the dependence of the Akimov disk function on the angles e, i and α. As seen above, D(α, i, e) has been computed considering the values of the emission, incidence and phase angles of the reference image, therefore it assumes a different value for each cube. The propagation of uncertainties formula for D(α, i, e, λ) is:

$$dD = \sqrt{\left(\frac{\partial D}{\partial \alpha} d\alpha \right)^2 + \left(\frac{\partial D}{\partial \beta} d\beta \right)^2 + \left(\frac{\partial D}{\partial \gamma} d\gamma \right)^2} \tag{3.12}$$

In order to apply this equation we considered the value of the angles e, i and α in which to compute the partial derivatives of eq. 3.12, that are different for each cube. Thus, considering the map of the emission and incidence angles of the reference image, the mean value assumed from the angles, in the area around the latitude and longitude coordinates of the boxes selected, has been evaluated. For the phase angle, which shows low variations among the cube it has been considered the mean value of α on the surface of the comet.
Then, it has been computed the value of the absolute errors associated to the emission,

incidence and phase angles. Uncertainties on the angles have been estimated using the spatial resolution of the comet's shape model, that can be retrieved as the minimum difference in angles e, i, and α within each map. Specifically, among the maps of the illumination angles it has been evaluated the minimum difference assumed from the angles values between adjacent pixels, in correspondence of the latitude and longitude coordinates at which boxes have been selected to obtain the spectra. This estimate of the uncertainties associated to the angles allows to trace the resolution of the comet's shape model, which indeed has been implemented using the maps of the illumination angles. The estimated absolute errors are: de = 0.0002°, di = 0.1°, dα = 0.0006° for all the datasets.
Finally, the partial derivatives of D respect to α, β and γ have been computed, taking into account that β and γ depends on e, i and α, as follows:

$$\beta = \arccos\left[\frac{\cos e}{\cos\left(\arctan\left(\frac{\cos i}{\cos e \sin\alpha} - \cot\alpha\right)\right)}\right] \tag{3.13}$$

$$\gamma = \arctan\left(\frac{\cos i}{\cos e \sin\alpha} - \cot\alpha\right) \tag{3.14}$$

which comes from eq. 3.6 and 3.7. The absolute errors of β and γ, which appear in eq. 3.12, have been computed from the errors in i, e and α using the formula for the propagation of uncertainties, as follows:

$$d\beta = \sqrt{\left(\frac{\partial\beta}{\partial e}de\right)^2 + \left(\frac{\partial\beta}{\partial i}di\right)^2 + \left(\frac{\partial\beta}{\partial\alpha}d\alpha\right)^2} \tag{3.15}$$

$$d\gamma = \sqrt{\left(\frac{\partial\gamma}{\partial e}de\right)^2 + \left(\frac{\partial\gamma}{\partial i}di\right)^2 + \left(\frac{\partial\gamma}{\partial\alpha}d\alpha\right)^2} \tag{3.16}$$

Therefore, considering the contribution to the errors due to the measured reflectance for each filter and to the Akimov disk function, the errors associated to the reflectance corrected for the topography effects (eq. 3.5) in each filter are reported in Tab. 3.5.
Finally, starting from equation 3.9, the uncertainty on the spectral slope value has been computed for each cube. As in the previous cases, the propagation of uncertainties formula for the slope has been used:

$$dS = \sqrt{\left(\frac{\partial S}{\partial(I/F_{NIR})}d(I/F_{NIR})\right)^2 + \left(\frac{\partial S}{\partial(I/F_{Green})}d(I/F_{Green})\right)^2} \tag{3.17}$$

where d(I/F$_{NIR}$) and d(I/F$_{Green}$) are the absolute errors associated to the reflectance value of the near-infrared and green NAC filters, which appear in the slope formula. d(I/F$_{NIR}$) and d(I/F$_{Green}$) have been calculated from the relative errors listed in the OSIRIS calibration pipeline, as described above for a generic value of λ (eq. 3.11).

Filter	d(I/F$_{cor,\lambda}$) dataset 1	d(I/F$_{cor,\lambda}$) dataset 2	d(I/F$_{cor,\lambda}$) dataset 3
15	$8.44392 \cdot 10^{-5}$	$5.66875 \cdot 10^{-5}$	/
16	$8.95919 \cdot 10^{-5}$	$6.91120 \cdot 10^{-5}$	$2.0766 \cdot 10^{-4}$
24	$4.17209 \cdot 10^{-5}$	$3.21892 \cdot 10^{-5}$	$9.67184 \cdot 10^{-5}$
23	$4.50065 \cdot 10^{-5}$	$3.92674 \cdot 10^{-5}$	$1.0360 \cdot 10^{-4}$
22	$5.94907 \cdot 10^{-5}$	$4.75013 \cdot 10^{-5}$	$1.3055 \cdot 10^{-4}$
27	$6.54264 \cdot 10^{-5}$	$5.04927 \cdot 10^{-5}$	$1.5151 \cdot 10^{-4}$
28	$6.75320 \cdot 10^{-5}$	$5.25997 \cdot 10^{-5}$	$1.6169 \cdot 10^{-4}$
51	$6.98778 \cdot 10^{-5}$	$5.85340 \cdot 10^{-5}$	/
41	$7.06556 \cdot 10^{-5}$	$5.92592 \cdot 10^{-5}$	$1.8744 \cdot 10^{-4}$
61	$7.44786 \cdot 10^{-5}$	$6.32287 \cdot 10^{-5}$	$1.9762 \cdot 10^{-4}$
71	$8.21746 \cdot 10^{-5}$	$6.67528 \cdot 10^{-5}$	$2.1349 \cdot 10^{-4}$

Table 3.5: Estimate of the errors for the corrected reflectance (d(I/F$_{cor}$)) for each dataset.

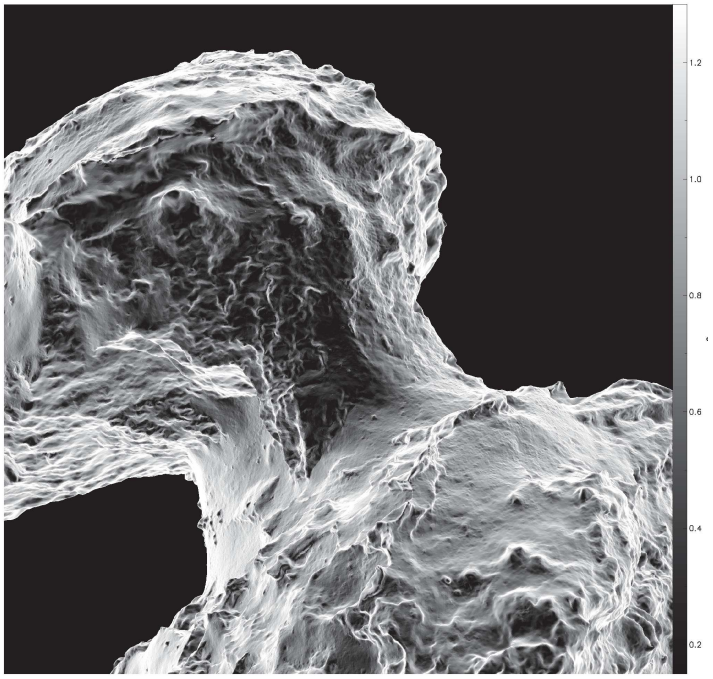

Figure 3.21: Map of the emission angle for dataset 2.

The partial derivative of the slope S respect to the measured reflectance in the F23 and F41 filters has been evaluated computing the mean value of the reflectance at the latitude and longitude coordinates of the boxes selected for the spectra. Indeed, these values are different for each filter and change over the surface of the comet, in this case they have been evaluated for the near-infrared and green filters, according to the spectral slope formula. Thus, the errors associated to the spectral slope value for the dataset 1 and 2 are 0.9 %/100 nm, and for dataset 3 is 1 %/100 nm, as reported in Tab. 3.4.

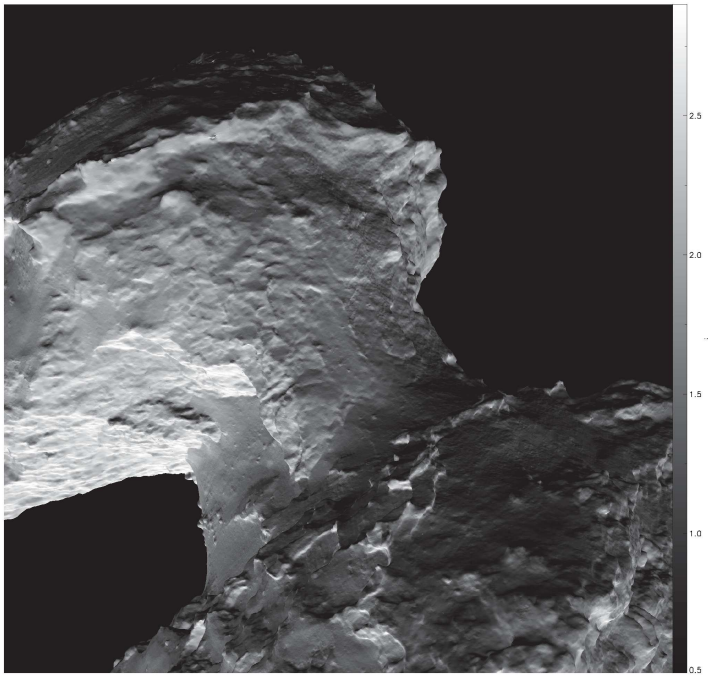

Figure 3.22: Map of the incidence angle for dataset 2.

Figure 3.23: Map of the phase angle for dataset 2.

Chapter 4

Discussion of the spectrophotometric results

This study fits into the spectrophotometric research performed on comet 67P/Churyumov-Gerasimenko, by use of images acquired with the NAC camera of the OSIRIS instrument on-board Rosetta spacecraft. The aim of this study is to analyse the spectral behaviour of the Anubis region, located on the body lobe. Indeed, many regions have already been spectrophotometrically examined, we focused our analysis to the physiographic regions which still lack of this kind of investigation. Anubis has been chosen among ten regions (Aker, Apis, Aten, Babi, Geb, Anuket, Hathor, Neith and Sobek), and has been investigated using images pre and post perihelion. In particular we aim to highlight any possible variation on the surface of Anubis and to investigate the possible correlation with illumination conditions, stagionality and evolution.
Our analysis has been performed on three datasets of images acquired with the OSIRIS/NAC camera. Dataset 1 was acquired on 22-05-2015, almost three months before perihelion passage (13 August 2015), dataset 2 was acquired on 9-01-2016, five months after perihelion and dataset 3 was acquired on 28-01-2016. The first two datasets have been acquired with eleven broad band filters, while for the third dataset images in nine filters were available. In order to perform an accurate spectrophotometric study, images have been transformed to reflectance, co-registered, corrected for photometric and topographic effects and sorted by increasing values of the wavelength in a multispectral cube.
The Anubis region has been classified, together with Imhotep and Aten, as a large irregular depression (Giacomini et al. 2016). From the geological map of the comet (Fig. 4.1), it is clear that Anubis is mainly composed of four geological units: smooth terrain, smooth terrain with boulders and to a less extent, outcropping consolidated terrain and fine particle deposits on consolidated terrain (Giacomini et al. 2016). The boulders which characterize part of the Anubis terrain could have been released from the Seth or Atum close regions, as a consequence of past activity (El-Maarry et al. 2015).

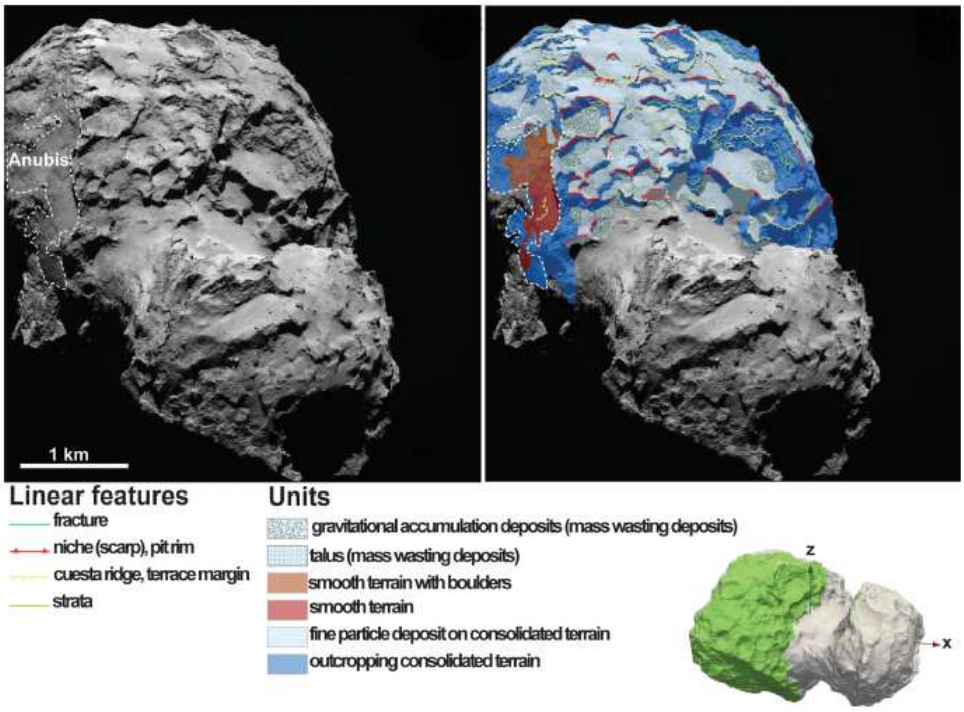

Figure 4.1: Partial geologic mapping of comet, the Anubis region is bordered with white dashed line (Giacomini et al. 2016).

4.0.1 Surface variegation in Anubis region

By comparing our datasets with the geologic mapping of the Anubis region (Fig. 4.2) it follows that the red and green boxes are located on smooth terrain, the blue box is between smooth terrain and smooth terrain with boulders, while the black one is located on the outcropping consolidated terrain and the yellow one on consolidated terrain covered with fine particle deposits. It must be noted that the location of each box in datasets 1 coincides with the location of the box of the same colour in dataset 2 since they have been selected to be at about the same latitude and longitude on the nucleus surface despite the changing illumination and observation conditions. Considering the spectra of datasets 1 and 2 (Fig. 3.12, 3.13), it results that the yellow box shows the lowest reflectance for both datasets, as well as displays the bluest spectral slope with respect to the other boxes. This could be linked to the difference in the grain shape and dimension between fine particle deposits on consolidated regions and smooth terrain. Concerning all the other boxes, it can be observed a slight variability in the reflectance and slope values.
The slight variability observed among the reflectance values of datasets 1 and 2 mentioned above, could be ascribed to the different geologic units where boxes have been selected. In particular smooth terrains (red, green and blue box) show the highest reflectance, fine particle deposits (yellow box) the lowest and consolidated terrain (black box) fits between these two values. This dependence of the reflectance values on the geologic units is in accordance with what found by Deshapriya et al. 2016 in the spectrophotometric analyisis of the Khonsu region.

Overall, low-resolution spectra for the three datasets display a linear trend of the reflectance with increasing values of the wavelength, without any specific absorption feature. This is in agreement with the global spectral trend of the nucleus before perihelion (Fornasier et al. 2015), and with the local results obtained, for example, in the Khonsu and Seth regions before and after perihelion (Deshapriya et al. 2016, Lucchetti et al. 2017), in the Imhotep region after perihelion (Feller et al. 2018) and at the landing site of the Philae lander, Agilkia, before perihelion (La Forgia et al. 2015). A slight deflection in the linear trend of the spectrum appears around 805 nm. This behaviour could be interpreted as related to the coma emission detected in the 700-743 nm range, which generates the subsequently deflection at 805 nm. This feature is consistent with the results found globally on comet 67P by Fornasier et al. (2015).
Spectra normalized at 535.7 nm (Fig. 3.15, 3.16, 3.17) confirm that overall the region is homogeneous and the variegation is small.

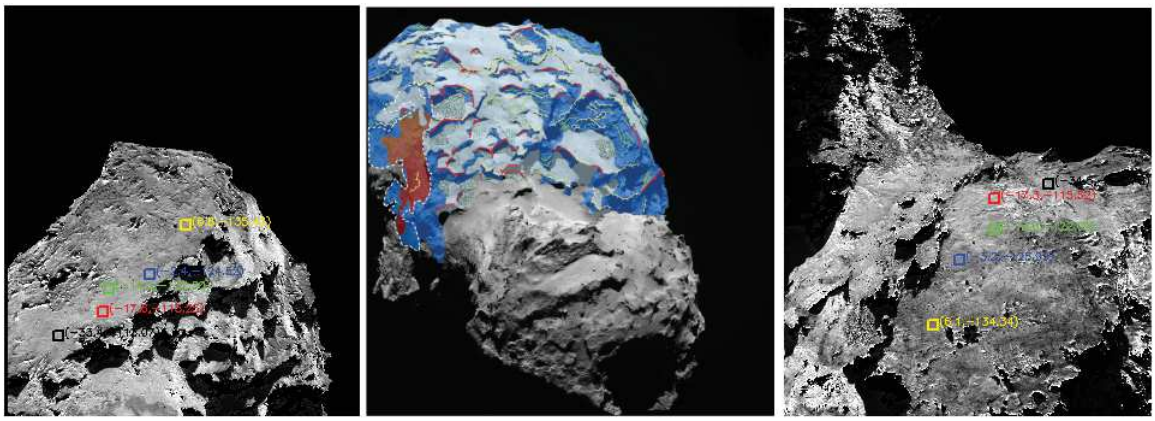

Figure 4.2: Overview of the boxes selected, with the same latitude and longitude coordinates, on different geologic units for datasets 1 and 2.

For dataset 1 the spectral slope values range between $14.5 \pm 0.9\,\%/100\,\mathrm{nm}$ and $16.1 \pm 0.9\,\%/100\,\mathrm{nm}$ on the selected boxes, for dataset 2 between $17 \pm 0.9\,\%/100\,\mathrm{nm}$ and $18.1 \pm 0.9\,\%/100\,\mathrm{nm}$, and for dataset 3 between $16.3 \pm 1\,\%/100\,\mathrm{nm}$ and 17.9 ± 1 %/100 nm. Overall, the spectral slope of the terrain ranges between 15 and 18 %/100 nm, which leads us to classify Anubis as an average spectral slope terrain, according to the classification made by Fornasier et al. 2015. As an example, the Imhotep and Khonsu regions belong to the same group.
The reflectance values before perihelion (dataset 1) range from from 0.12% in the UV up to 0.46% in the near-IR. At the beginning of January (dataset 2) refelctance is very low, of about 0.06% in the UV wavelength to 0.24% in the near-IR wavelength, finally for dataset 3 it ranges from 0.15 to 0.45%.
The mean values of the reflectance in the green filter and the mean slopes for each dataset are shown in Tab. 4.1, together with date and phase angles at which different datasets have been acquired.

Dataset	Date	$\alpha[^\circ]$	$(I/F)_{mean,Green}$	$S_{mean}[\%/100nm]$
1	2015-05-22	61	0.00245	15.4
2	2016-01-9	90	0.00125	17.7
3	2016-01-28	62	0.00258	16.9
			0.00283 (with boulder)	18.0 (with boulder)

Table 4.1: The main characteristics and results for the datasets used in this study: the acquisition date, the phase angle α, the mean reflectance for the green filter and the mean spectral slope.

4.0.2 Comparison of datasets

From the comparison of spectra in Fig. 3.12 and 3.13, it follows that the small variegation observed within the Anubis region remained somehow consistent before and after perihelion, indeed the yellow box remains the one with the lower reflectance, and the red box keeps the highest reflectance. The black box is the only one who has changed its relative reflectance as compared to the surrounding data (Fig. 3.12 and 3.13), as it was below the green box before perihelion and above it after perihelion. Comparing the spectral slope values before and after perihelion, we can notice that on average also the spectral slope variability within the sample has preserved its behaviour after perihelion, in particular the green box keeps the highest spectral slope, followed by the black and the red boxes respectively. The lowest spectral slope is achieved by the yellow box post-perihelion, while before perihelion the blue and yellow boxes share the lowest values 14.5 and 14.6 %/100 nm respectively. However, these subtle variations are consistent within the different conditions of observation between the datasets. Overall, the average red spectral behaviour of the Anubis terrain has been maintained after perihelion. This result could be interpreted as due to the overall small size of the region, which makes plausible that the whole part is uniformly modified by the cometary activity at perihelion. In particular it might suggest a uniform dust fall-out subsequent to the perihelion activity, which does not modify the local variegation of different geologic units.

4.0.3 Phase reddening effects

Datasets 2 and 3 have been acquired post-perihelion in January 2016, on 9 and 28 respectively. Since datasets 2 and 3 refer to the same period, no seasonal or evolutional effect is expected. However, as shown in Tab. 4.1, datasets 2 and 3 have been acquired at α= 90° and α=62° respectively. Therefore, we compared the two datasets (except for the yellow box on dataset 3 which is located on the bright boulder) in order to investigate pure phase reddening effects. The mean spectral slope values are 16.9 %/100 nm for dataset 3 and 17.7 %/100 nm for dataset 2, thus on average dataset 2 shows an enhancement of the spectral slope of $\sim$ 0.8 %/100 nm. This change in spectral

slope is attributed to a phase reddening effect, which causes an increase in the spectral slope passing from a smaller (62°) to a larger phase angle value (90°). We estimated the phase reddening effect considering the linear fit of the slope as a function of the phase angle. Thus the phase reddening ΔS has been computed as the ratio of the angular coefficient and the intercept of the linear fit. The slope value considered for each cube is the mean value of the slope of the four boxes. We obtained a phase reddening of 0.18 %/°, which can be compared with what found by Fornasier et al. 2015 and Ciarniello et al. 2015. Indeed for the global nucleus of the comet in the visible range a phase reddening of 0.95 %/° was found for 1° $<\alpha<$ 54° (Fornasier et al. 2015). While using the VIRTIS instrument Ciarniello et al. 2015 measured a phase reddening of 0.44 %/° for 20 ° $<\alpha<$ 120 ° in the visible range. The higher value found by Fornasier et al. 2015 could be ascribed to a different phase angle coverage, from 1 to 54° where the phase curve is much steeper and the phase angle effects are therefore more pronounced. The higher value found by Ciarniello et al. 2015 with respect to our value is to be ascribed similarly to a much larger phase angle coverage and possibly to the slightly different wavelength range used (550-800 nm). Additionally it is important to note that both measurements were performed pre-perihelion and as an average on the global nucleus. Despite the differences in the phase angle coverage our measurement suggests that the terrains characterizing Anubis region displays a smaller phase reddening effect in the post-perihelion epoch with respect to the global nucleus in the pre-perihelion epoch. This might hints to a different role of multiple scattering in the post-perihelion epoch. Further studies will be necessary to test this theory.

4.0.4 Seasonal evolution

Datasets 1 and 3 have been acquired respectively on May 2015 and January 2016, that is pre and post-perihelion, but they share about the same phase angle, 61° and 62° respectively. Thus, phase reddening effect do not pertain here, and the comparison between the two dataset will yield pure seasonal evolution. We recall that for dataset 3 boxes have been selected on different coordinate positions with respect to dataset 1, because a portion of the Anubis region is not visible in dataset 3, due to the observational conditions relative to the comet-spacecraft positions. However, all the boxes in dataset 3 have been selected on the smooth or consolidated terrain of the region (except for the yellow box which we neglect now) thus it is possible to compare them. It follows that the mean spectral slope is 15.4 %/100 nm for dataset 1 and 16.9 %/100 nm for dataset 3. This means that the spectral slope has increased of 1.5%/100 nm. This effect can be ascribed exclusively to seasonal evolution of the Anubis surface due to perihelion passage. The 1.5%/100 nm increase of the slope value is consistent with observed variations in the nucleus, which was observed to be redder when the comet is at large heliocentric distance, while approaching perihelion the slope decrease becoming bluer (Fornasier et al. 2015). In our case dataset 1 has been acquired three months before the perihelion passage, displaying a bluer spectral slope as compared to dataset 3. This trend could be linked to the different acquisition periods of both datasets, three months before and five after perihelion, which correspond to different phases of cometary activity. Indeed, at perihelion comet is subjected to a stronger

solar irradiation which leads to the sublimation of volatile components and removal of dust particles. As a consequence of the increasing activity the internal layers are exposed, revealing a bluer spectral colour (Fornasier et al. 2016). On the other hand, the spectral slope of dataset 3 is higher and corresponds to a redder colour. This could reveal that the comet activity has gradually decreased and it will continue to reduce as it approaches the outer solar system along its orbit. At such distances the bluening effect of the perihelion have been already washed out by the redeposition of volatile-poor refractory dust particles which make the spectra red again.
We also computed the mean reflectance value in the green filter for the four boxes, obtaining very similar values, 0.245% for dataset 1 and 0.258% for dataset 3, suggesting that while the colours of the terrain show a significant seasonal evolution, the average reflectance of the terrain remains somehow constant over time showing much more variations depending on the geometric conditions rather than on seasonal evolution.

Comparing dataset 1 and 2 is complex as datasets have been acquired both at different phase angles (61° and 90° respectively) and at different epochs. Thus, the slope and reflectance change must take into account for both the phase reddening and evolutionary effects. The mean spectral slope increases from 15.4 to 17.7 %/100 nm, that is of 2.3 %/100 nm, while the mean reflectance value in the green filter consistently decreased of a 0.0012 factor. The increase in spectral slope can be interpreted in light of the results of the previous two comparisons as due for one third to the phase reddening effect and for the rest two thirds to the seasonal evolution. Therefore, the seasonal evolution influences the spectral slope more importantly than the phase reddening effect.
On average the Anubis region has become slightly brighter and redder compared to its pre-perihelion appearance. The redder behaviour could be attributed to a decrease in the volatile components upon sublimation at perihelion. Instead, the brighter reflectance could be ascribed to the exposure of slightly inner layers of the surface which display a higher reflectance, consistently with what was studied by Ferrari et al. 2018.

4.0.5 Spectral analysis of a bright feature at Anubis-Seth

Finally, we analysed the low-resolution spectra of the third dataset, which has been selected to inspect a bright boulder at the border of the Anubis and Seth region. Performing the analysis we aim to understand if the boulder displays a bright patch resting on its surface. Thus we selected a box of 8×8 pixel on the boulder's surface, which correspond to the yellow spectrum. The yellow box is indeed brighter if compared to the boxes selected on the rest of the Anubis terrain, showing a reflectance a factor 0.001 higher with respect to the mean reflectance of the Anubis terrain. The spectrum normalized at 535.7 nm (Fig. 3.17) displays the yellow box deviation from the global spectral trend at high wavelength values. However, also the spectral slope (22.6%/100 nm) of the boulder is higher than the mean spectral slope of the other boxes, being 16.9 %/100 nm. The red slope is associated to a composition of dark materials probably organic compounds with low abundances of volatile elements, leading

us to the conclusion that the boulder does not display a bright patch. Indeed, bright patches typically show a higher reflectance and a flat spectral slope with respect to the mean of the surrounding terrain. Their bluer spectral colour has been interpreted as due to the presence of a water ice component mixed with dust particles. In Fig. 4.3 the absolute and relative reflectance spectra of a bright feature identified on the Khonsu region are shown (Deshapriya et al. 2016). Therefore, the brighter appearance of the boulder could be due to the specific illumination condition of dataset 3 related to the boulder inclination on the surface. Indeed the boulder seems to be located on a sharp scarp between Seth and Anubis. In addition, we should consider that the topographic correction accounts for the shape model reconstruction of the comet which, despite the shape model has a resolution of 1-1.5 meters (Preusker et al. 2017) and the boulder has an estimated dimension of about 9.6 m^3, is less accurate on the surface of a boulder, whose contours are sharper and harder to model than the surrounding terrain. This could have affected the topographic correction, which was not able to completely correct the effects due to the illumination conditions on the boulder's surface. We investigated if the high spectral slope of the boulder could be caused by a large box dimension, which includes the surrounding terrain in the reflectance and slope calculation. However, the spectral slope value remains higher compared to the Anubis terrain even considering box dimensions of 6×6 or 4×4 pixels. The high red slope of the boulder could be interpreted with a less enrichment in volatile molecules and dust coverage, which the boulder could have lost moving from its original position. Indeed it is very likely that the boulder comes from the detachment of material from the close Seth region as a consequence of the Seth's activity. Thus, the boulder's surface appears covered by darker organic material with respect to the rest of Anubis terrain.

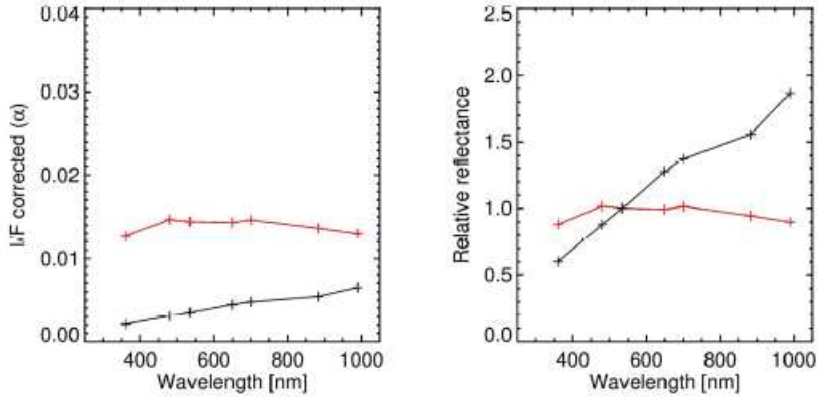

Figure 4.3: Absolute and relative reflectance spectra for a bright feature (in red) and the surrounding terrain (in black) on the Khonsu region (Deshapriya et al. 2016).

4.1 Conclusions and future development

To sum up our results, we studied the spectrophotometric properties of the Anubis physiographic region on the body lobe of comet 67P/Churyumov-Gerasimenko using

three datasets acquired with the OSIRIS/NAC camera onboard Rosetta respectively on 22-05-2015, 9-01-2016 and 28-01-2016. We defined five boxes of 16 pixels for the first two datasets and of 9 pixels for the third dataset. Boxes have been selected at different locations on the region, which following the geological map of Anubis region, produced by Giacomini et al. 2016 have been identified as smooth terrain, smooth terrain with boulders, outcropping consolidated terrains and fine particle deposits on consolidated terrain. We noticed that boxes display a slight variability in the reflectance and slope values. This variability remains consistent also after the perihelion passage, this could be attributed to a uniform dust coverage of the region as a consequence of the perihelion activity. The box selected on the fine particle deposits on outcropping consolidated terrain displays the lowest reflectance and slope, probably because of the difference in the grain shape and dimension between fine particle deposits and smooth terrain.
We analysed the spectral slope of each cube and compared the slope values of the three datasets. First, we have compared datasets 2 and 3, which have been acquired over a small period of time (in the month of January) and at different phase angle value, α= 62° and α=90°. We have found an increase in the spectral slope value of 0.8%/100 nm from dataset 3 to dataset 2, which could be attributed to the phase reddening effect, which correspond to ΔS=0.18 %/°. Comparing datasets 1 and 3, that is for similar phase angle values, but for different seasons we obtain an increase of 1.5 %/100 nm in the spectral slope, which could be attributed to the seasonal evolution which comet experiences as it approaches perihelion and then going outward. Finally to compare datasets 1 and 2, which have been acquired at different phase angles and different periods of time, we notice an increase in the slope of 2.3 %/100 nm, which is caused by both phase reddening and stagionality effects.

In order to make a proper comparison of the reflectance for datasets acquired at different phase angle, it is fundamental to take into account the contribution of the phase curve, apart from the seasonal effect. Indeed the reflectance depends on the phase angle showing a typical phase curve effect (Fig. 4.4). Therefore, in a future analysis it would be interesting to analyse the contribution of the phase curve in order to understand if the changes in the reflectance before and after perihelion are compatible with the nucleus average phase curve observed or they present additional variations due to the phase curve or to the seasonal effects. With this purpose it could be interesting to adopt the Hapke model to describe the reflectance of the Anubis surface in relation to the observation conditions and the physical properties of the terrain. Indeed, the Hapke model is a semi-empirical function which describes the measured reflectance of a particulate medium by use of five parameters, which depend in a complex way on the physical properties of the particulate medium that cover the surface as the composition, size, shape and opacity of the regolith grains. Thus, we could plot the values of the reflectance as a function of the phase angle found in our analysis, together with the phase curve of the global nucleus by Fornasier et al. 2015, in order to quantify the deviation of our data from that of the global nucleus. Therefore, it could be possible to identify the contribution due to the phase curve and subsequently the contribution of the phase reddening, and distinguish them from the seasonal effects.
Finally, it would be interesting to apply the spectrophotometric analysis to the regions

which still lack of this kind of investigation, in order to see if there are regions displaying a similar spectral behaviour and compare them with the regions already studied. This would provide a detailed and comprehensive view of the cometary surface changes and will help disentangling among observational, seasonal and evolutionary changes. Ultimately all the surface studies will help characterizing the nucleus intrinsic material and composition and the activity driving mechanisms working at shaping the comets in general.

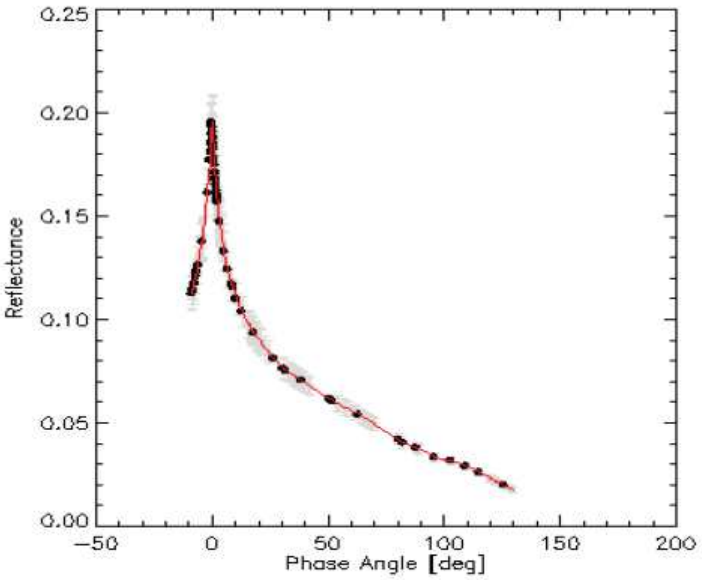

Figure 4.4: Phase curve showing the reflectance trend as a function of the phase angle.

Bibliography

[1] K. Altwegg et al. "67P/Churyumov-Gerasimenko, a Jupiter family comet with a high D/H ratio". In: *Science* 347 (Dec. 2014), p. 1261952. DOI: 10.1126/science.1261952.

[2] J. Bibring et al. "COMETARY SCIENCE. 67P/Churyumov-Gerasimenko surface properties as derived from CIVA panoramic images". In: *Science (New York, N.Y.)* 349 (July 2015). DOI: 10.1126/science.aab0671.

[3] Jens Biele et al. "COMETARY SCIENCE. The landing(s) of Philae and inferences about comet surface mechanical properties". In: *Science (New York, N.Y.)* 349 (July 2015). DOI: 10.1126/science.aaa9816.

[4] Nicolas Biver and Dominique Bockelee-Morvan. "Chemical diversity in the comet population". In: *Proceedings of the International Astronomical Union* 11 (Aug. 2015), pp. 228–232. DOI: 10.1017/S1743921316002945.

[5] Dominique Bockelee-Morvan et al. "Evolution of CO2, CH4, and OCS abundances relative to H2O in the coma of comet 67P around perihelion from Rosetta/VIRTIS-H observations". In: *Monthly Notices of the Royal Astronomical Society* 462 (Sept. 2016). DOI: 10.1093/mnras/stw2428.

[6] Fabrizio Capaccioni et al. "The organic-rich surface of comet 67P/Churyumov-Gerasimenko as seen by VIRTIS/Rosetta". In: *Science (New York, N.Y.)* 347 (Jan. 2015), aaa0628. DOI: 10.1126/science.aaa0628.

[7] Mauro Ciarniello et al. "Photometric properties of comet 67P/Churyumov-Gerasimenko from VIRTIS-M aboard Rosetta". In: *Astronomy Astrophysics* 583 (Sept. 2015). DOI: 10.1051/0004-6361/201526307.

[8] A Coradini et al. "The Surface Composition and Temperature of Asteroid 21 Lutetia As Observed by Rosetta/VIRTIS". In: *Science (New York, N.Y.)* 334 (Oct. 2011), pp. 492–4. DOI: 10.1126/science.1204062.

[9] Donald Davis and Paolo Farinella. "Collisional Effects in the Edgeworth-Kuiper Belt". In: 261 (Jan. 2001). DOI: 10.1007/978-94-010-0712-2_17.

[10] Prasanna Deshapriya et al. "Spectrophotometry of the Khonsu region on the comet 67P/Churyumov-Gerasimenko using OSIRIS instrument images". In: *Monthly Notices of the Royal Astronomical Society* 462 (Nov. 2016), S274–S286. DOI: 10.1093/mnras/stw2530.

[11] Paul Feldman et al. "Rosetta-Alice Observations of Exospheric Hydrogen and Oxygen on Mars". In: *Icarus* 214 (June 2011). DOI: 10.1016/j.icarus.2011.06.013.

[12] Clément Feller et al. "Rosetta/OSIRIS observations of 67P's nucleus during the April 2016 flyby: high-resolution spectrophotometry". In: *Astronomy Astrophysics* 630 (Dec. 2018). DOI: 10.1051/0004-6361/201833807.

[13] Sabrina Ferrari et al. "The big lobe of 67P/Churyumov-Gerasimenko comet: Morphological and spectrophotometric evidences of layering as from OSIRIS data". In: *Monthly Notices of the Royal Astronomical Society* 479 (Sept. 2018), pp. 1555–1568. DOI: 10.1093/mnras/sty1656.

[14] Sonia Fornasier, Clément Feller, et al. "The highly active Anhur-Bes regions in the 67P/Churyumov - Gerasimenko comet: results from OSIRIS/ROSETTA observations". In: *Monthly Notices of the Royal Astronomical Society* 469 (July 2017), S93–S107. DOI: 10.1093/mnras/stx1275.

[15] Sonia Fornasier, Pedro Henrique Hasselmann, et al. "Spectrophotometric properties of the nucleus of comet 67P/Churyumov-Gerasimenko from the OSIRIS instrument onboard the ROSETTA spacecraft". In: *Astronomy and Astrophysics* 583 (Nov. 2015), A30. DOI: 10.1051/0004-6361/201525901.

[16] Sonia Fornasier, V. Hoang, et al. *Linking surface morphology, composition, and activity on the nucleus of 67P/Churyumov-Gerasimenko*. Sept. 2018.

[17] Sonia Fornasier, S Mottola, et al. "Rosetta's comet 67P/Churyumov-Gerasimenko sheds its dusty mantle to reveal its icy nature". In: *Science (New York, N.Y.)* 354 (Dec. 2016), pp. 1566–1570. DOI: 10.1126/science.aag2671.

[18] Elisa Frattin et al. "Post-perihelion photometry of dust grains in the coma of 67P Churyumov–Gerasimenko". In: *Monthly Notices of the Royal Astronomical Society* 469 (June 2017), S195–S203. DOI: 10.1093/mnras/stx1395.

[19] Lorenza Giacomini et al. "Geologic mapping of the Comet 67P/Churyumov-Gerasimenko's Northern Hemisphere". In: *Monthly Notices of the Royal Astronomical Society* 462 (Nov. 2016), S352–S367. DOI: 10.1093/mnras/stw2848.

[20] Fred Goesmann et al. "Organic compounds on comet 67P/Churyumov-Gerasimenko revealed by COSAC mass spectrometry". In: *Science (New York, N.Y.)* 349 (July 2015). DOI: 10.1126/science.aab0689.

[21] Samuel Gulkis et al. "Cometary science. Subsurface properties and early activity of comet 67P/Churyumov-Gerasimenko". In: *Science (New York, N.Y.)* 347 (Jan. 2015), aaa0709. DOI: 10.1126/science.aaa0709.

[22] A. Herique et al. "Homogeneity of 67P/Churyumov-Gerasimenko as seen by CONSERT: implication on composition and formation". In: *Astronomy Astrophysics* 630 (May 2019). DOI: 10.1051/0004-6361/201834865.

[23] Karl Jansson and Anders Johansen. "Formation of pebble-pile planetesimals". In: *Astronomy Astrophysics* 570 (Aug. 2014). DOI: 10.1051/0004-6361/201424369.

[24] L. Jorda et al. "The Global Shape, Density and Rotation of Comet 67P/Churyumov-Gerasimenko from Pre–Perihelion Rosetta/OSIRIS Observations". In: *Icarus* 277 (May 2016). DOI: 10.1016/j.icarus.2016.05.002.

[25] H Keller et al. "E-type asteroid (2867) Steins as imaged by OSIRIS on board Rosetta". In: *Science (New York, N.Y.)* 327 (Jan. 2010), pp. 190–3. DOI: 10.1126/science.1179559.

[26] H. Keller et al. "Insolation, erosion, and morphology of comet 67P/Churyumov-Gerasimenko". In: *Astronomy Astrophysics* 583 (June 2015). DOI: 10.1051/0004-6361/201525964.

[27] Wlodek Kofman et al. "Properties of the 67P/Churyumov-Gerasimenko interior revealed by CONSERT radar". In: *Science* 349 (July 2015). DOI: 10.1126/science.aab0639.

[28] Fiorangela La Forgia et al. "Geomorphology and spectrophotometry of Philae's landing site on comet 67P/Churyumov-Gerasimenko". In: *Astronomy Astrophysics* 583 (Sept. 2015). DOI: 10.1051/0004-6361/201525983.

[29] L. Lara et al. "Large-scale dust jets in the coma of 67P/Churyumov-Gerasimenko as seen by the OSIRIS instrument onboard Rosetta". In: *Astronomy Astrophysics* 583 (Sept. 2015). DOI: 10.1051/0004-6361/201526103.

[30] Alice Lucchetti et al. "Geomorphological and spectrophotometric analysis of Seth's circular niches on comet 67P/Churyumov–Gerasimenko using OSIRIS images". In: *Monthly Notices of the Royal Astronomical Society* 469 (June 2017), S238–S251. DOI: 10.1093/mnras/stx1590.

[31] Mohamed Ramy El-Maarry, Nicolas Thomas, Lorenza Giacomini, et al. "Regional surface morphology of comet 67P/Churyumov-Gerasimenko from Rosetta/OSIRIS images". In: *Astronomy and Astrophysics* 583 (Nov. 2015), A26. DOI: 10.1051/0004-6361/201525723.

[32] Mohamed Ramy El-Maarry, Nicolas Thomas, A Gracia-Berná, et al. "Fractures on comet 67P/Churyumov-Gerasimenko observed by Rosetta/OSIRIS". In: *Geophysical Research Letters* 42 (July 2015), pp. 5170–5178. DOI: 10.1002/2015GL064500.

[33] M. Massironi et al. "The two independent and primitive envelopes of the bilobate nucleus of comet 67P/Churyumov-Gerasimenko". In: *Nature* 526 (Jan. 2015).

[34] S Mottola et al. "The structure of the regolith on 67P/Churyumov-Gerasimenko from ROLIS descent imaging". In: *Science (New York, N.Y.)* 349 (July 2015). DOI: 10.1126/science.aab0232.

[35] Laurence O'Rourke et al. "The Philae lander reveals low-strength primitive ice inside cometary boulders". In: *Nature* 586 (Oct. 2020), pp. 697–701. DOI: 10.1038/s41586-020-2834-3.

[36] Nilda Oklay et al. "Variegation of comet 67P/Churyumov-Gerasimenko in regions showing activity". In: *Astronomy and Astrophysics* 586 (Feb. 2016), A80.

[37] Maurizio Pajola, S. Höfner, et al. "The pristine interior of comet 67P revealed by the combined Aswan outburst and cliff collapse". In: *Nature Astronomy* 1 (Mar. 2017), p. 0092. DOI: 10.1038/s41550-017-0092.

[38] Maurizio Pajola, Jui-Chi Lee, et al. "Multidisciplinary analysis of the Hapi region located on Comet 67P/Churyumov–Gerasimenko". In: *Monthly Notices of the Royal Astronomical Society* 485 (May 2019). DOI: 10.1093/mnras/stz446.

[39] Maurizio Pajola, Nilda Oklay, et al. "Aswan site on comet 67P/Churyumov-Gerasimenko: Morphology, boulder evolution, and spectrophotometry". In: *Astronomy and Astrophysics* 592 (Aug. 2016), A69.

[40] Maurizio Pajola, J.B. Vincent, et al. "Size-frequency distribution of boulders >=7 m on comet 67P/Churyumov-Gerasimenko". In: *Astronomy Astrophysics* (Sept. 2015). DOI: 10.1051/0004-6361/201525975.

[41] Luca Penasa et al. "A three-dimensional modelling of the layered structure of comet 67P/Churyumov-Gerasimenko". In: (July 2017). DOI: 10.1093/mnras/stx2899.

[42] Olivier Poch et al. "Ammonium salts are a reservoir of nitrogen on a cometary nucleus and possibly on some asteroids". In: *Science* 367 (Mar. 2020), eaaw7462. DOI: 10.1126/science.aaw7462.

[43] Antoine Pommerol et al. "OSIRIS observations of meter-size exposures of H2O ice at the surface of 67P/Churyumov-Gerasimenko and interpretation using laboratory experiments". In: *Astronomy and Astrophysics* 583 (Nov. 2015), A25. DOI: 10.1051/0004-6361/201525977.

[44] Frank Preusker et al. "The global meter-level shape model of comet 67P/Churyumov-Gerasimenko". In: *Astronomy Astrophysics* 607 (Oct. 2017). DOI: 10.1051/0004-6361/201731798.

[45] Alessandra Rotundi et al. "Dust measurements in the coma of comet 67P/Churyumov-Gerasimenko inbound to the Sun". In: *Science* 347 (Jan. 2015), aaa3905. DOI: 10.1126/science.aaa3905.

[46] H Sierks et al. "Images of Asteroid 21 Lutetia: A Remnant Planetesimal from the Early Solar System". In: *Science (New York, N.Y.)* 334 (Oct. 2011), pp. 487–90. DOI: 10.1126/science.1207325.

[47] Holger Sierks et al. "On the nucleus structure and activity of comet 67P/Churyumov-Gerasimenko". In: *Science* 347 (Jan. 2015). DOI: 10.1126/science.aaa1044.

[48] Nicolas Thomas, B. Davidsson, et al. "Redistribution of particles across the nucleus of comet 67P/Churyumov-Gerasimenko". In: *Astronomy Astrophysics* 583 (June 2015). DOI: 10.1051/0004-6361/201526049.

[49] Nicolas Thomas, H. Sierks, et al. "The morphological diversity of comet 67P/Churyumov-Gerasimenko". In: *Science* 347 (Jan. 2015).

[50] Peter Thomas et al. "The shape, topography, and geology of Tempel 1 from Deep Impact observations". In: *Icarus* 187 (Mar. 2007), pp. 4–15. DOI: 10.1016/j.icarus.2006.12.029.

[51] Pious Thomas et al. "The nucleus of Comet 9P/Tempel 1: Shape and geology from two flybys". In: *Icarus* 222 (Feb. 2013), pp. 453–466. DOI: 10.1016/j.icarus.2012.02.037.

[52] C Tubiana et al. "67P/Churyumov-Gerasimenko: Activity between March and June 2014 as observed from Rosetta/OSIRIS". In: *Astronomy and Astrophysics* 573 (Jan. 2015). DOI: 10.1051/0004-6361/201424735.

[53] Cecilia Tubiana et al. "Comet 67P/Churyumov-Gerasimenko at a large heliocentric distance". In: *Astronomy and Astrophysics, v.490, 377-386 (2008)* 527 (Oct. 2008). DOI: 10.1051/0004-6361:20078792.

[54] Cécilia Tubiana et al. "Scientific assessment of the quality of OSIRIS images". In: *Astronomy and Astrophysics* 583 (Nov. 2015), A46.

[55] J. Vincent et al. "Are fractured cliffs the source of cometary dust jets? Insights from OSIRIS/Rosetta at 67P/Churyumov-Gerasimenko". In: *Astronomy Astrophysics* 587 (Mar. 2016).

[56] I Wright et al. "COMETARY SCIENCE. CHO-bearing organic compounds at the surface of 67P/Churyumov-Gerasimenko revealed by Ptolemy". In: *Science (New York, N.Y.)* 349 (July 2015). DOI: 10.1126/science.aab0673.